UNIVERSITY OF CAPE TOWN

DEPARTMENT OF MECHANICAL ENGINEERING

RONDEBOSCH, CAPE TOWN, SOUTH AFRICA

Fabrication of PtNi and PtV Near-Surface Alloys as Improved Catalysts for Proton Exchange Membrane Hydrogen Fuel Cells

Clinton Leary

A dissertation submitted to the Faculty of Engineering and the Built Environment in fulfillment of the requirements for the degree of Master of Science in Engineering

January 2014

ABSTRACT

This study concerns the characterization of platinum nickel (PtNi) and platinum vanadium (PtV) near-surface alloys (NSAs) for use as improved catalysts in proton exchange membrane hydrogen fuel cells. The need for this study arose in order to further understand the principles behind the predicted catalytic properties of NSAs, to fabricate them and to characterize them experimentally.

Two groups of NSAs were fabricated, namely PtNi and PtV. Pt was used as the parent metal while Ni and V were used as the solute/near surface constituents. Within these groups of Pt with Ni or V, variations in coating thickness and heat treatments were used to attempt to fabricate the NSA structure.

Surface profile analysis was carried out using profilometry and light microscopy. These techniques showed that surfaces were not always of a 100% mirror finish and that deposited coatings were not stable and were prone to peeling especially with coatings of greater than one layer. Elemental analysis was performed by employing energy-dispersive x-ray spectroscopy (SEM-EDS), proton induced x-ray emission (PIXE) and Rutherford backscattering spectrometry (RBS). These techniques helped verify the presence of the thin deposited coatings whilst also highlighting the presence of contaminants in the form of iron, manganese and chromium.

Tafel Plot analysis was used to gather electrochemical data for the NSAs. In this regard, the hydrogen reduction (evolution) reaction was analyzed with the exchange current density extracted experimentally therefrom. This technique confirmed that Pt is indeed a superior catalyst, especially compared to pure Ni and V. It showed that e-beam deposition did not create coated systems which were suitable for Tafel analysis. It also illustrated that deaeration via nitrogen gas was not always effective with trace oxygen sometimes being present in the purge gas, resulting in contaminant oxygen reduction distorting the electrochemical results.

Ultimately, electron-beam deposition proved to be inefficient in fabricating stable coatings for catalysis, with the coatings possibly not being adequately thin to mimic the NSA structure. This, coupled with trace oxygen reduction, prevented effective analysis of NSA catalytic properties.

ACKNOWLEDGEMENTS

I would like to thank everyone who assisted and supported me throughout the duration of this project, in particular:

- God, without whom I would not have had the strength to make it this far in my life.
- My supervisor, Professor C.I Lang, for her supervision and constant guidance throughout my project.
- Professor R. Knutsen, for all his advice and guidance.
- Professor J. Petersen for his valuable input.
- Doctor Nkosi, Doctor Topic and Doctor Pineda at iThemba Labs.
- Professor D.J Simbi for his support.
- Beverly Glass for always providing a friendly welcome.
- Doctor Sarah George and Liezl Matthews for all their assistance in the lab.
- Penny Park Ross for ensuring that laboratory chemicals and equipment were always available.
- Gerard Leteba for all his help in the labs.
- All the students and staff at the Centre for Materials Engineering for their support, assistance and friendship.
- Leandrie for all her motivation and support.

I would also like to say a very special thank you to my dad who has supported me throughout my life and studies and without whom my goals would not have been realised.

DECLARATION

I, Clinton Derek Leary, know the meaning of plagiarism and declare that all the work in this document, save for that which is properly acknowledged, is my own.

Signed by candidate

Signature: Signature Removed

Date: 30/08/2015

TABLE OF CONTENTS

LIST OF FIGURES

LIST OF TABLES

CHAPTER 1

INTRODUCTION

1.1 Subject of Study

This report concerns the characterisation of platinum nickel (Pt/Ni) and platinum vanadium (Pt/V) near-surface alloys (NSAs) with regard to their surface and electrochemical properties and their possible use as improved catalysts (electrodes) in the proton exchange membrane hydrogen fuel cell (PEMFC). This experimental work arises from reported computational modelling which predicts that NSAs display superior catalytic activity, relative to pure platinum catalysts, in PEMFCs. In this work, focus is placed on the hydrogen reduction (evolution) reaction to determine catalytic efficacy.

1.2 Background to Study

With crude oil reserves being depleted there is dire need for alternative, clean and renewable energy sources. This is especially true for the automotive industry. One potential energy source is the PEMFC, whereby electricity is generated by the splitting of hydrogen (H_2) (oxidation) and oxygen (O_2) (reduction) molecules causing electrons to flow through a closed, external circuit. PEMFCs can be used to power electric motors which in turn can be used to power passenger vehicles. Besides the advantage of both hydrogen and oxygen being abundantly available elements, the by-product of this process is minimal heat and clean water.

Currently pure platinum is used as both the anode and cathode in the PEMFC due to its superior catalytic properties relative to other pure metals. Platinum is however a costly metal making the use of hydrogen fuel cells expensive. Platinum is also not a highly abundant element which stands as a limiting factor for industrial scale applications of PEMFCs. NSAs are formed by creating a subsurface nano-layer of solute metal within a host metal, platinum to form an alternative catalyst material. It must be noted that although the hydrogen reduction reaction was studied in the present research, the principle that NSAs are predicted to display enhanced catalytic activity in both hydrogen and oxygen related reactions still stands, regardless of which species is being reduced/oxidized (i.e. fast hydrogen reduction kinetics implies fast oxygen reduction kinetics).

Use of Pt based NSAs is highly desirable as NSA geometries are on the nanometer scale. Thus, minimal material is used in the NSA catalyst, especially pertaining to the platinum content. Furthermore, NSAs incorporate the use of a solute metal thus further minimizing the total pure platinum content. As NSAs are predicted to have superior catalytic properties compared to pure platinum, it stands to reason that a more effective catalyst would also generate more electricity regarding the fuel cell application.

One now has a catalyst that not only requires less platinum, thus reducing cost, but also a potentially superior catalyst generating more electricity. The result is a cheaper fuel cell yielding greater electric outputs. Combining this reduced Pt loading with improvement on the efficacy and selectivity of the Pt catalyst, NSAs provide a promising alternative to PEMFC electrodes.

1.3 Objectives of Study

The objectives of this investigation are therefore to:

- Fabricate Pt/V and Pt/Ni NSAs using electron beam deposition (e–beam) and heat treatments.
- Characterise these NSAs with regard to their surface and electrochemical properties.
- Determine, experimentally, whether e-beam deposition is an effective fabrication technique for NSAs; and whether these display superior catalytic behaviour relative to pure Pt.

1.4 Limitations and Scope of Study

Research into NSAs is a relatively new field in the context of catalysis and so there was limited literature available on the subject.

Many of the analytical techniques available such as Energy Dispersive X-ray Spectroscopy (EDS) and X–Ray Diffraction (XRD) were restricted due to the nano–scale geometry of the NSAs, with the surface layers of the NSAs being too thin for analysis. EDS was only accurate down to a contaminant concentration of 1%, there is, accordingly, the possibility of undetected contaminants.

Rutherford Backscattering Spectrometry (RBS) was also restricted by the thin, nano-scale thickness of the coatings, where only the 5nm Pt coating on Ni substrates was seen.

Pure Pt was used as a substrate for the NSA samples fabricated, and thus due to the high cost of Pt, there was a limited amount of Pt available. Each sample was only tested once with regard to the electrochemical analysis. After analysis, coatings were polished off the Pt surfaces and re-used; while after approximately 3 rounds of testing Pt substrates were sent for complete recycling at *Perkins metals*.

Due to limited time available and time constraints, PIXE was only available for the PtNi and PtV NSA samples.

1.5 Plan of Development

This project begins with a review of the literature available on platinum metal, fuel cells, electrochemistry and NSAs. This is followed by an outlining of the experimental procedure whereafter results will be presented and discussed. Conclusions will then be drawn from the discussion followed by recommendations for future work.

CHAPTER 2

LITERATURE REVIEW

2.1 Platinum

There are many claims of who first discovered platinum (Pt) but it is most commonly cited to have been discovered by a Spaniard, Don Antonio de Ulloa, in 1735. It was given the name platinum from the Spanish word *platina* which means 'little silver'.

Platinum is a soft, malleable metal which is often alloyed with small amounts of iridium to lend it increased strength and hardness whilst still maintaining all the desirable properties of pure Pt. Pt is part of the Pt group metals (PGMs) which contains, along with Pt, osmium (Os), iridium (Ir), ruthenium (Ru), palladium (Pd), and rhodium (Rh). The PGMs share remarkably similar chemical and physical properties and typically occur together in ore deposits[1].

Pt is a noble metal in that it is resistant to corrosion and oxidation even up to its melting temperature of 1772.0 °C. Pt does not dissolve in most solvents (acidic or alkaline) however it will dissolve in aqua regia (a mixture of concentrated nitric acid and hydrochloric acid). It is due to this noble trait that Pt occurs in its almost pure/native form in nature. It is naturally and most commonly found as polyxene, which consists primarily of pure Pt along with iron, gold, copper, nickel and a small amount of the other PGMs. Pt can also be obtained from the very rare native alloy, platiniridium. One can also find Pt in less common mineral deposits such as sperrylite, cooperlite, chromite and olivine. The majority of the world's Pt production is mined in South Africa[1].

Pt is predominantly used in the automotive, dental, jewellery and chemical industries. The primary interest in Pt with regards to this research project is as a catalyst, more specifically, as a catalyst used in the Proton Exchange Membrane Hydrogen Fuel Cell (PEMFC). Pt's stable chemical and electrical properties make it an outstanding catalyst. However, Pt is globally one of the most expensive metals (owing to its rarity in the earth's crust) and as it is used as both the anode and cathode in PEMFCs, it drives up the cost of such fuel cells.

To improve on the efficacy and selectivity of the Pt catalyst would be desirable as it would potentially allow for the reduction of Pt loading in the fuel cell, thereby reducing the cost involved[2].

One approach to increasing Pt's efficacy and selectivity as a catalyst, and reducing the cost involved, is through the use of Pt based Near–Surface Alloys (NSAs)[2]. Near-surface alloys will be discussed in section 2.4 of the literature review.

2.2 Fuel Cells

2.2.1 Background

With fossil fuels slowly being depleted, an energy crisis looms. There is a dire need for an alternative and renewable energy source. One such option is fuel cells. The basic principle of the fuel cell was first discovered by German scientist Christian Friedrich Schönbein in the 19th century. Using the theory discovered by Schönbein, a Welsh man by the name of Sir William Robert Grove, practically demonstrated the first functioning fuel cell in the mid-19th century[3,4].

Fuel cells are electrochemical cells (galvanic cells[1]) in which the free energy of a chemical reaction is converted into an electric current (electricity)[3,5–7]. The change in Gibbs free energy of this chemical reaction is related to the cell voltage as seen in the following equation[3,6,7].

$$\Delta G = -nF\Delta U_0$$

Where ΔG is the Gibbs free energy, n is the number of electrons involved in the reaction, F is the Faraday constant and ΔU_0 is the voltage of the cell for the thermodynamic equilibrium in the absence of a current [3,6,7]. Since n, F, and U_0 are all positive numbers, the overall reaction is negative thus indicating a spontaneous reaction, this being the thermodynamic principle behind the fuel cell.

The typical reaction that occurs in a hydrogen/oxygen fuel cell can be seen in the following equation where ΔG is the change in Gibbs free energy of formation[8].

$$H_2 + \tfrac{1}{2} O_2 \rightarrow H_2O \quad \text{with } \Delta G = -237\text{kJ/mol}$$

[1] Galvanic cells produce electrical energy from chemical energy (chemical reactions) whereas electrolytic cells use electrical energy to drive a chemical reaction.

The theoretical equilibrium voltage/EMF[2] for an ideal (single) hydrogen/oxygen fuel cell is 1.23V at STP (standard temperature and pressure) of 101.325 kPa (1 atmosphere) at 25°C [8]. This is demonstrated by the following equation[3,6,7,9].

$$\Delta U_0 = -\Delta G/nF = 1.23V$$

However, the actual operating voltage of such a fuel cell is about 0.6 – 0.7V at STP[8]. In figure 2.1 we see a graph illustrating the four main causes for these voltage losses as proposed by Zhang[10].

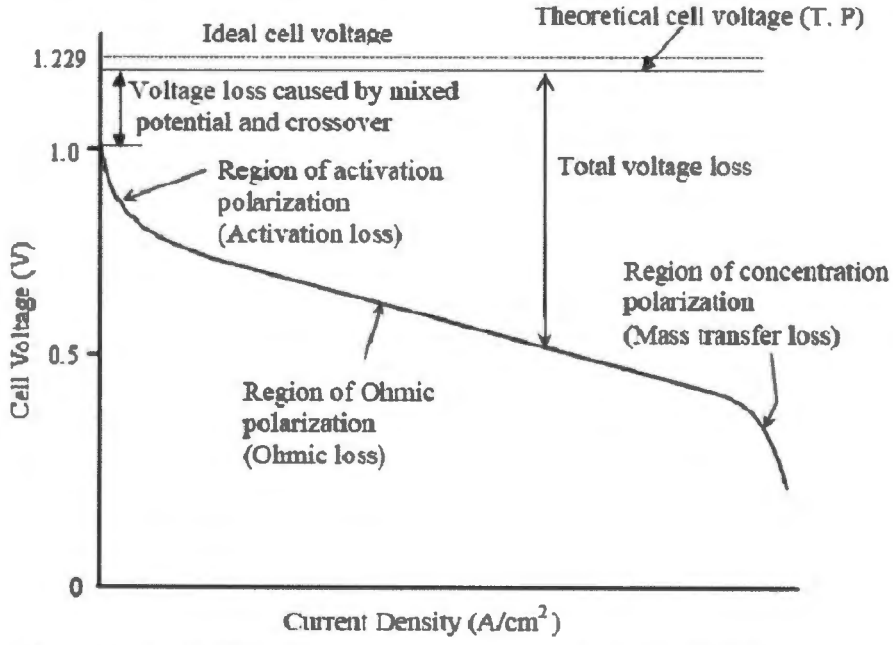

Figure 2. 1: Graph of voltage vs. current density illustrating voltage loss between theoretical and actual PEMFC output[10].

[2] EMF or electromotive force is defined as, "The cell voltage of a galvanic cell measured when there is no current flowing through the cell."

Mixed potential and fuel crossover voltage drops occur as a result of "unavoidable parasitic" reactions which decrease the equilibrium electrode potential[3]. A dominant cause of this phenomenon is due to fuel crossover where the hydrogen fuel passes through the PEM from the anode to cathode or from the cathode back to the anode. In both scenarios no current is produced and we see a voltage drop[9,11].

Activation polarization (overpotential) drop[4] occurs where the cell voltage drops rapidly at low current densities due to slow reaction kinetics at the electrodes/catalyst[9,12–16]. This is particularly true with the oxygen reduction reaction (ORR) in PEMFC's where the ORR is the rate limiting electrode with regards to its slow reaction kinetics[9,13–16].

Ohmic polarization (loss) arises due to the ohmic resistance caused by the proton exchange membrane itself (resistance to the flow of protons through the membrane), resistance of the flow of electrons through the electrodes and conducting resistance between the electrodes and proton exchange membrane[9,13,14].

Concentration polarization (mass transportation losses) arises as a result of mass transport limitations of the reactant gases/fuel (hydrogen and oxygen) to the electrodes. As the reaction proceeds and the fuel is consumed, a concentration gradient develops where the concentrations of the reactant gases are lower at the electrodes compared to at the gas inlet channels. Thus, at high current densities, sluggish transportation of the reactants and products to and from the electrodes results in the concentration voltage drop[9,13,14,16].

[3] See emf above. Also known as open circuit potential (OCP).
[4] Overpotential can be defined as, "The difference in the electrode potential of an electrode between its equilibrium potential and its operating potential when a current is flowing. The overpotential represents the extra energy needed (an energy loss that appears as heat) to force the electrode reaction to proceed at a required rate (or its equivalent current density)." Or one could say that polarization is the change of an electrode's potential from its equilibrium potential and the magnitude of this change is the overpotential.

One can increase the voltage output of a fuel cell by connecting multiple single fuel cells together in series to form a stack. Bipolar plates are electrically conductive plates used to separate and connect individual fuel cells together to form a fuel cell stack[10]. The total voltage output will be the sum of each individual fuel cell whilst the current will be equal in every cell[17]. In figure 2.2 we see a simple schematic of a fuel cell stack[18].

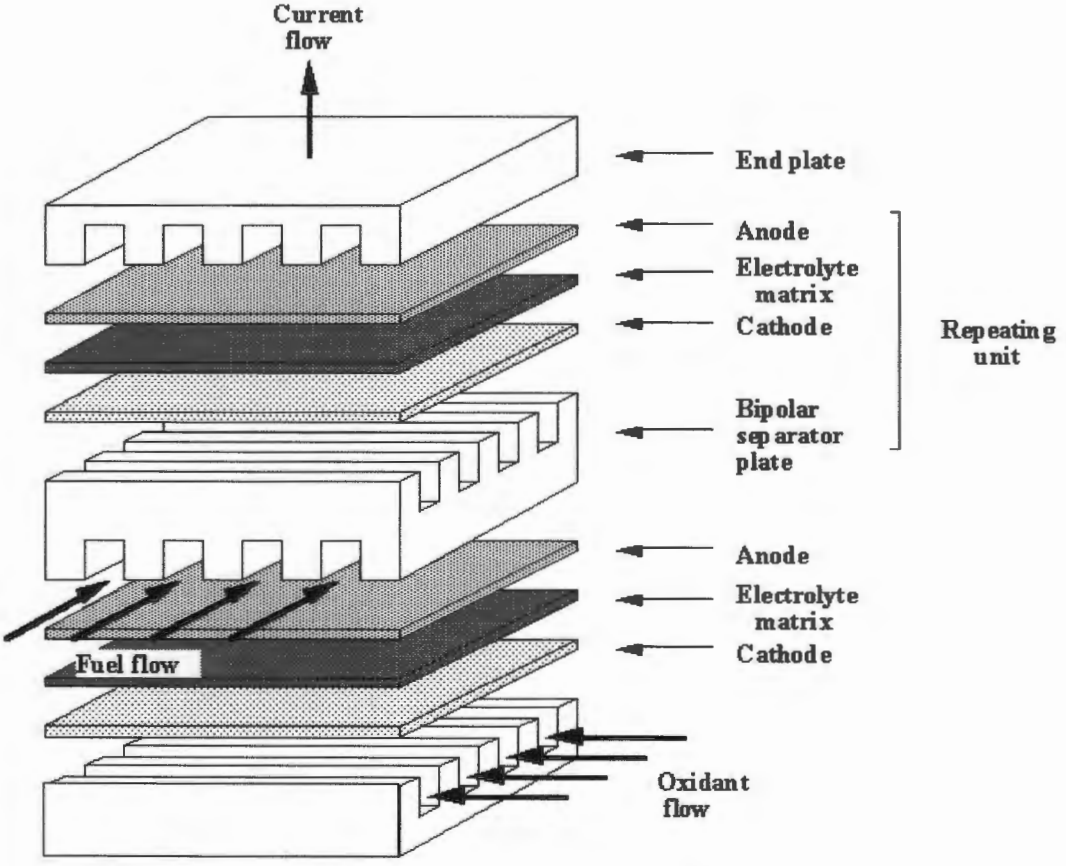

Figure 2. 2: Schematic of the components of a fuel cell stack[18].

The various types of fuel cells, along with their operating parameters and basic characteristics, are displayed in table 2.1[3,19–24].

Table 2. 1: Overview of different fuel cells[3,19-24].

	AFC (Alkaline)	PEMFC (Polymer Electrolyte Membrane)	DMFC (Direct Methanol)	PAFC (Phosphoric Acid)	MCFC (Molten Carbonate)	SOFC (Solid Oxide)
Operating temp. (°C)	<100	60–120	60–120	160–220	600–800	800–1000 low temperature (500–600) possible
Anode reaction	$H_2 + 2OH^- \rightarrow 2H_2O + 2e^-$	$H_2 \rightarrow 2H^+ + 2e^-$	$CH_3OH + H_2O \rightarrow CO_2 + 6H^+ + 6e^-$	$H_2 \rightarrow 2H^+ + 2e^-$	$H_2 + CO_3^{2-} \rightarrow H_2O + CO_2 + 2e^-$	$H_2 + O^{2-} \rightarrow H_2O + 2e^-$
Cathode reaction	$\frac{1}{2}O_2 + H_2O + 2e^- \rightarrow 2OH^-$	$\frac{1}{2}O_2 + 2H^+ + 2e^- \rightarrow H_2O$	$3/2\,O_2 + 6H^+ + 6e^- \rightarrow 3H_2O$	$\frac{1}{2}O_2 + 2H^+ + 2e^- \rightarrow H_2O$	$\frac{1}{2}O_2 + CO_2 + 2e^- \rightarrow CO_3^{2-}$	$\frac{1}{2}O_2 + 2e^- \rightarrow O^{2-}$
Applications	Transportation Space Military Energy storage systems			Combined heat and power for decentralised stationary power systems	Combined heat and power for stationary decentralised systems and for transportation (trains, boats, ...)	
Realised Power	Small plants 5–150kW modular	Small plants 5–250 kW modular	Small plants 5 kW	Small – medium sized plants 50kW – 11MW	Small power plants 100-kW- 2 MW	Small power plants 100-250kW
Charge Carrier in the Electrolyte	OH^-	H^+	H^+	H^+	CO_3^{2-}	O^{2-}

Table 2. 2: A List of anode and cathode materials used in different fuel cells[6,24,25].

Fuel cell	Anode catalyst	Cathode catalyst
AFC	Pt/Au, Pt, Ag, Ni, Ni/Ti, Pt/Pd	Pt/Au, Pt, Ag, Pt on carbon, Ag or different perovskites or spinels
PEMFC	Pt, Pt/Ru	Pt, Pt/C, Pt alloys
PAFC	Pt	Pt/Cr/Co, Pt/Ni
MCFC	Ni, Ni/Cr	Li/NiO
SOFC	Ni/ZrO_2(Y)-cermet layers	perovskites, e.g. $LaMnO_3$, $LaSrMnO_3$
DMFC	Pt/Ru, Pt/Sn, Pt/WO_3	Pt, metal chelates, thiospinels

2.2.2 The PEM Hydrogen Fuel Cell (PEMFC)

The PEM hydrogen fuel cell offers an outstanding possibility in the quest for cleaner, alternative energy sources[26]. This is particularly valid for mobile/transport applications such as for light passenger vehicles. The PEMFC produces an electrical current by oxidation of hydrogen and reduction of oxygen. The primary component of a PEMFC is the MEA (membrane electrode assembly) which is comprised of the proton exchange membrane which is composed of poly-perfluorosulfonic acid, known as Nafion by DuPont, which is in contact with both the anode and cathode on either side[10]. The PEMFC differs from other types of fuel cells in that it operates at relatively low temperatures (as seen in table 2.1), it has a solid electrolyte/PEM (as opposed to liquid), it exhibits fast startup, has high power densities and is portable[8,27–29]. These features make the PEMFC perfect for mobile applications. In figure 2.3 a schematic of the PEMFC is shown[27].

There are, however, still limitations to current PEMFC technology which are impeding them from being used commercially. This is especially true for applications as a mainstream alternative to internal combustion engines in passenger vehicles. Some of the main limitations of PEMFCs, using pure Pt electrodes ,are discussed below[30,31]. These limitations directly pertain to near-surface alloys, because NSAs are a prospective solution to them.

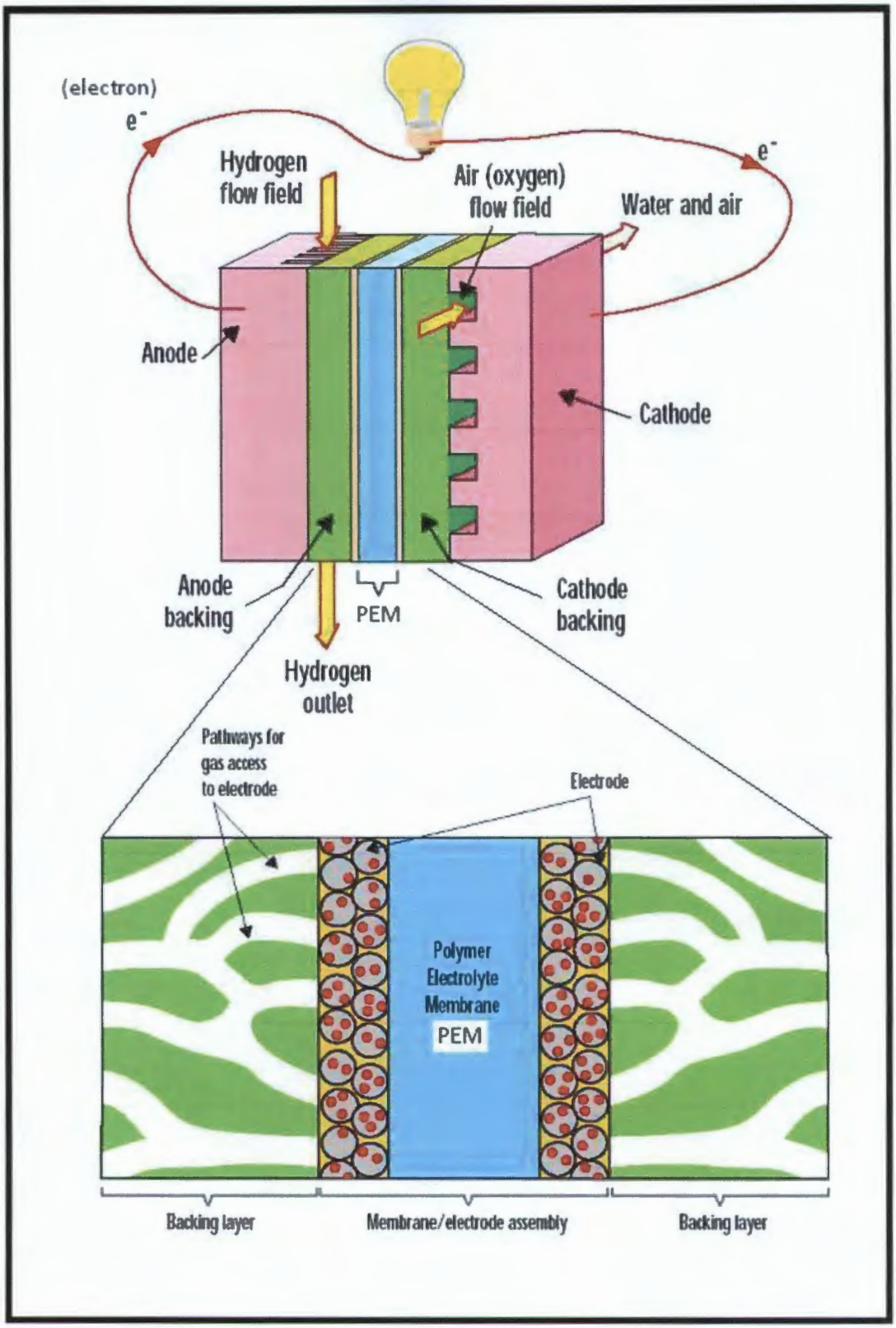

Figure 2. 3: Illustration of a PEM hydrogen fuel cell[27].

2.2.2.1 General Features of PEMFCs

(a) PEMFC Limitations[5]

(1) Carbon monoxide (CO) poisoning of the anode[30,31].

(2) Hydroxide (OH) poisoning of the cathode[30,31].

(3) Slow oxygen reduction kinetics[30,31].

(4) The high cost of Pt metal which is used for both the cathodic and anodic electrode material[30,31].

[5] These limitations will be discussed in greater detail in section 2.4 on near-surface alloys.

(b) Anodic (Oxidation) Reaction of Hydrogen in the PEMFC

Hydrogen oxidation takes place readily on Pt catalysts, with the kinetics of this reaction being very fast. Hydrogen oxidation kinetics at larger current densities are typically controlled by mass-transfer limitations[3,6,25].

Hydrogen gas (H_2) adsorbs to the Pt anode surface. The H_2 gas is then catalyzed (split) into H^+ ions resulting in the release of the H_2 bonding electrons. These electrons are unable to pass through the proton exchange membrane (PEM) and thus need to flow through an external circuit in order to reach the Pt cathode. The H^+ ions are able to move across the PEM; in so doing they come into contact with oxygen atoms being reduced on the cathode. This flow of electrons gives rise to a current and thus electricity is generated. On reaching the cathode, the electrons provide for the bonding between the H^+ ions and reduced oxygen atoms to form water (H_2O). The oxidation of hydrogen is illustrated in the equations below[3,6,25]:

$$2\,Pt_{(s)} + H_2 \longrightarrow 2\,Pt\text{-}H_{ads}$$

$$Pt\text{-}H_{ads} \longrightarrow H^+ + e^- + Pt_{(s)}$$

$Pt_{(S)}$ is a free active site on the Pt surface whilst $Pt\text{-}H_{ads}$ is a hydrogen atom adsorbed to a free active site on the Pt. The overall oxidation reaction of hydrogen can be aeen in the following equation[3,6,25]:

$$H_2 \longrightarrow 2\,H^+ + 2e^- \qquad U_0 = 0V$$

(c) Cathodic (Reduction) Reaction of Oxygen in the PEMFC

The oxygen reduction reaction (ORR) is a somewhat more complex reaction than the oxidation of hydrogen. The ORR is the kinetically slower reaction of the two processes. The slow ORR kinetics is attributed to several factors: oxygen is usually sourced from air feeds and is not pure oxygen (thus lower oxygen partial pressures), possible hydroxide (OH^-) poisoning of the cathode, breaking of the strong oxygen-oxygen double bond and the dual pathway of the ORR as described below[3,6,19,25,32–37].

The ORR commences along two parallel pathways, an indirect 2-electron pathway (hydrogen peroxide formation) and a direct 4-electron pathway (water formation). These two pathways are illustrated by the following two equations[3,6,19,25,32–37]:

(1) $O_2 \rightarrow O_{2,ads} \xrightarrow{4H^+ + 4e^-} 2\,H_2O_{ads} \rightarrow 2\,H_2O_{sol}$

(2) $O_2 \rightarrow O_{2,ads} \xrightarrow{2H^+ + 2e^-} (H_2O_2)_{ads} \xrightarrow{2H^+ + 2e^-} (H_2O)_{ads}$

$(H_2O_2)_{sol}$ $(H_2O)_{sol}$

In equation (1) we see the direct 4-electron pathway in which water (H_20) is the final product. This is the more desirable of the two pathways as there is no peroxide formed and it has a greater Faradaic efficiency[6]. Equation (1) occurs when the oxygen (O_2) molecule adsorbs to the catalyst so that its axis is parallel to the catalyst surface. It is then cleaved into two oxygen atoms which are reduced and protonated from protons coming via the PEM to form water[3,6,19,25,32–37].

In equation (2) the indirect 2-electron pathway is shown in which either H_20 or hydrogen peroxide (H_20_2) is formed. This occurs when the O_2 molecule adsorbs to the catalyst so that its axis is perpendicular to the catalyst surface. In this scenario the O_2 molecule does not cleave but is rather partially reduced and protonated to form the peroxide anion (HO_2^-) adsorbed intermediate. This intermediate can either be protonated by the incoming protons from the PEM to form H_20_2 or it can be further reduced and protonated to form H_20. Due to the complex nature of this pathway, the ORR requires a substantial overpotential with the activation overpotential being approximately 300-400mV at current densties appropriate for fuel cell applications, whereas for the hydrogen oxidation reaction the overpotential is approximately 50mV[3,6,19,25,32–37]. In figure 2.4 we see a graphic representation of these dual ORR pathways[6].

[6] Faradaic efficiency refers to the efficacy with which electrons are transported in a system, thus enabling an electrochemical reaction.

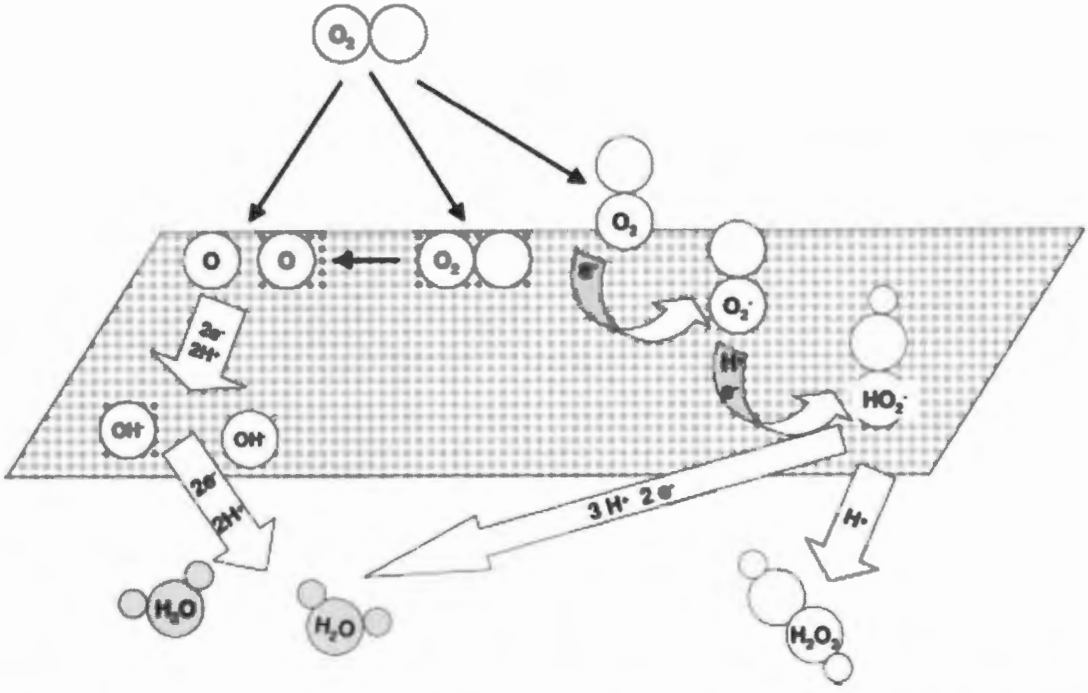

Figure 2. 4: Illustration of the two ORR pathways with the left hand side being the direct 4-electron pathway and the right hand side being the indirect 2-electron pathway[6].

2.3 Electrochemistry

2.3.1 Heterogeneous Catalysis

Heterogeneous catalysis is a type of catalysis where the phase state of the reactants is different to the phase state of the catalyst. This is the case for the PEMFC where the Pt catalyst is solid and the reactants (oxygen and hydrogen) are gases, and entails the adsorbing of reactants to the catalyst surface, breaking and formation of bonds forming reaction intermediates and finally desorption of products from catalyst surface. Pt has always been the first choice as both the anode and cathode catalyst in PEMFCs due to its superior catalytic activity, due to Pt's nobleness which makes it a superior catalyst. The perfect catalyst would ideally follow the Sabatier principle which states that "the most active catalyst for a given reaction should not bind too strongly or too weakly to the reaction intermediates"[38,39].

In other words the catalyst needs to form a strong enough bond with reactants to allow for a reaction to take place whilst at the same time not bond too strongly to products so as not to allow them to be released[40].

The main characteristic which determines a metal's catalytic nature is its surface and subsurface electronic structure. It is this electronic structure which governs how well the metal catalyst is able to create and break bonds with reacting molecules and thus allows us to identify and explain the trends in reactivity of different metal catalysts[40].

The catalytic performance of various metals is typically evaluated via reactions involving common adsorbates such as H_2, O_2, CO and OH with reference to the Sabatier principle[40].

Hammer and Norskov produced a theoretical framework, grounded on d-band hybridisation theory, which allowed for the explanation of the reactions occurring on the surface of catalysts and reacting adsorbates with regards to bond formation and breaking as explained in section 2.3.2[2,39–45].

2.3.2 The d-Band Model

There have been many attempts at elucidating the electronic factors which give rise to the specific catalytic properties and reactivity of different metallic surfaces[40].

One such attempt looked at the reactivity of a surface as being linked to the number of holes in the d-band[40,46], whilst another related reactivity to the local density of one-electron states at the Fermi level($LDOS_{E_F}$)[40,47].

Hammer and Norkov, however, used density functional theory calculations to gain a better understanding of what physical properties of a metal's surface determined its chemical reactivity. They considered the H_2 dissociation reaction as the basis for their tests. They chose four metal surfaces illustrating four types of systems, namely: a system with a d-band and a small $LDOS_{E_F}$(Cu (111)), a system with a d-band and a large $LDOS_{E_F}$(Pt (111)), a system with no holes in the d-band (Cu_3Pt (111)) and a system without a d-band (Al (111))[40,41].

From these experiments they concluded that looking at just the number of holes in the d-band or at the $LDOS_{E_F}$, was insufficient for determining what gave rise to the reactivity of metal surfaces and consequently offered the d-band model[40,41].

According to the d-band model, deviations between different metals' reaction barriers and adsorption energies are due to differences in the coupling of the adsorbate sp-states to the metal d-state. There are two contributing factors which influence the energy of the adsorbate-metal bond with regards to the d-band model:

(i) The formation of a stable adsorbed state via the linking of the adsorbate state to the free electron like s-orbitals. Linking of the adsorbate state to the free electron s-orbitals is independent of the metal with the s-orbitals of transition metals being "broad, featureless and always half filled"[40,48].

(ii) The interaction of adsorbates with the metal d-states is what gives rise to the variation in reactivity of the transition metals in the periodic table. This interaction of adsorbates with metal d-states results in the adsorbate states splitting into bonding and anti-bonding states. How electrons are distributed across the bonding and anti-bonding states dictates the bond strength between adsorbate and metal surface. If the anti-bonding states are above the Fermi level then they will not be occupied and thus the bond between adsorbate and metal surface is strong. On the other hand if the anti-bonding states are below the Fermi level they are then occupied, with the population of the anti-bonding states leading to Pauli repulsion and the bond between adsorbate and metal surface is weak[40,49–51]. It can be said that for the reactivity of a metal surface, a high d-band moves the anti-bonding states above the Fermi level resulting in a stronger adsorbate bond, whereas, a low d-band populates the anti-bonding states, resulting in a weaker bond[40].

Based on the above information, various models have been developed which relate reactivity to the d-band centre (which is a measure of the average energy) or the d-band width[40,49–51].

2.3.3 The Tafel Equation

The Tafel Equation was deduced by German chemist, Julius Tafel. It is an electrochemical equation which relates the kinetics or rate of an electrochemical reaction to the overpotential of the reaction[52,53]. Below we see the Tafel equation for a single reaction in the forward and reverse directions[54]:

$$\ln i = \ln i_0 - \alpha nF\eta/RT$$

Where i is the current density (A/cm^2), i_0 is the exchange current density (A/cm^2), α is the charge transfer coefficient, n is the number of electrons involved in the electrode reaction, F is the Faraday constant, η is the overpotential (the difference between the applied potential and equilibrium potential), R the universal gas constant and T is the absolute temperature. This equation can be further expanded to solve for η[52,54]:

$$\eta = (2.3RT/\alpha nF) \log (i_0/i)$$

The key variable from the Tafel equation, which directly pertains to this research, is the exchange current density (i_0). Exchange current density is a commonly used parameter in the evaluation of catalysts[55]. It is a valuable kinetic parameter which illustrates the electrochemical reaction rate[56].

Exchange current density essentially reflects the intrinsic rate at which electrons are transferred between the electrode and reactants and thus how rapidly an electrochemical reaction will take place[56,57].

In table 2.3 below we see a comparison of exchange current densities for various metals with regard to the hydrogen reduction reaction[57–60].

Table 2. 3: Exchange current densities (log) of various metals for the hydrogen reduction reaction in 1M H_2S0_4 (sulphuric acid)[57-60].

Electrode Material	Exchange current density $log_{10}(A/cm^2)$
Palladium	-3.0
Platinum	-3.1
Rhodium	-3.6
Iridium	-3.7
Nickel	-5.2
Gold	-5.4
Tungsten	-5.9
Vanadium	-6.3
Niobium	-6.8
Titanium	-8.2
Cadmium	-10.8
Manganese	-10.9
Lead	-12.0
Mercury	-12.3

As can be seen in table 2.3, the exchange current density (i_0) for Pt compared to Hg varies by a factor of 10^{10} further illustrating platinum's outstanding catalytic performance. A higher current density indicates a superior catalytic material.

A basic example of a Tafel plot [log values of current density (*Amps/cm²*) vs. potential (E)(vs. SHE – standard hydrogen electrode)] is shown with a 'best fit line' in figure 2.5[52]. Here one sees the anodic and cathodic current slopes along with the open circuit potential (OCP). OCP is also referred to as the rest potential or corrosion potential (E_{corr}). It is the potential at which the net current flow is zero.

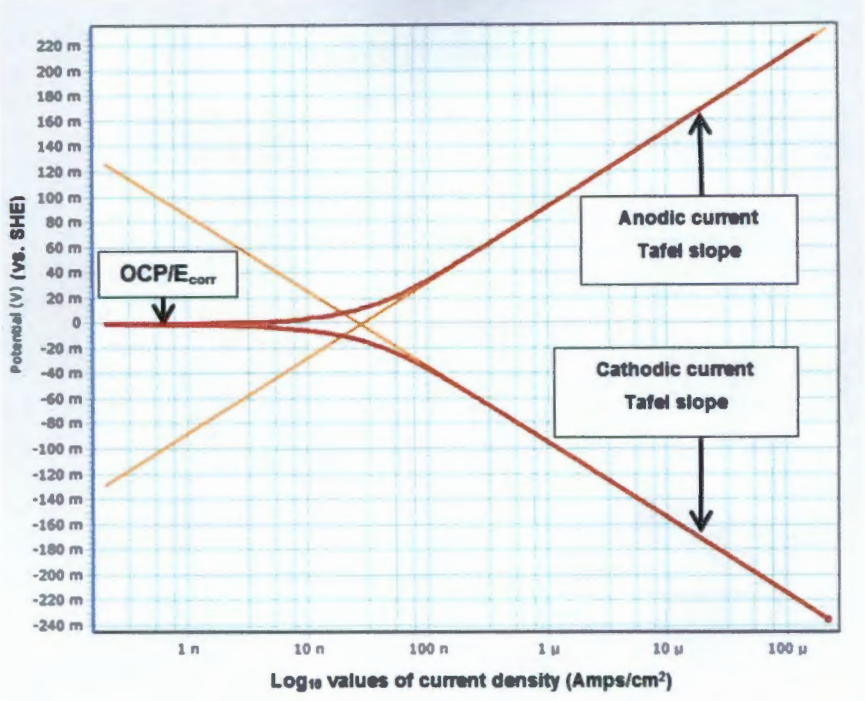

Figure 2. 5: Basic illustration of a Tafel plot showing OCP, anodic and cathodic currents[52].

2.4 Near-Surface Alloys (NSAs)

By definition, a Near-Surface Alloy (NSA) is a type of binary alloy comprising a host metal (bulk concentration) and a solute metal (low concentration) where the solute metal exists just below the surface of the host metal. This creates a subsurface alloy with the solute metal forming a distinct and separate layer from the host. A basic illustration of a NSA is shown in fig. 2.6[61].

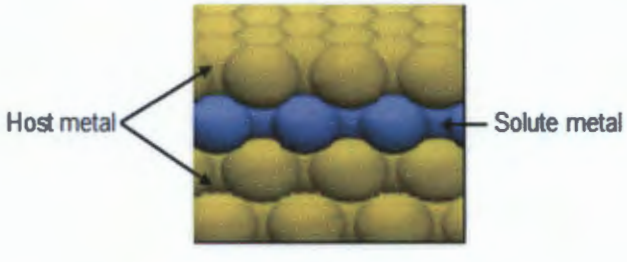

Figure 2. 6: Illustration of a NSA[61].

It is well understood that the chemical properties of bimetallic surfaces are often very different from those of either of the parent metals.

An example of this is the nickel/Pt (Ni/Pt) (111) surface with Ni coverage in the monolayer, which shows higher hydrogenolysis activity compared to that on either pure Ni or Pt[62].

NSAs are predicted to display superior catalytic activity relative to either of the pure parent metals making up the NSA. An example of this can be seen in hydrogen-related reactions with the dissociation of hydrogen (H_2). Typically, weak binding of atomic hydrogen (H) to the catalyst surface infers a high activation energy barrier for dissociation of H_2, as is the case with pure metal catalysts. In other words, weak binding of atomic hydrogen to a catalyst surface goes hand in hand with a lot of energy being required to split or dissociate molecular hydrogen into H^+ ions[61,63].

NSAs display an exciting exception to this rule: not only do they allow for weak hydrogen binding but they simultaneously allow for low H_2 activation energy barriers. This means that NSAs would provide a catalyst that weakly adsorbs hydrogen to the reactive surface with less energy required to dissociate the H_2. With weakly adsorbed hydrogen comes easier release of the H^+ formed. The weaker hydrogen binding makes subsequent reactions with H^+ easier and so lower temperatures can be used with NSA catalysts. Owing to this reduction in NSA reaction temperature, catalyst selectivity can increase as there would be insufficient thermal energy available to activate reaction pathways that would produce un-desired by-products[61,63].

2.4.1 Fabrication Techniques and Thin Film Formation

Various methods are available for depositing thin metal films onto target substrates. Examples include chemical techniques such as atomic layer deposition and physical techniques such as sputtering and pulsed laser deposition. The method used in this research was electron beam (e-beam) deposition, which falls into the category of physical vapor deposition.

A tungsten (W) filament is heated under vacuum to the point that it begins to emit electrons. These electrons are then directed towards the metal to be evaporated (the evaporant) by magnets. The electrons cause the evaporant to heat up and vaporize due to kinetic energy from the impacting electrons being converted into thermal energy. The vapor rises and condenses on the surface of the target metal resulting in fabrication of a thin film (and ultimately, with deposition of two layers, the NSA)[64]. Figure 2.7 shows a schematic of e-beam deposition[65].

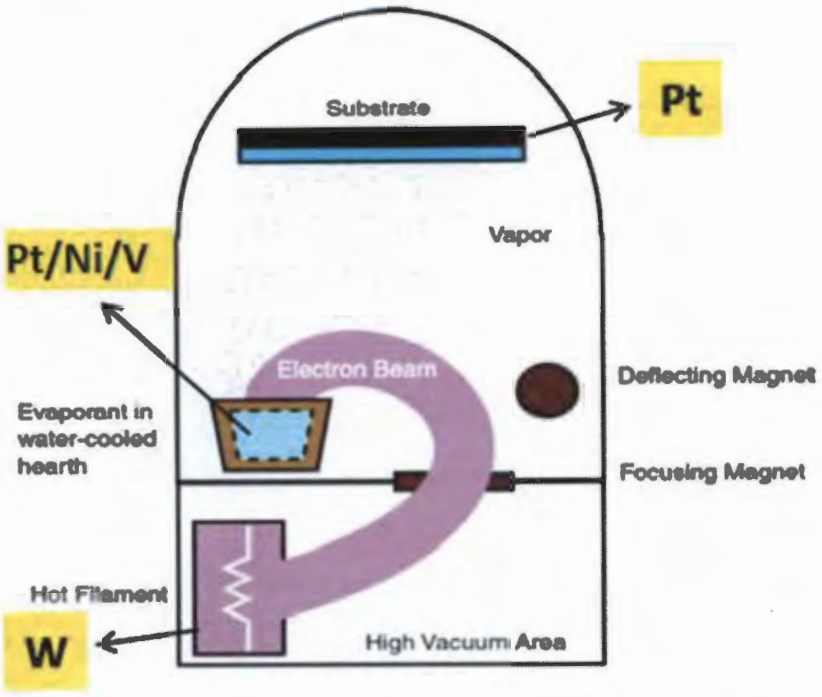

Figure 2.7: Diagram illustrating electron beam deposition[65].

Thin film growth, through physical vapour deposition (e-beam), follows as a result of deposition and condensation of the evaporated atoms on to the surface of a substrate[66]. The characteristics of the substrate surface affect the properties and formation of the thin film being deposited. Such characteristics include[66]:

- Surface morphology, which may lead to affects such as gecmetrical shadowing of the surface (prevention of depositing atoms reaching a particular region of the substrate surface due to a substrate surface abnormality) causing coating porosity. Surface morphology may also alter the angle-of-incidence of the atoms being deposited, thus affecting film growth.
- Homogeneity of the substrate surface can affect uniformity of the film characteristics.
- Surface chemistry, such as contamination (uniform and local), can affect nucleation density and surface-adatom reactions, thus altering the stability of the deposition interface. Particulate contamination may cause pinholes to develop in the thin film coating. Adatoms are evaporated atoms which have reached the substrate surface but have not undergone condensation to the surface .i.e. they are still mobile on the surface.

In figure 2.8 examples of how surface morphology and particulates affect film properties, are shown[66].

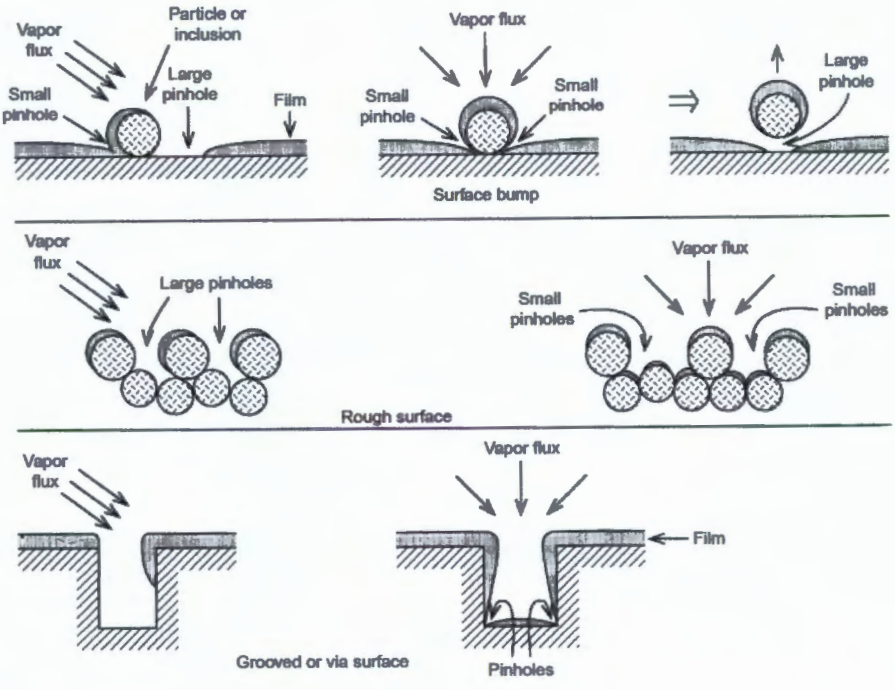

t

Figure 2.8: Effects of surface morphology on pinhole formation and surface coverage[66].

The main stages of thin film growth; the condensation and nucleation of adatoms on the substrate surface, growth of nuclei, interfacial formation and film growth.

Condensation and Nucleation

Evaporated atoms which impact the substrate surface, will either condense on the surface, re-evaporate or are reflected immediately. If these atoms do not immediately condense on the surface, they will have a certain level of mobility across the surface until they eventually condense (adatoms). However, if the bonding energy between the adatoms and surface are weak and the substrate temperature is too high, re-evaporation of the adatoms will occur and a film will not form. In the experimental method used here, substrate temperature were kept at room temperature and so re-evaporation was not a concern[66].

Mobility of the adatoms on the substrate surface is affected by the chemical bonding energy between the atom and surface, crystallography of the surface and surface temperature (as previously described). In terms of the surface crystallography, different planes have different free energies. In fcc metals (such as Pt and Ni) surface free energy of the (100) plane is greater than the (111) with the surface mobility of an adatom being lower on the (100) compared to the (111). This results in different crystallographic planes growing at varying rates during condensation[66].

Adatoms eventually condense on the substrate surface by bonding to other atoms only after they have lost their energy. Adatom energy loss will occur through; collisions with other diffusing surface atoms and adsorbed surface species, chemical reactions with the substrate surface and through finding favoured nucleation sites (e.g. impurities, crystal lattice imperfections, atomic steps). These condensing atoms form chemical bonds with the surface atoms of the substrate in the form of metallic bonds, also known as homopolar bonding, with orbital electrons being shared between the atoms. If this bond between the adatom and surface atom is strong then the surface mobility will be minimal allowing each surface atom to be a nucleation site. If, however, the interaction between surface atom and adatom is weak, mobility of the adatom will be high. The adatom will then condense at a preferred nucleation site where bonding is stronger due to an electronic or elemental change in chemistry or an increase in coordination number (such as a step). In figure 2.9 a diagram illustrating preferred nucleation sites is shown[66].

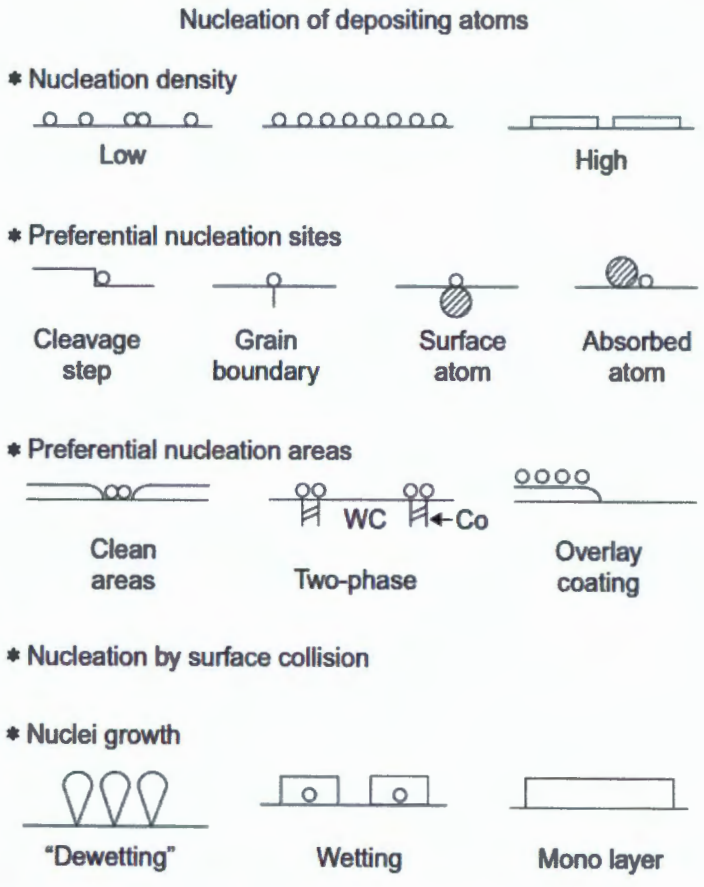

Figure 2.9: Nucleation on a surface showing preferred nucleation sites along with low and high density nucleation[66].

Growth of Nuclei

Nuclei proceed to grow through the addition of more adatoms, with adatoms either migrating over the substrate surface to existing nuclei or by directly impacting the nuclei from source. There are three different types of mechanisms of nucleation. Only the Stranski-Krastanov (S-K) mechanism is relevant to this work as it applies to metal-on-metal deposition at low substrate temperatures with low surface mobility. The S-K mechanism occurs where an altered surface layer is created through the reaction with the deposited metal to generate a pseudomorphic or strained structure. This is followed by cluster nucleation on the altered surface[66].

Separate nuclei on the substrate surface may grow in two ways to form a continuous film; normal to surface growth (dewetting growth) or laterally over the surface (wetting growth). Less material is required to form a continuous film with high nucleation density and dominantly wetting-type growth[66].

Interfacial Formation – Abrupt Interface

An interfacial region may form between the substrate and deposited material through the deposited atoms diffusing and reacting with the substrate. This interfacial region influences the adhesion properties between the substrate and deposited film. There are various types of interfacial regions which can form depending on; the types of materials being worked with, deposition temperatures and deposition times. The interfacial region relevant to the work in this project is known as an abrupt interface[66].

An abrupt interface forms due to lack of bulk diffusion between substrate and deposited material, resulting in a sudden variation from the substrate material to the deposited material in a distance of approximately 2-5Å (atomic spacing). Abrupt interfaces usually signify low deposition temperatures, surface contamination, lack of solubility between substrate and deposited materials or a weak chemical reaction between substrate and deposited material. Nucleation densities are typically low in abrupt interfaces with films needing a significant thickness for uniform coverage. Abrupt interfaces are thus prone to formation of interfacial voids which lead to low adhesion between coating and substrate[66].

Film Growth

Film growth occurs through continuous attachment of evaporated atoms to existing deposited layers, with the surface being constantly covered under newly deposited material. Important facets of film growth include; surface temperature, geometrical shadowing effects, adatom surface mobility, reaction and mass transport during deposition and surface roughness. Surface morphologies can range from being very rough to smooth. Typically, surface roughness increases as the film grows. This is due to faster growth of some crystallographic planes or other features compared to others[66].

Deposited films typically display unique growth morphology in a form looking like logs or columns packed together. This is known as columnar morphology.

Whether a material is amorphous or polycrystalline, columnar morphology is observed and it occurs due to geometrical effects. Typically the columns are not single crystal grains but rather polycrystalline or amorphous. Columnar morphology begins early in film growth and becomes noticeable from a thickness of approximately 100nm[66].

Surface diffusion and geometrical shadowing compete to define the morphology of the depositing material. Peaks on a rough surface receive adatom flux from all directions, under these conditions if surface mobility of adatoms is minimal, peaks will grow faster than valleys due to geometrical shadowing[66].

How smooth (or rough) the substrate surface is has a marked influence on the film characteristics. Typically, deposition of a film on a smooth surface has properties more similar to the bulk properties of the film material than a film deposited on a rough surface[66].

2.4.2 Surface Segregation Energy

The chemical composition of an alloy's surface could be substantially different from the composition of the bulk of the alloy. This may arise due to one of the alloys enriching the surface region of the metal. This is known as surface segregation and it plays an important role in surface chemistry. It has the potential to either enhance or suppress wanted and unwanted chemical reactions on the alloy surface. Surface segregation energy is defined as "the energy cost of transferring an impurity atom from the interior to the surface of a host crystal", or "the difference in the total energies of the system with the impurity in a surface layer and in the bulk"[66].

Density-functional theory (DFT)[7] has been used to determine the surface segregation energies of the transition-metal alloys; values are tabulated in the segregation energy database of Ruban *et al*[61,67,68].

Greeley and Mavrikakis[61] considered surface segregation energies when selecting an appropriate solute metal partner for Pt-based NSAs for hydrogen related reactions (where hydrogen is the adsorbate molecule). There are a multitude of binary alloy combinations available for fabricating NSAs but not all of them are necessarily stable, particularly in hydrogen-rich environments such as the anode of the PEMFC. This stability and thus combination of alloys to be used was determined by means of a two-prong approach[61].

First, under a vacuum, the surface composition of the potential NSA was estimated from the solute/host segregation energy database of Ruban *et al*.The surface layer of the alloy will be pure solute if the E_{seg} is negative and gives rise to an overlayer structure as shown in figure 2.10[61]. On the other hand, if E_{seg} is positive the surface layer will be pure host and we get a subsurface alloy forming (NSA) as seen in figure 2.6[67]. With a positive E_{seg} and annealing, a solute deposited on the host metal surface would segregate to the subsurface layer of the host metal forming a NSA[61]. In the context of the present research, overlayer structures are undesirable.

[7] Density-functional theory is a method used for the initial calculations of the structure of atoms, molecules, crystals, surfaces and how they interact with one another. It is a strong predictive tool for catalysis.

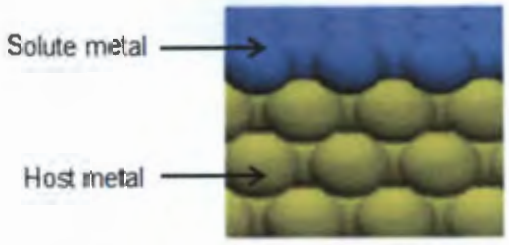

Figure 2.10: Illustration of an overlayer structure[61].

Second, the effect of hydrogen adsorption on the alloy's surface composition was determined. This is important as adsorbates such as hydrogen can potentially draw alloy components to the surface due to strong binding of the adsorbate to the alloy component. An example of this is the Pt-gold (Au) system where hydrogen is able to draw the Pt to the surface of the Au forming an overlayer structure[61].

One can reliably estimate the possibility of hydrogen causing this surface segregation of solute atoms by making a comparison between the E_{seg} of the solute and the difference in magnitude of the hydrogen binding energies (BE_H)[8] of the pure solute and pure host $(BE_H^{sol} - BE_H^{host})$. Thus, if E_{seg} is positive and if hydrogen binds more strongly to the host atoms relative to binding to the solute atoms, then no surface segregation will occur[61].

In figure 2.11 we see a graph illustrating the results of hydrogen-based segregation study for numerous bimetallic systems, showing both NSAs and overlayer structures[61].

[b] Hydrogen binding energy is the change in energy when the hydrogen gas is adsorbed onto the catalyst surface.

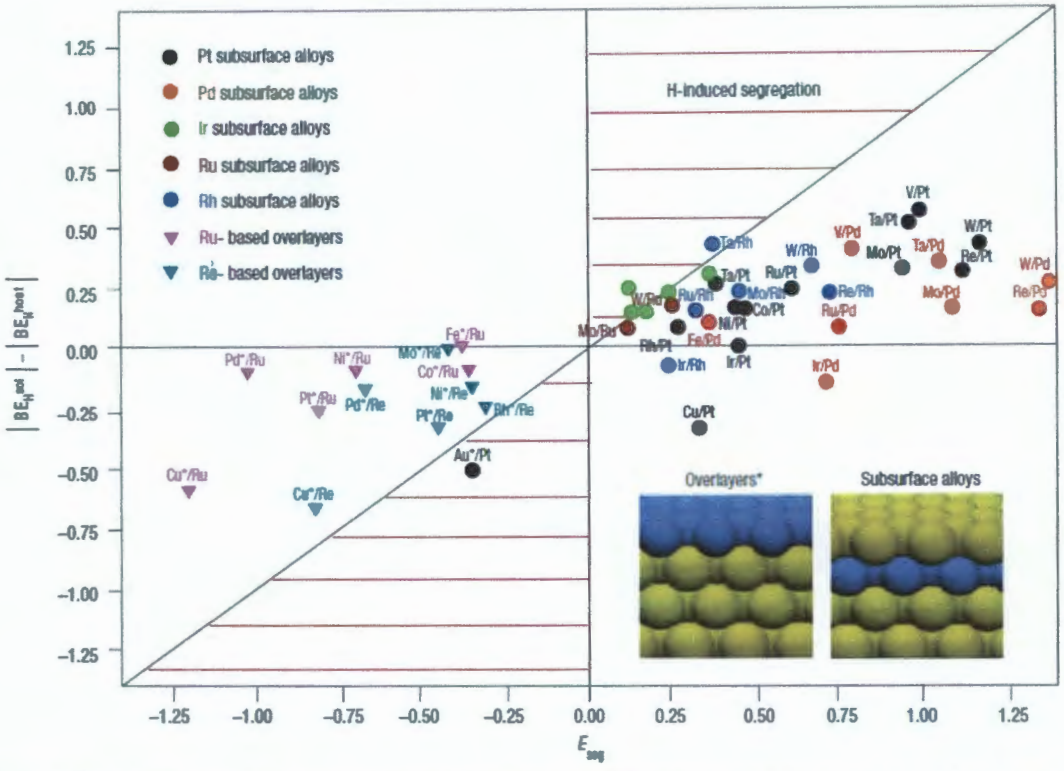

Figure 2.11: A graph of hydrogen binding energy vs. segregation energy for various bimetallic alloys with overlayers forming in the lower left quadrant and NSAs in the upper right quadrant[61].

2.4.3 Idealized vs. Real NSAs

What has been discussed thus far with regards to NSA s has been based on an 'idealized' NSA model in that a total solute coverage of one monolayer in the near-surface region is assumed. In reality though, NSAs differ from this idealized model[61]. Real NSAs are unlikely to have a pure monolayer of solute in the near-surface region[63]. Some of these differences arise from the possibility that some of the solute atoms in the subsurface region can segregate deeper into the host, away from the near surface region. An example of this is the W/Pt (111) NSA where a portion of the W atoms migrate deeper into the host (Pt) metal. In other cases it has been found that atom arrangements have abnormal periodicity or no periodicity at all which may give rise to long-range reconstructions or the formation of defects[61].

These variations in structure between ideal and real NSAs do not substantially affect the adsorbate behavior as described in section 2.4.2. In other words, there are no qualitative changes between ideal and real NSAs.

However, quantitative predictions will vary between real and ideal NSAs. An example is the W/Pt NSA above where deeper segregation of W atoms will result in a lesser decrease in BE_H, but still a decrease relative to either pure Pt or W[61].

2.4.4 NSA Novel Properties

The factors which affect the active site reactivity of catalysts are either electronic or geometric. The electronic effect is comprised of two components, namely the ligand effect and the strain effect. The ligand and strain effects occur together and so it is difficult to elucidate their individual roles[40].

2.4.4.1 Geometric Effects

Geometric effects occur due to differing geometries of the catalyst active sites. Examples of such geometries include kink sites, two fold sites, three fold sites and flat surfaces. By altering the structure of a particular transition metal, one can change the d-band center. The coordination number of the metal dictates the bandwidth, resulting in the changes in the d-band centers. In the case of Pt, the atoms in the most close-packed (111) surface have a coordination number of 9, whilst in the open (100) surface the coordination number is 8[40,69].

With kinks, the coordination number can be as little as 6. It has been determined that high coordination number sites have weak reactivity, binding adsorbates weakly. Conversely, at lower coordination number sites the d-bands are of higher energy and bind adsorbates more strongly[40,69]. An example of this was shown with OH poisoning where it was determined that low coordination sites, such as kinks, bind OH^- ions strongly[40,45]. This OH poisoning was found to be one of the sources of overpotential for the ORR in PEMFCs[40,45,69].

Further evidence of the geometric effect is shown by Pt surfaces which have a propensity to reconfigure into overlayer structures which have a larger density of Pt atoms than the close packed (111) surface[69,71].

Due to this higher density of Pt atoms, we see a larger bandwidth and lower d-bands resulting in these Pt overlayer surfaces binding CO more weakly than the Pt (111) surface[69].

2.4.4.2 Electronic Effects

The electronic effect refers to "changes in the physicochemical properties of the surface atoms due to altered electronic structure of the topmost atoms."[72]. It is comprised of the strain and ligand effects.

(a) Strain Effect

Computational studies have been carried out in order to distinguish the effects of strain from ligand effects[40,73,74]. This effect arises when a metal surface takes on a different two dimensional surface lattice parameter from the bulk parent lattice. A strain can be introduced into a metal surface by pseudomorphic growth, which can be seen in figure 2.12[40,74].

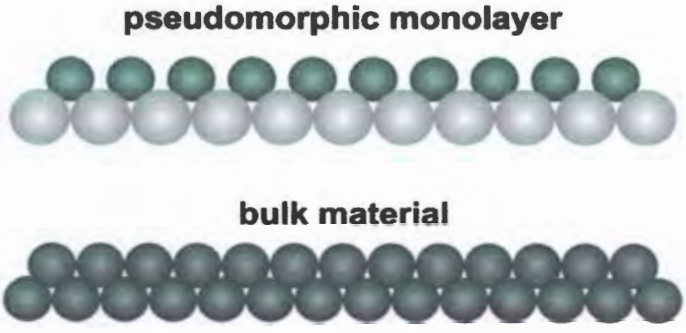

Figure 2.12: Pseudomorphic growth leading to a strained overlayer[40,74].

This strain effect results in changes in the metal's electronic structure by altering the orbital overlaps. Based on this, if the surface atoms experience a compressive strain then the d-orbital overlaps increase with subsequent widening of the bandwidth and thus a decrease of its d-band center (average energy $\Delta\varepsilon_d$).

This compressive strain effect results in the adsorption energies of simple adsorbates, such as hydrogen (and carbon monoxide), to decrease in comparison to hydrogen adsorption on the pure/parent metal surface.

In other words, the hydrogen binds more weakly to the alloy surface compared to the pure/parent metal[2]. This is illustrated in figure 2.13[50].

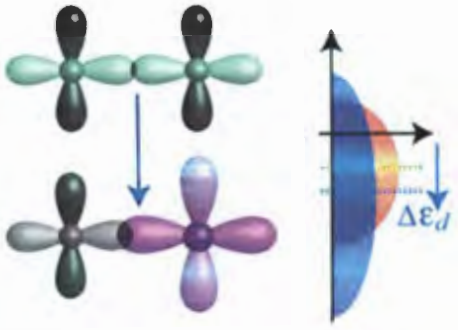

Figure 2.13: Compressive strain resulting in increased d-orbital overlap, a widening of the bandwidth and decrease of the d-band center[50].

The reverse occurs when the surface atoms experience a tensile strain (lattice is expanded); there is a decrease in d-orbital overlap leading to a narrowing of the bandwidth and a subsequent increase in its d-band center. Adsorbates such as hydrogen now have increased adsorption energies and thus bind more strongly to the alloy surface compared to binding the pure/parent metal surface[2].

Electronic effects can be further explained by the rectangular d-band model as seen in figure 2.14[40,74]. It shows that the primary reason for a shift in the d-band center is due to variations in the interatomic distances between atoms in an overlayer. In order to conserve the metal d-band electron filling at the Fermi level (ε_F), the d-band center needs to decrease when subjected to a compressive strain or increase when subjected to a tensile strain[40,74].

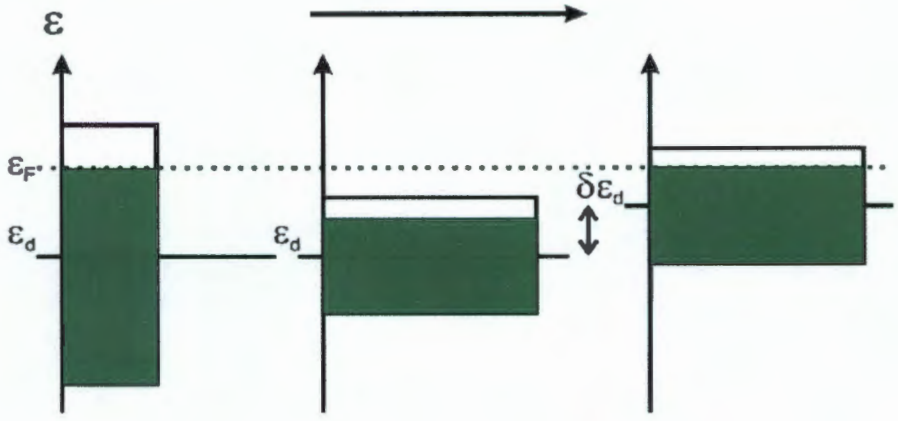

Figure 2.14: Rectangular d-band model describing effects of compressive and tensile strain on the d-band center[40,74].

Strasser *et al*[75] confirmed the strain effect by demonstrating the high catalytic activity of a dealloyed[9] Pt-copper (Cu) system ($PtCu_x$). The catalyst had a Pt-rich shell over a Pt-Cu core[76]. They showed a 4-6 fold improvement in catalytic activity over pure Pt and were able to directly correlate this improvement to strain effects.

(b) Ligand Effect

The ligand effect occurs due to the bonds that form between the subsurface solute metal and the parent metals surface atoms. This bimetallic nature at the near-surface region can result in changes in the electronic structures of the two metals. These changes in electronic structure may give rise to dramatic variations in the metals chemical properties[40,77]. Although it has been determined that the ligand effect becomes insignificant if the solute layer is further than three atomic monolayers from the surface, NSAs where the solute layer is within 3 atomic monolayers from the surface have been successfully employed in "fine" tuning chemical properties of catalyst surfaces[39,40,45].

Experiments have been reported by Chorkendorff *et al*[39] where Pt/Cu(111) single crystals were used to validate the ligand effect. By varying the amount of subsurface Cu in the NSA, they were able to fine tune the catalytic efficacy of the PEMFC cathode for the ORR, increasing the kinetics by a factor of 8. Ultimately they were unable to decisively verify that this enhancement was solely due to the ligand effect[39,40].

[9] "Dealloying is a common corrosion process during which an alloy is "parted" by the selective dissolution of the electrochemically more active elements."

Another experiment carried out in order to verify the ligand effect was by Kitchin *et al* [2]. Here DFT calculations were performed on Pt NSAs with a subsurface layer of 3d transition metal atoms. The 3d atoms were in the second monolayer.

In this scenario it was known that the surface was not strained and so any alterations in chemical properties would be as a result of the ligand effect alone. Their results verified the ligand effect, showing that it was strong when using the early 3d transition metals but weak with the late 3d metals[2,40]. The ligand effect is related to a parameter known as the matrix element (V_{dd}), which determines the coupling between metal states and the strength of the bond between the 3d solute metal and surface parent metal[40,78].

2.4.5 NSAs and H_2 Oxidation

With regard to the hydrogen oxidation reaction of the PEMFC, one desires a catalyst which is able to bind H_2 weakly, dissociate H_2 into H^+ easily and not be poisoned by carbon monoxide (CO) which is often present in hydrogen gas feeds[2]. The hydrogen fuel used in the cell is often obtained from a steam reforming process. This process leads to small amounts of CO always being present in the hydrogen gas feed. These small amounts, sometimes even trace amounts of CO are sufficient to poison the Pt anode, thereby reducing the efficacy of the fuel cell[63]. CO poisons the Pt anode by remaining bound to active sites on the catalyst surface and so limiting the number of active sites available for hydrogen to bind to. This poisoning effect increases the overpotential from approximately 50mV to 700mV[78].

One can enhance resistance to CO poisoning by altering and modifying the catalyst surface (i.e. the electronic structure) in a manner that causes CO to bind more weakly to the catalyst surface and in so doing minimizing the CO coverage. To achieve this one can alloy Pt with a transition metal such as nickel (Ni). Creating a PtNi NSA causes surface modifications in the catalyst whereby its d-band center is lowered. This lowering of the catalyst surface d-band has the effect of lowering the adsorption energy of CO[2,79].

The lowering of the d-band is a result of the interaction and sharing of electrons between the electron rich d-band of Pt with the electron poor d-band of the transition metal (Ni)[80]. The two graphs in figures 2.15 and 2.16 illustrate the effects of CO poisoning on pure Pt and the Pt/Ru NSA[25].

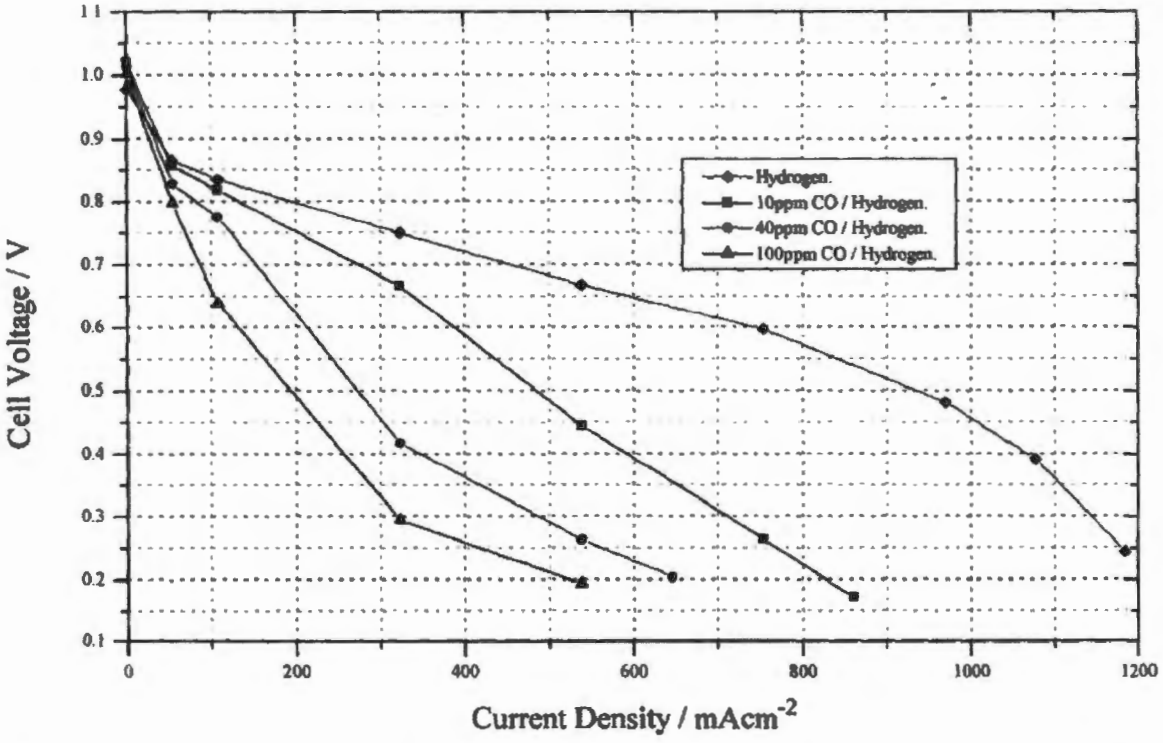

Figure 2.15: Graph of voltage vs. current density illustrating the effects of CO poisoning of the pure Pt anode for the hydrogen oxidation reaction of the PEMFC[25].

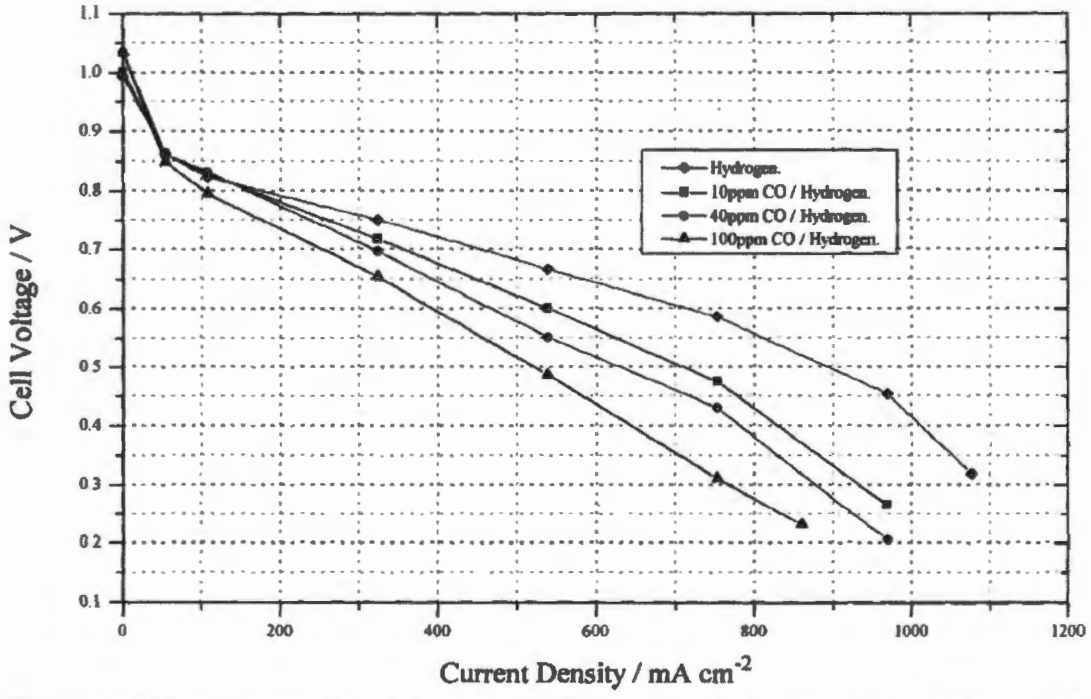

Figure 2.16: Graph of voltage vs. current density illustrating the PtRu NSAs resistance to CO poisoning for the hydrogen oxidation reaction in the PEMFC[25].

The effects of CO poisoning on the pure Pt catalyst are clearly evident in figure 2.15 where current density drastically drops from 1200 $mAcm^{-2}$ to almost 500 $mAcm^{-2}$ (more than halving) as CO concentration increases. When PtRu is used as the catalyst one can see a dramatic change in the plots. Here the current density only drops by approximately 200 $mAcm^{-2}$, illustrating the marked efficacy of NSAs in resisting CO poisoning.

There is a trade-off however in that if the surface d-band center is lowered too much then hydrogen adsorption becomes energetically unfavorable making the electrode unsuitable as a fuel cell anode[2]. One needs to make an informed decision as to which transition metal to use as a solute with the host Pt in the NSA.

2.4.6 NSAs and the Oxygen Reduction Reaction

Alloying Pt with transition metals in the NSA format shows promise for exciting and novel surface electrochemistry regarding the cathodic reaction in PEMFCs. These PtM alloys are shown to be 2 to 4 times more active than pure Pt for the reduction of oxygen[81]. Potential reasons for this increase in activity include[81]:

- Altering of the electronic structure of Pt in such a way that the Pt-OH bond energy is affected.
- Modifications to the geometric structure of Pt with regards to the Pt-Pt bond distance and coordination number.

In this reaction again, the position of the d-band center is what describes the relationship between the electronic structure of metallic surfaces and the heat of adsorption of small molecules (H_2, O_2 and CO)[81].

Desirable properties for the cathode, as for the anode, include easy dissociation of O_2 into O^- while not binding too strongly to the resulting oxygen adatoms (O^-). Enhanced catalysis has been reported for Pt/M NSAs, especially with PtNi, relative to pure Pt[2].

In this reduction reaction, it was shown that O_2 adsorption was the rate-limiting/determining step and that using the Pt/M NSA enhanced the surface-oxygen interaction leading to increased O_2 coverage and subsequent dissociation. The trade-off in this scenario is that by decreasing the dissociative adsorption energy of oxygen the dissociation barrier of O_2 to O^- is increased[2].

A benefit in this is that a more weakly bound O^- adatom may potentially be more reactive than a more strongly bound one and so the rate of the reduction reaction is ultimately increased[2].

The weak adsorption of oxygen to the NSA surface occurs for the same reasons described in the hydrogen oxidation reaction above[2]. With regard to the issue of OH poisoning which arises from the strong bonding between pure Pt and OH[30], it is predicted that due to the weak binding of oxygen to the NSA surface the same rules would apply to the binding of OH. OH binding would thus be weak and so poisoning would not be an issue as the OH would be easily released from the NSA surface, in this way not clogging up active sites[2].

Another very interesting prospect in the prevention of OH poisoning is the replacing of some of the Pt metal in the NSA surface layer with a transition metal (e.g. Ir, Ru). The theory is that the transition metal will attract initial OH molecules and in so doing will induce repulsion on adjacent Pt-OH groups. The result is decreased OH binding and coverage with an increase in available Pt active sites[30]. Figure 2.17 illustrates this concept[30].

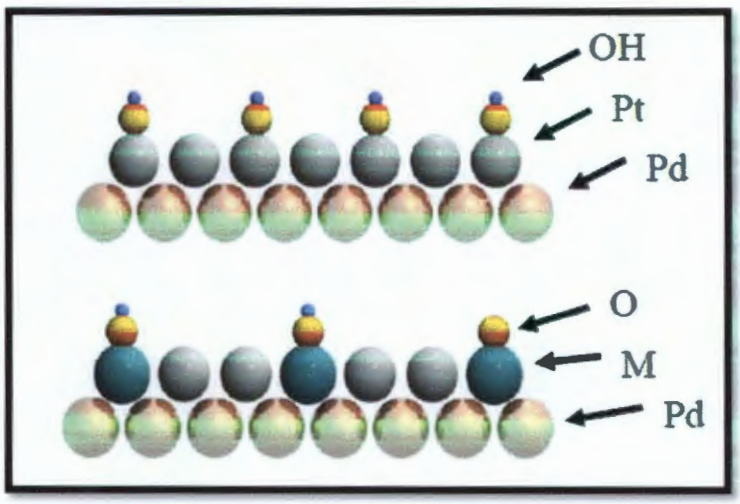

Figure 2.17: Illustration of induced repulsion of OH with PtM surface[30].

Based on the literature, the following bimetallic alloys are promising candidates for the PEMFC anodic and cathodic reactions: (alloys are in NSA format with Pt being surface species and non-Pt metals being the subsurface alloy)

- Anode: **Pt** surface with either **Ni**, **Re**, **Rh**, **Ru**, **Ta**, **V** or **W** as the subsurface metal[30,61].
- Cathode: **Pt** surface with either **Co**, **Fe**, **Ir**, **Ni**, **Rh**, or **Ru** as the subsurface metal[2,30,45,81].

CHAPTER 3

EXPERIMENTAL PROCEDURE

3.1 Materials

The materials used in this project were platinum (Pt), nickel (Ni) and vanadium (V). Pt was obtained from *Perkins Metals* in the form of recycled granules of total mass 57g. Approximately 40g of the Pt was used as the substrate material on top of which the nano–layers of Ni and V were deposited. The remaining platinum was used as the target for evaporation in e-beam deposition. With regards to the NiPt sample, the Pt evaporant target was supplied by iThemba labs. An additional 1g of Pt, as received from *Perkins*, was used as a reference of purity against the above 57g of Pt. Nickel and vanadium used as substrates were also obtained from *Perkins Metals* as 100% pure ingots. The Ni and V evaporant targets used for e-beam deposition were supplied by iThemba Labs. Only the mass of Pt is given as it was the limiting material due to the high cost.

3.2 Sample Preparation

Firstly, the 57g of platinum granules were melted into a single Pt button using the *ICON 3CS Hot Platinum Induction Furnace* in new, clean ceramic crucibles. The 1g of additional Pt including the Nickel and vanadium used for substrates were already in button form and needed no melting.

All preparation steps carried out apply to the Pt, Ni and V substrates including the additional 1g of Pt. The buttons were rolled using the *Dinkel Laboratory roller* to a thickness of 0.2mm for Pt and 1mm for Ni and V. After rolling, each metal sheet was then cut into squares of 15mm x 15mm using the *Buehler Isomet micro cutter*. The cut metal squares were then hot mounted in *Struers ClaroFast hot mounting resin* using the *Struers LaboPress-3* in preparation for grinding and polishing. The mounted samples were then ground using the *Struers LaboPol–25 grinder* with the 1200 grit silicon carbide grinding pads. Samples were ground until a planar surface was obtained. Samples were then polished using the *Struers TegraForce-1, TegraDoser-5* and *TegrPol-11* auto polisher. Samples were first polished with 9µm diamond paste on a *Struers MD-Dac cloth*, followed by 3µm on a *Struers MD-Mol cloth* and finally with OP-S on a *Struers MD-Chem cloth* to a mirror finish.

Between each increment of polishing paste, sample surfaces were cleaned with pure ethanol-alcohol and then distilled water. Samples were then carefully removed from the resin in preparation for cleaning. Samples were sequentially cleaned in individual beakers of pure methanol, ethanol, acetone and distilled water in the *Fritsch laborette ultrasonic cleaner*.

Only Pt and Ni were used as substrates in e-beam deposition. To improve their surface quality, in order to assist in the e-beam coatings to adhere to their surfaces effectively, the Pt and Ni polished samples were placed in 5% Hydrofluoric acid for approximately 5 seconds. Substrate temperature during e-beam deposition was kept at room temperature. Variation in temperature between substrate and deposited metal should have no significant impact on adhesion between the substrate and coating, as advised by the assisting professor, C. Pineda. This is also evident in the lack of peeling in the NiPt sample. However, peeling may be a result of abrupt interfaces forming as described in section 2.4.1[66].

The Pt and Ni substrates were then taken to iThemba labs to be coated with nano-layers via their *Varian 3117 E-Beam Evaporator*. Table 3.1 shows the various important parameters for the depositions. Under the 'NSA' column, the bold element is the substrate metal, whilst in the 'Element Deposited' column, the elements occur in the order they were deposited onto the substrate.

To measure film thickness during deposition, the e-beam evaporator at iThemba Labs makes use of a quartz crystal monitor which operates on a principle called the piezoelectric effect. When a free-running RF (radio frequency) voltage is applied to the quartz crystal, it vibrates at its natural frequency. This frequency remains stable unless the crystal's mass changes. Depositing a thin film on the crystal's surface will change the mass of the crystal. The increase in mass from the deposition causes the resonant frequency of the crystal to lower. Such changes are easily detected electronically and converted into thickness measurements. The thickness and rate are calculated from user supplied data on density and acoustic impedance of the film material. The user also specifies a tooling factor to compensate for differences in detector/substrate geometry. Deposition may be automatically terminated at a specified thickness by remote operation of a shutter door. The quartz crystal monitor uses a 6MHz oscillator and a high accuracy quartz microbalance controller, offering a thickness resolution of 0.1nm. The thickness range is 0 - 999.9microns and a rate of deposition of 0 - 999.9nm/s.

Since heat also changes the frequency of the vibration of the crystal, the quartz crystal monitor was water-cooled to improve the accuracy of readings.

Table 3.1: Parameters of e-beam deposition for NSA samples prepared.

#	NSA	Substrate	Element Deposited	Thickness of Deposition (nm)	Deposition Rate (Å/s)	Applied Current (mA)	Pressure ($x10^{-6}$ mbar)
1	**Pt**/Ni	Pt	Ni	3	1.2	30	4
			Pt	3	1.2	150	4
2	**Pt**/Ni	Pt	Ni	5	1.2	30	4
			Pt	5	1.2	150	4
3	**Pt**/V	Pt	V	3	1.2	20	4
			Pt	3	1.2	150	4
4	**Pt**/V	Pt	V	5	1.2	20	4
			Pt	5	1.2	150	4
5	**Pt**/Ni	Pt	Ni	3	1.2	30	4
6	***Ni**/Pt	Ni	Pt	5	1.2	150	4

The deposition rate was controlled by the magnitude of applied current, as the current being applied to the evaporant metal is what causes it to vaporize. The lower the deposition rate the greater the uniformity of the layer being deposited. The above deposition rates were the lowest possible rates that could be achieved. Complete evaporant coverage over the substrate is achieved.

With regards to the second last sample fabricated in the table 3.1, namely (5) Pt/Ni, after deposition of the 3nm Ni coating onto the Pt substrate was completed these samples were subjected to a heat treatment in order to complete NSA fabrication. The Pt/Ni samples were heat treated in an *Elite Thermal Systems Limited* vacuum furnace at 500°C for 4 hours. The samples were furnace cooled under vacuum until room temperature was reached. The purpose of this heat treatment was to allow for the segregation of Ni from the surface of the Pt substrate down into the subsurface/near-surface region of the Pt to form the NSA as described in section 2.4.2[61-63,67].

As described in section 1.4, under project limitations, the presence of the 3nm Ni coating before heat treatment (and lack of it after heat treatment due to segregation) could not be verified by the techniques available for this project.

As can be seen in the Pt – Ni phase diagram at 500°C (fig. A.2), the following phases and intermetallic are possible; $NiPt_3$, NiPt, Ni_3Pt and (Ni,Pt)[82]. Based on the theory described in section 2.4.2 and that the weight % of the 3nm Ni coating is less than 1% relative to the Pt substrate (as seen in fig. A.2), it is highly unlikely that any of the above phases would be produced but rather segregation of the Ni into the subsurface of the Pt substrate[61-63,67].

No vanadium-based samples were fabricated in this manner due to how readily vanadium oxidizes. If oxidation was not a factor and heat treatments of Pt-V samples were carried out, it can be seen in fig. A.3 at 500°C that many variations of Pt-V phases are possible[83]. However, as previously discussed, Based on the theory described in section 2.4.2 and that the weight % of a 3nm V coating is less than 1% relative to the Pt substrate (as seen in fig. A.3), it is highly unlikely that any binary phases would be produced but rather segregation of the V into the subsurface of the Pt substrate. Possible phase transformations due to interdiffusion of Pt and V were considered, however prior work has shown that phase transformations do not occur at temperatures below 700°C, consistent with the bulk phase diagram[83]. Since no heat treatments were carried out for Pt-V samples, it is concluded that interdiffusion was minimal to non-existent.

Four Pt substrates from the 57g batch were annealed in the *LaboFurn box furnace* at 1000°C for 8 hours. The samples were then allowed to furnace cool. Vacuum was not necessary as Pt does not oxidize at this temperature. The purpose of this heat treatment was to allow for recrystallization of the Pt after being cold worked during rolling.

Table 3.2 shows a list of all the samples fabricated, via the above described sample preparation protocols, for testing in this research project along with a basic schematic of the sample to illustrate its structure. Illustrations are not to scale with all samples being in the solid phase.

*The (6) Ni/Pt sample was initially intended as a NSA sample but it was later found that the thickness of the Pt coating masked any NSA attributes. Thus, along with the stability of the single Pt coat, pure Pt was being analysed with the Ni substrate serving merely as a platform for the Pt coating. Due to the Pt being evaporated onto the Ni surface, the Pt was of highest purity, free of any possible contamination arising from recycling and the lab preparation protocol. Thus, the first four samples in table 3.2 are pure metals and not of the NSA structure. These were used as references in the Tafel analysis.

The remaining five samples in table 3.2 are all of the NSA structure. The names given to the samples in table 3.2 will be used from here on, throughout the text.

Based on the method of screening in section 2.4.2, Pt/Ni and Pt/V were selected as candidates for NSA fabrication and study. Both NSA samples have positive segregation energies and thus do not form overlayer structures, and neither alloy suffers hydrogen-induced segregation.

It must be noted that due to the high cost of Pt metal, only a limited number of Pt substrates could be prepared for each round of testing. Each sample was only tested once with regards to the Tafel scan. After analysis, coatings were polished off the Pt surfaces and re-used; while after approximately 3 rounds of testing Pt substrates were sent for complete recycling at *Perkins metals*.

Table 3.2: List and illustrations of all sample types fabricated and tested.

Name	Structure
Pt Pt (annealed)	
NiPt (used as pure Pt)	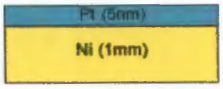
Ni	
V	
PtNi (3nm)	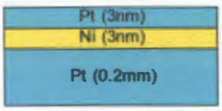
PtNi (5nm)	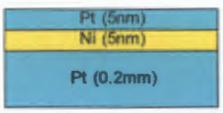
PtV (3nm)	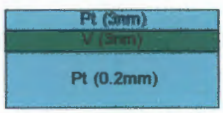
PtV (5nm)	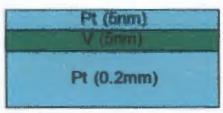
PtNi (heat treated)	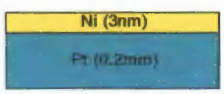

3.3 Analysis Techniques

3.3.1 Electrochemical Analysis

All the experiments described in this section on electrochemical analysis were carried out using the *Ametek Princeton VersaSTAT 3 Potentiostat* in the electrolytic *Ametek Princeton Flat Cell* as shown in figure 3.1.

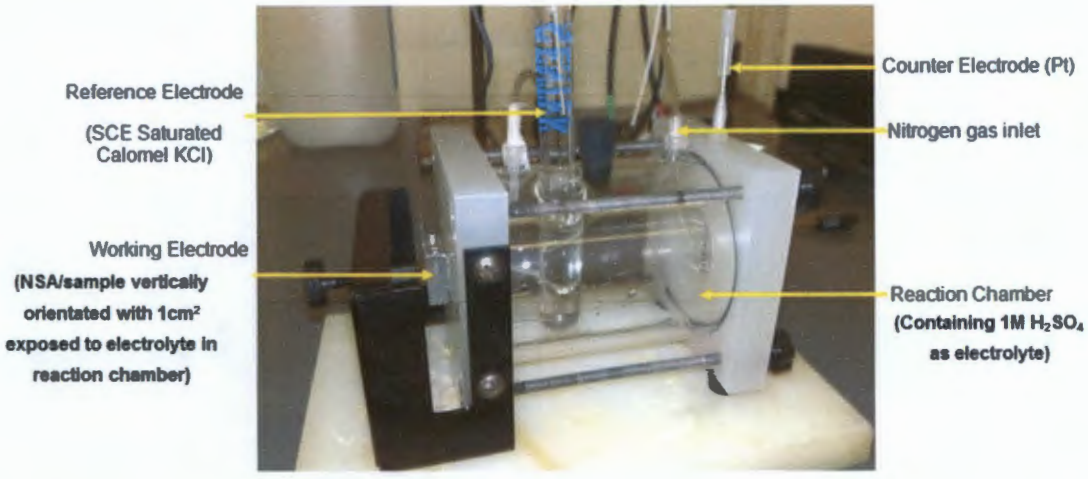

Figure 3.1: Photograph of the electrolytic *Ametek Princeton Flat Cell* in which Tafel tests were run.

(a) ASTM G5 - 94

This is a standard reference test method for making potentiodynamic and potentiostatic polarization measurements. This standard test is carried out in order to ensure the potentiostat used for electrochemical testing is functioning properly. The standard was run before each round of testing fabricated samples to confirm proper functioning of the electrochemical equipment. Test parameters were strictly adhered to according to the ASTM G5 – 94 Standard manual.

(b) Tafel Plot Analysis

Tafel Plot analysis was the primary technique used in the electrochemical analysis of all the samples illustrated in table 3.2. It is a direct current (DC) method whereby a small potential is applied to the sample (working electrode) and the current which arises on the surface of the sample as a result of this potential is measured and displayed as a graph of potential vs. log current. It is a useful technique for the calculation of a metal's exchange current density. The exchange current density of the fabricated samples was determined using this technique.

All tests were carried out at room temperature (25°C) and at standard atmospheric pressure (101.325 kPa). 250ml of fresh, 1M Sulphuric acid ($H_2SO_{4\,(aq)}$), pH~0 was used as an electrolyte for each test. Test samples were vertically orientated with a $1cm^2$ area exposed to the electrolyte for analysis. Before a Tafel Plot analysis was initiated, the sulphuric acid electrolyte within the reaction chamber was deaerated with 99.99% pure nitrogen gas ($N_{2\,(g)}$) for 60 minutes at a flow rate of approximately 2.0×10^{-6} m^3/s. It was found that the open circuit potential (OCP) of the test sample stabilised after 60 minutes of deaeration. Nitrogen gas flow was maintained at the above flow rate throughout the entire Tafel Plot analysis. In table 3.3 the parameters for the Tafel Plot analysis are shown.

Table 3.3: Parameters of the Tafel Plot analysis.

Endpoint Properties	Value	Measured versus
Initial Potential (V)	-0.25	vs. OCP
Final Potential (V)	0.25	vs. OCP

Scan Properties	Value
Step Height (mV)	2
Step Time (s)	1
Scan Rate (mV/s)	2

In figure 3.2 we see a Tafel Plot analysis of a pure Ni sample tested in this project. This figure illustrates how one is able to graphically determine the exchange current density as is further discussed below.

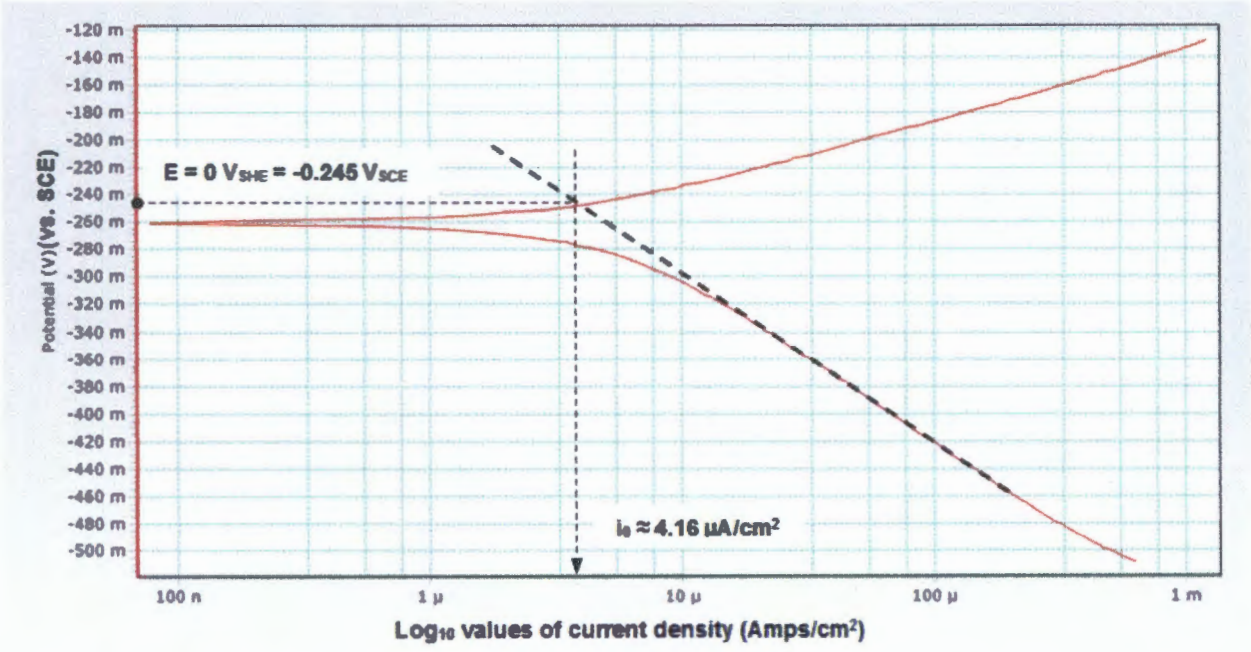

Figure 3.2: Tafel Plot analysis of potential (vs. SCE*) vs. log current density for a pure Ni sample. Graph shows extrapolation method for determining the exchange current density (i_0) as described below.*SCE = Saturated Calomel Electrode, SHE = Standard Hydrogen Electrode.

As previously mentioned, the Tafel Plot analyses carried out on all samples pertains to the hydrogen reduction (evolution) reaction kinetics.

Due to the concentration of dissolved hydrogen not being controlled during the experimental analysis used here, the equilibrium potential (E_0) was not defined. Running Tafel analyses at the correct potentials would result in hydrogen reduction (evolution). Thus, hydrogen pressure was then taken to be approximately 1 atmosphere. The equilibrium potential was then defined as;

$E_0 = 0\ V_{SHE} = -0.245\ V_{SCE}$

The exchange current density was then calculated using the experimentally determined Tafel plots of E vs. log I by extrapolating the current density to E = -0.245 V_{SCE} (E = 0 V_{SHE}) as shown in fig. 3.2. This extrapolated current density is the exchange current density (i_0).

In fig. 3.2 the exchange current density is shown to be $i_0 = 4.16 \mu A/cm^2$ for hydrogen reduction on pure Ni. This value is then converted to a more easily comparable number by using the following formula:

$$\log_{10}[i_0 / (A/cm^2)] = \log_{10}(4.16 \times 10^{-6}) = \underline{-5.3}$$

This i_0 value can now be used to compare against i_0 values for hydrogen reduction on Ni in scientific literature and against the other samples tested in this project.

3.3.2 Light Microscopy

The *Leica Reichert MeF3-A Inverted Light Microscope was* used to take micrographs of the fabricated samples before and after testing. Images were taken of the sample surfaces (post-electrochemical testing using differential interference contrast microscopy (also known as Nomarski interference contrast) at 5x, 10x, 20x and 100x magnifications.

Nomarski interference was selected to emphasize the surface profile of the samples. It was especially useful in identifying any scratches present on the sample surface as this would affect Tafel Plot analysis results.

3.3.3 Profilometry

The profile and surface roughness of the fabricated samples was measured using the *Taylor-Hobson Surtronic 3P Profilometer.* Measurements were taken subsequent to electrochemical and microscopic analysis of the reacted surfaces. As with light microscopy, this technique was employed to gauge the surface roughness of the fabricated samples. The manner in which the measurements were taken is illustrated in figure 3.2.

Blue circles in figure 3.2 represent the reacted surface of the fabricated samples with black dashed lines showing the path of the profilometer needle. Each of the above four measurements was run 5 times each and the resulting Ra-values (roughness average-values) were averaged. The range for the Ra-values was 99.99 µm with a cut off of 0.8mm (distance the profilometer pin travelled along sample surface).

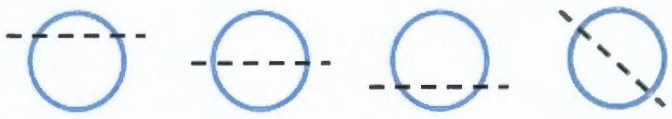

Figure 3.3: Illustration of Profilometer measurements taken in plan view of NSA surfaces.

3.3.4 Proton Induced X-ray Emission (PIXE)

MicroPIXE is a technique whereby the test samples surface is bombarded with protons, which in turn displace electrons in the sample out of their energy orbitals. Other electrons in the sample then drop out of their higher energy electron orbitals to replace the displaced electron so as to balance the energy state of the atom in the sample. Movement of these electrons in replacing the displaced electrons results in x-rays (characteristic to the particular element being analysed) to be emitted[84]. These x-rays are then detected by a Silicon-Lithium crystal and the data is analysed.

This technique provides a quantitative analysis of the elements present in a sample. The technique is very sensitive and is able to pick up trace amounts of elements which other methods such as EDS fail to do[84].

This technique was used to analyse the surface composition of the fabricated samples and to determine if any impurities were present as these would affect the Tafel Plot analysis.

Fabricated samples were analysed using the *Van De Graaff Accelerator* at iThemba Labs. The particle beam consisted of protons of energy 3.0 MeV with a beam size of approximately 3 x 3 μm^2. The scan size was 128 x 128 pixels with a mapping size of 900 x 900 μm^2. The total integrated charge was ~100nC and the scattering angle 135°. Samples were kept under vacuum of ~10^{-6}Torr during testing. An important parameter to note is that beam penetration into samples was between 1-2µm. With samples being at least 200µm thick, there would be no false readings or detection from the sample mounting stage.

Since the thickness of the Ni and V layers were very thin from the point of view of PIXE the following assumptions were made in order to be able to analyse the PIXE spectra using the software package Geo-PIXE:

- For the Ni (or V) deposited over thick Pt, the Ni (V) content was assumed to be part of the bulk composition on the surface. Therefore a chemical formula of the form Pt_x-Ni_y was used to simulate the PIXE spectrum. In other words the PtNi and PtV systems equated to a Pt bulk material with some small content of Ni (V). In addition, any trace element found in the bulk up to the total depth of analysis using the 3.0 MeV protons was determined.

Although we are reporting values in ppm for the trace elements, these values may vary substantially over the whole area of the total sample. Please note the effective area analysed in the PIXE experiment was of 500 micrometers (within the electrochemically analysed area) which is just a small portion of the total surface-sample area.

It must be noted that due to limited Pt availability, only one of each of the fabricated NSA subtypes was analysed by PIXE.

3.3.5 Rutherford Backscattering Spectrometry (RBS)

RBS is especially useful in the analysis of near-surface layers in solids. The sample is probed with alpha particles i.e. helium ions (He^+) and the energy and yield of these alpha particles is measured. The backscattering profile for all elements is known so it is possible to acquire a quantitative compositional depth profile of a sample from the RBS spectrum generated in the analysis[85,86]. This technique was used for determination of the thickness of the nano-layers.

Alpha particles of energy 2.0 MeV were used in probing the fabricated samples which were kept under vacuum during analysis. The total integrated charge was ~20000 nC with a scattering angle of 165°. A circular beam of 2mm diameter was used. The penetration depth of the alpha particles was in the order 1μm. The software package SIMNRA was used to simulate and analyse the RBS results. The units used by the SIMNRA simulation code are atoms/cm^2. However, these units can be converted to nm using the equation:

10^{15} atoms/cm^2 = (1.661 x 10^{-2} M[a.m.u] / density [g/cm^3]) nm, where M is the atomic mass of the material.

The analysis by RBS was complicated for the case of the Ni (V) layer over Pt Substrate since the content of Ni (V) as a layer was very small (the Ni and V coatings were too thin, with the alpha particles passing right through them into the Pt substrate). Although penetration depth of the alpha particles was greater than the coating thicknesses, small amounts of Ni (V) on a thick Pt substrate are not easy to determine by RBS since the scattering cross sections for Ni (V) are too small as compared with those of Pt. Therefore only the results for the case of a Pt layer over the thick Ni substrate are meaningful from the RBS point of view.

It must be noted that due to limited Pt availability, only one of each of the fabricated NSA subtypes was analysed by RBS.

3.3.6 Energy-Dispersive X-ray Spectroscopy (SEM-EDS)

An elemental analysis was carried out on the 57g batch of Pt and on the additional 1g of Pt using the *Nova NanoSEM 230* scanning electron microscope. This was done to identify if any impurities were present. Scans were done under vacuum using a 20keV beam across 5 points of the sample surface. Using the energy of the electron beam and the density of Pt, penetration depth of the beam into the Pt surface is calculated to be 0.3μm. Contaminants concentrations of only down to 1% are detectable by this method. PIXE was not available for elemental analysis of these samples. Coated samples (NSAs) were not analysed with this technique as only the presence of contaminants in the bulk Pt was of importance (the same bulk Pt used as a substrate for the coated NSA samples).

CHAPTER 4

RESULTS AND DISCUSSION

This chapter deals with the results and discussion of the experiments that were conducted on the pure reference metals followed by the near-surface alloys. Initially the pure metals (Pt, Ni, and V,) which were used as a reference for the NSA samples, are investigated. Thereafter the nickel-based (PtNi 3nm, PtNi 5nm, PtNi heat treated) and vanadium-based NSAs (PtV 3nm and PtV 5nm) were investigated. Further results can be found in appendix chapters 8.2 and 8.3. Here overlaid Tafel plots demonstrate reproducibility[87] of electrochemical results along with Ra-value tables and SEM-EDS spectra.

4.1 Pure Metal References

4.1.1 Nickel

Figure 4.1 shows a Tafel plot of a Ni sample analysed. The resulting log i_0 calculated for the hydrogen reduction reaction of the sample is approximately -5.3 (according to the method outlined in section 3.3.1.b). This value of -5.3 is consistent with that found in the literature, under the same test conditions, of i_0 = -5.2[57-60]. This indicates that the Tafel analysis ran without fault and that the Ni behaved as expected.

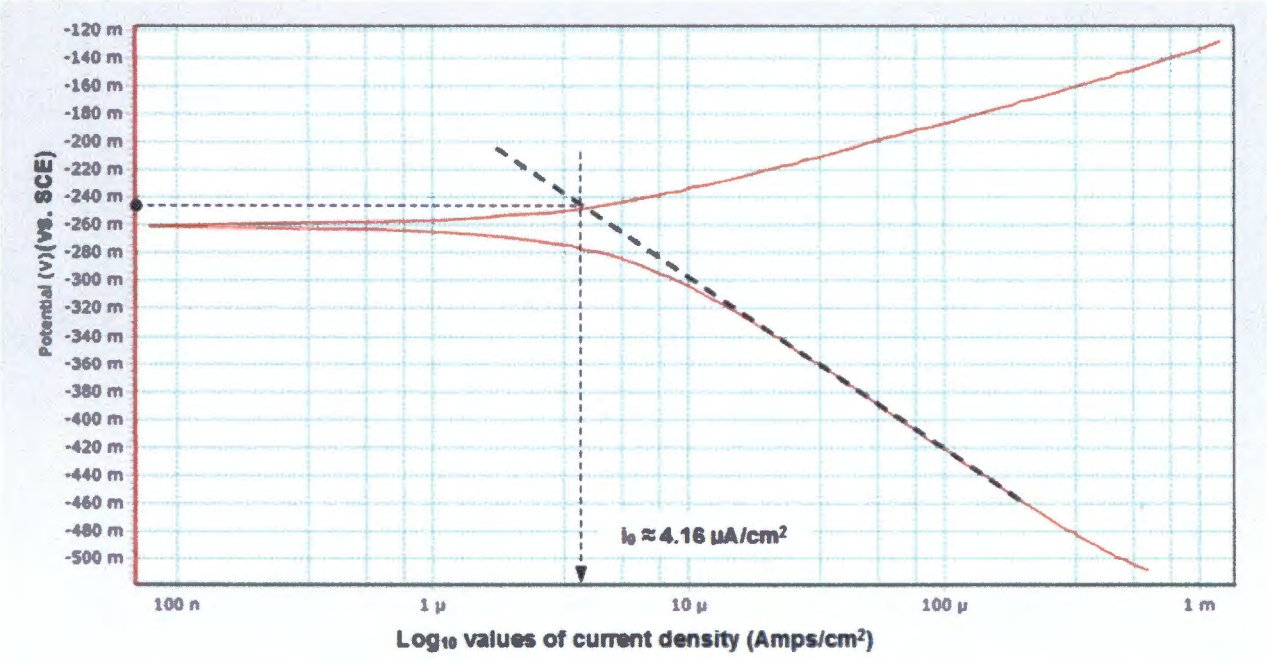

Figure 4.1: Tafel plot analysis of potential (V_{SCE}) vs. log current density (A/cm^2) for Ni.

In figures 4.2 and 4.3 micrographs of the Ni surface, pre and post testing of approximately the same regions, are shown. These images illustrate the somewhat coarse nature of the Ni surface. This can be used for a comparative analysis with the (6) NiPt micrographs seen in figures 4.8 and 4.9 showing consistency in the surface finish of the two sample types. This further illustrates the point that surface roughness on this scale had no marked impact on the Tafel analysis as discussed in table 4.6 below.

Figure 4.2: Micrograph of the Ni surface to be tested (pre-testing).

Figure 4.3: Micrograph of the Ni tested surface (post-testing).

4.1.2 Vanadium

Figure 4.4 shows a Tafel plot of a V sample analysed. The resulting log i_0 calculated for the hydrogen reduction reaction of the sample is approximately -6.5 (according to the method outlined in section 3.3.1.b). This value of -6.5 is consistent with that found in the literature, under the same test conditions, of i_0 = -6.3[57-60]. This indicates that the Tafel analysis ran without fault and that the V behaved as expected.

In figures 4.5 and 4.6 micrographs of the V surface, pre and post testing of approximately the same regions, are shown. Although these surfaces contain micro scratches, the scale of surface roughness had no impact on the Tafel analysis. This is evident in the i_0 value calculated for V as well as the results discussed in table 4.6.

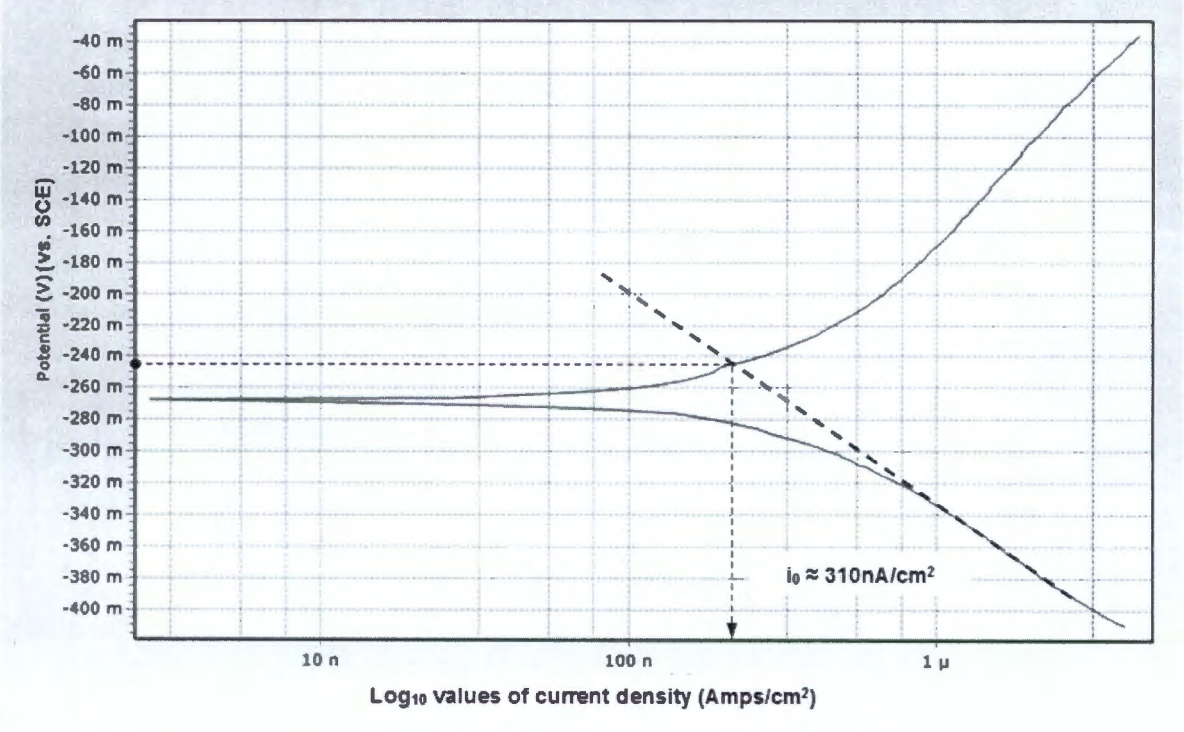

Figure 4.4: Tafel plot analysis of potential (V_{SCE}) vs. log current density (A/cm^2) for V.

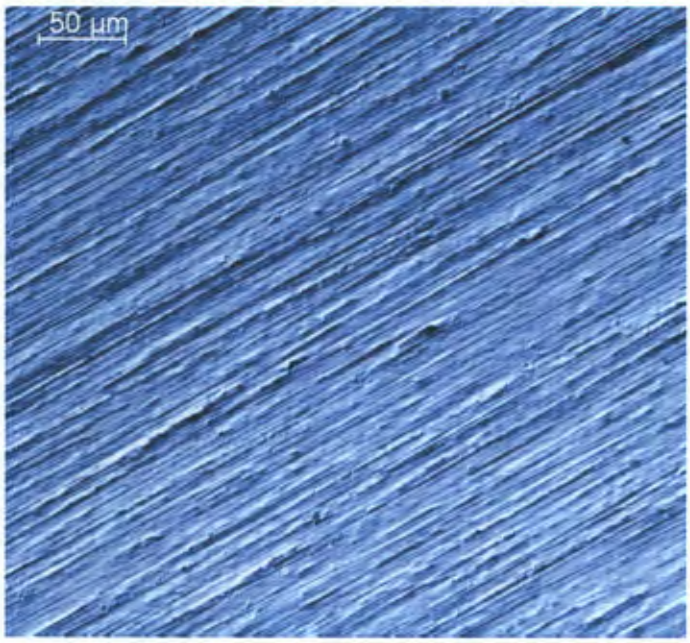

Figure 4.5: Micrograph of the V surface to be tested (pre-testing).

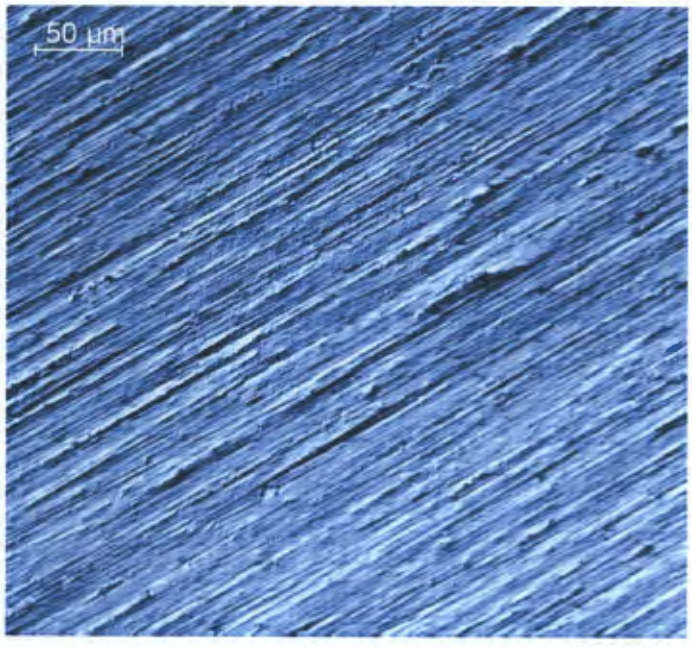

Figure 4.6: Micrograph of the V tested surface (post-testing).

4.1.3 (6) NiPt (as pure Pt)

As mentioned in section 3.2, the Ni/Pt sample was initially intended as a NSA sample but it was later found that the thickness of the Pt coating masked any NSA attributes. Thus, along with the stability of the single Pt coat, pure Pt was analysed with the Ni substrate serving merely as a platform for the Pt coating. Owing to the Pt being evaporated onto the Ni surface, the Pt was of highest purity.

Figure 4.7 shows a Tafel plot of a NiPt sample analysed. The resulting log i_0 calculated for the hydrogen reduction reaction of the sample is approximately -3.5 (according to the method outlined in section 3.3.1.b). This value of -3.5 is consistent with that found in the literature, under the same test conditions, of i_0 = -3.2[57-60]. This indicates that the Tafel analysis ran without fault and that although a Ni substrate is present, the sample behaved as pure Pt with the underlying Ni serving as a platform for the Pt coating.

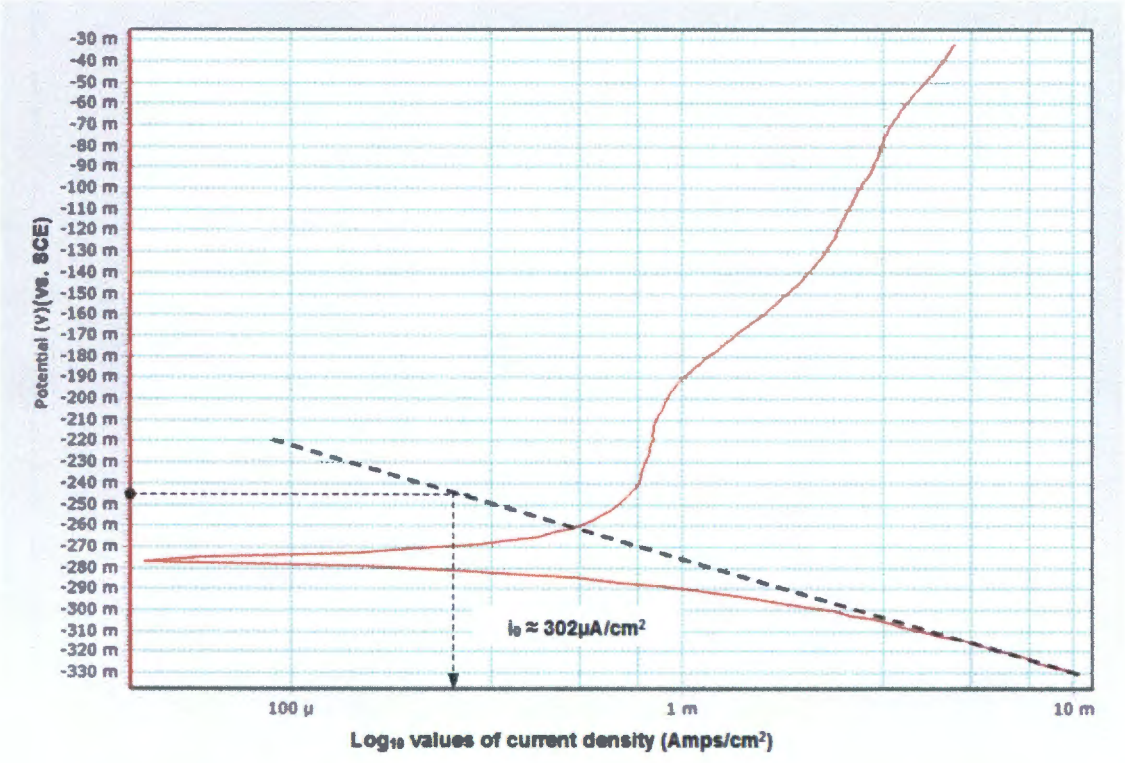

Figure 4.7: Tafel plot analysis of potential (V_{SCE}) vs. log current density (A/cm^2) for NiPt as pure Pt.

In figures 4.8 and 4.9 micrographs of the NiPt surface, pre and post testing of approximately the same regions are shown. Comparing the two images we see no peeling of the sample surface post testing. The deposited Pt layer has remained intact, confirming that only pure Pt was being tested which correlates to the i_0 value calculated for this sample. In figure 4.10 a RBS spectrum of this NiPt system is shown, validating the presence of the Ni substrate and, more importantly, the Pt surface coating.

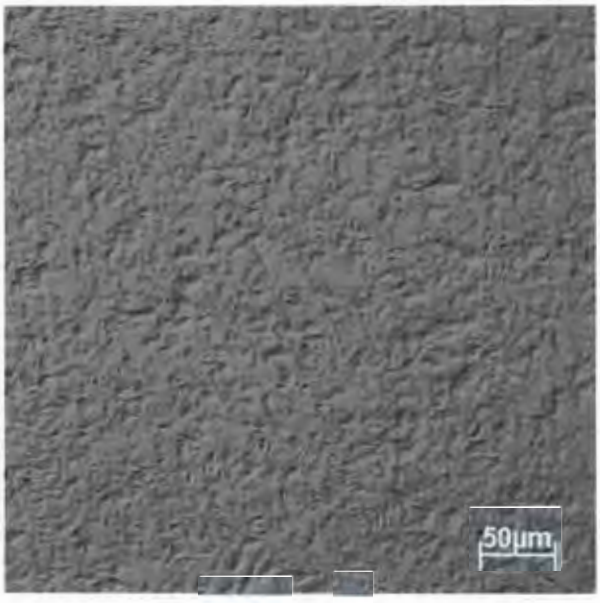

Figure 4.8: Micrograph of the NiPt surface to be tested (pre-testing).

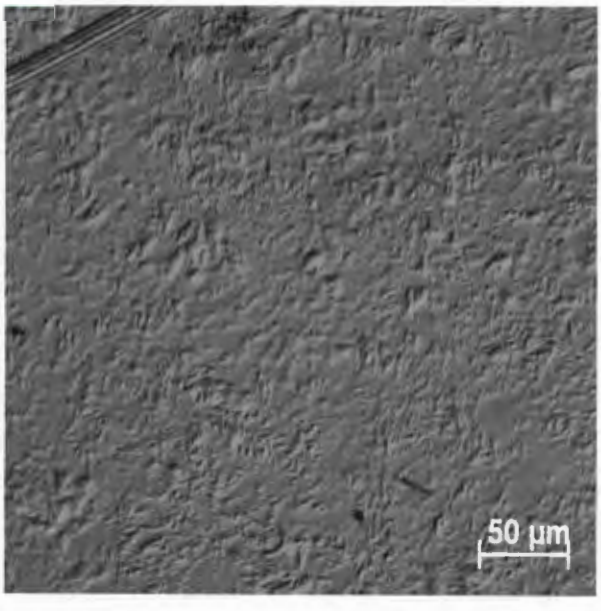

Figure 4.9: Micrograph of the NiPt tested surface (post-testing).

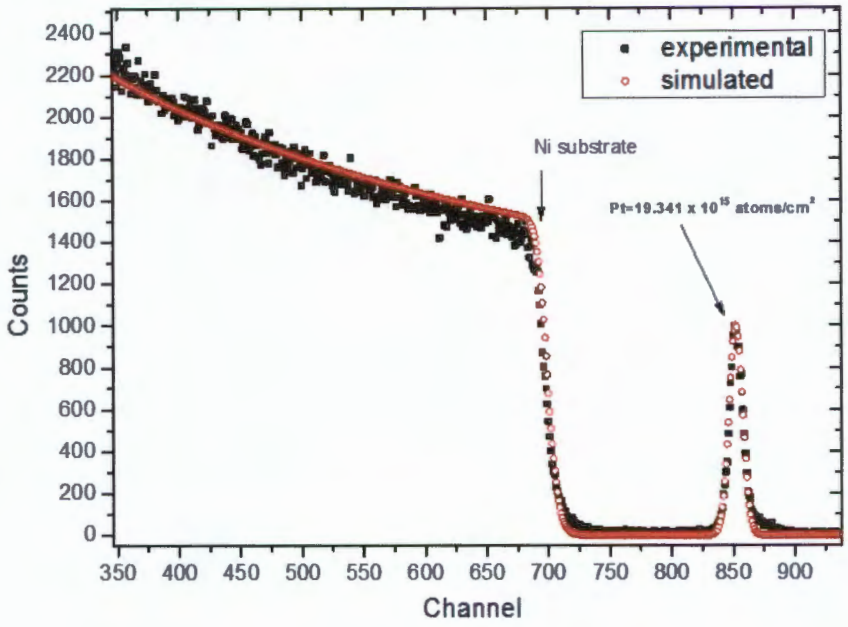

Figure 4.10: RBS spectrum for the NiPt system (Pt layer over Ni substrate) showing the value of the Pt layer thickness as obtained by simulation with the software program SIMNRA.

4.1.4 Platinum (57g button)

Figure 4.11 shows a Tafel plot of a Pt sample analysed from the 57g batch. It is evident before any further analysis that this Pt is not showing the results as expected from the literature. Analysis of the Tafel plot shows that the OCP is highly positive at a value of ~470 mV_{SCE} (715 mV_{SHE}). This value is substantially greater than the equilibrium potential for the H^+/H_2 reaction (0 V_{SHE} at pH = 0) with the measured currents not reflecting hydrogen reduction (evolution).

The most likely cause of the highly positive rest potentials observed here is trace oxygen present in the 99.99% nitrogen gas feed. Reduction of this residual dissolved oxygen in the electrolyte would cause a substantial cathodic reaction rate. This effect would be further compounded by the continuous stirring of the electrolyte by nitrogen gas bubbling. As such, these measurements of the Pt (57g) do not reflect the hydrogen reaction kinetics and thus cannot be used to determine the hydrogen evolution kinetics.

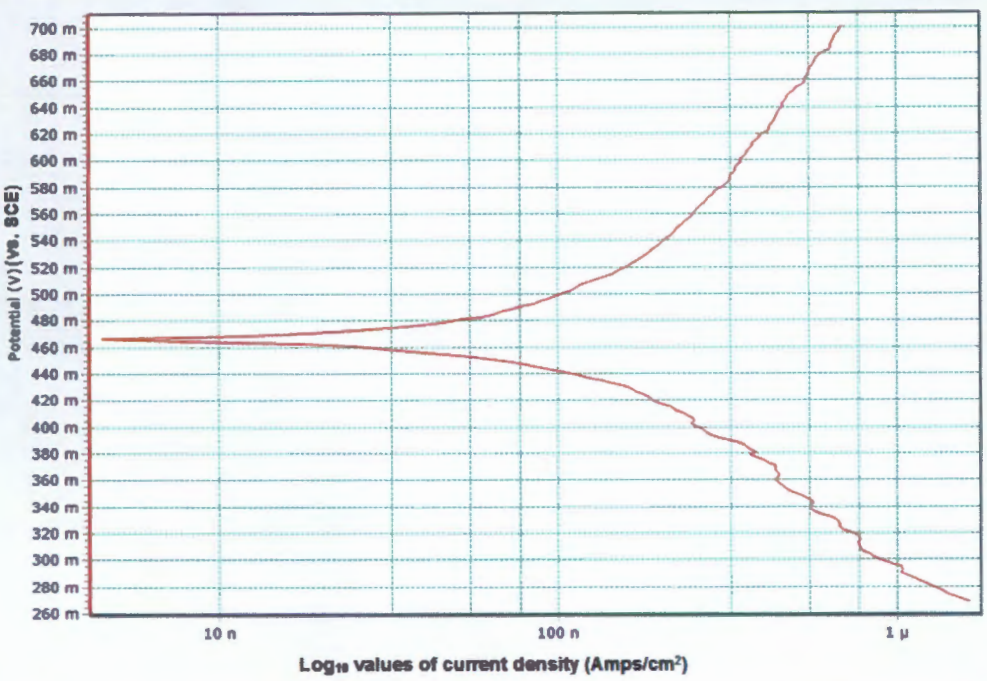

Figure 4.11: Tafel plot analysis of potential (V_{SCE}) vs. log current density (A/cm^2) for Pt (57g batch).

Elemental analysis by SEM-EDS was used to identify any impurities present in the Pt. These results can be seen in figure 4.12 and figures 8.6 to 8.9. It is evident from these graphs that only Pt was registered as being present with no other impurities.

It must be noted that with all the other samples elemental analysis was carried out with PIXE, which is a far more sensitive technique relative to SEM-EDS which only registers impurities down to 1% concentration. PIXE was not available for the Pt samples in this section. However, impurities (chromium, manganese and iron) were detected by PIXE in the NSA samples (tables 4.1 – 4.5) and it is almost certain these impurities were only present in the Pt substrate, the same Pt from this 57g batch (Pt, Ni and V evaporation targets were not processed in the lab as was done with the Pt substrates), which implies presence of those impurities throughout all of the Pt substrates prepared in the laboratory. The source of these impurities may be inherent in the Pt as received from *Perkins Metals* or may have been introduced into the ductile Pt surface from the stainless steel *Dinkel Laboratory roller*. These impurities, however, are not responsible for the highly positive rest potentials seen here. Without the presence of reducible species in the electrolyte, the impurities cannot cause the measured current density to be cathodic at potentials more positive than the H^+/H_2 equilibrium potential. As previously discussed, the only probable source of the observed potentials is reduction of trace oxygen from the nitrogen feed.

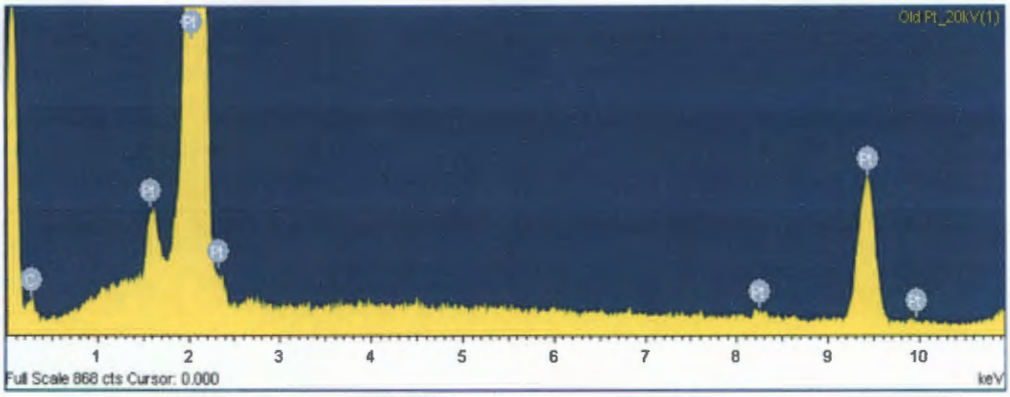

Figure 4.12: EDS Spectrum of the 57g Pt sample (point 1).

In figure 4.13 a micrograph of a Pt sample (pre testing) from this same 57g batch of Pt is shown. As indicated by the arrows, one can clearly see particulates in the Pt surface. These particulates may have been introduced into the platinum's ductile surface during the rolling of the platinum or through the polishing process from the fine, particles present in the polishing solutions. Polishing is the final step in preparing the Pt substrates and so any particulates embedded in the surface could not be removed as this would compromise the integrity of the surface finish. These particulates would not have any effect on the electrochemical results seen for, as described above, the lack of reducible species in the electrolyte negates this as a possibility. Scratches are also present in the micrograph but, as will be discussed in table 4.6, these have no bearing on the results obtained.

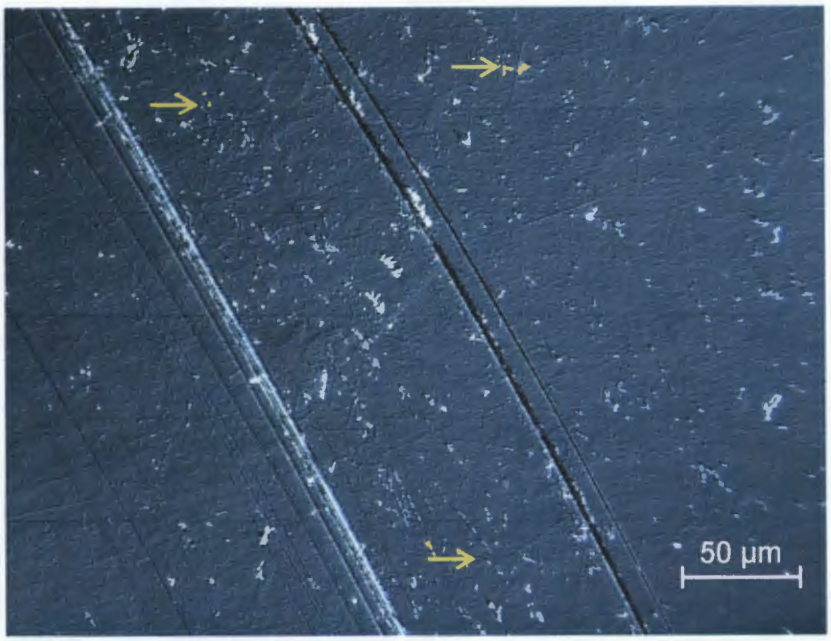

Figure 4.13: Micrograph of Pt showing particulates indicated by arrows (pre testing).

4.1.5 Platinum Annealed (57g button)

Two approaches were used to determine the possible cause of the erroneous electrochemical data measured for the Pt 57g button. The first will be discussed in this section and deals with increased dislocation concentration due to cold working; the second is discussed in section 4.1.6.

Another possibility for the observed electrochemical values may have arisen from the large amount of cold working done on the Pt in the rolling process (section 3.2). This cold working gives rise to the formation of dislocations in the Pt which in turn is the cause of many high energy regions on the Pt surface stemming from the dislocations. These high energy regions may affect the Tafel analysis and thus the exchange current density values.

In order to rule out dislocations as a problematic source, some Pt samples from the 57g batch were heat treated at 1000°C for 8 hours to allow for recrystallization and thus elimination of the dislocations.

The same highly positive rest potentials were observed on electrochemical analysis of the heat treated Pt samples. This shows that dislocations had no impact and further highlights oxygen contamination as the source of the positive rest potentials.

Micrographs of the heat treated Pt were also analysed and showed surface particulates. These results are not shown as they had no bearing on the electrochemistry of the Pt as described previously.

4.1.6 Platinum (1g button)

The second approach to try determine the cause of the results seen in 4.1.4 and 4.1.5 above was to use a new sample of Pt, also received from *Perkins Metals* but of a separate batch from that of the 57g batch, and to run the same tests on this Pt. A secondary variable for the results seen in 4.1.4 and 4.1.5 was ruled out in that this 1g Pt sample was already in button form (as received) and so melting in the induction furnace was not required. Thus, the crucible used to melt the previous Pt samples (57g batch) in the induction furnace was also ruled out as a source of impurities.

Elemental analysis by SEM-EDS was used to identify any impurities present in the Pt. These results can be seen in figure 4.14 and figures A.8 to A.10. It is evident from these graphs that only Pt was registered as being present with no other impurities. The same highly positive rest potentials were observed on electrochemical analysis of the 1g Pt samples. This again emphasises oxygen contamination as the source of the positive rest potentials. Micrographs of the 1g Pt samples were also analysed and showed surface particulates. These results are not shown as they had no bearing on the electrochemistry of the Pt as described previously.

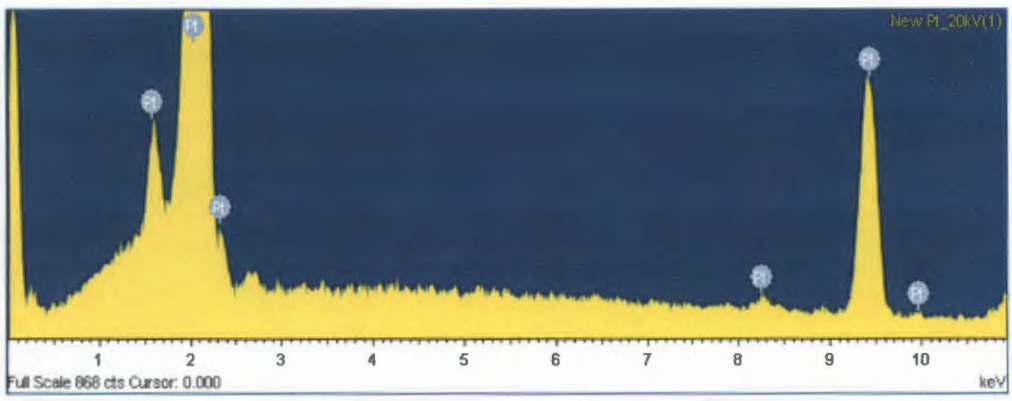

Figure 4.14: EDS Spectrum of the 1g Pt sample (point 1).

4.2 Near-Surface Alloys (NSAs)

Analyses of the various NSA samples fabricated are now presented. First the PtNi system will be considered followed by the PtV system.

For the PtNi system, three different subtypes of NSAs were fabricated as can be seen in table 3.2, whereas only two subtypes of PtV were fabricated and tested due to, firstly, lack of V metal substrates to fabricate the VPt NSA and, secondly, oxidation problems with regards to a heat treated PtV NSA.

With regards to both PtNi and PtV, 5nm coatings followed by 3nm coatings of surface Pt were fabricated and tested to determine whether the 5nm Pt surface layer was too thick and masked the geometric and ligand effects of the subsurface transition metal (Ni and V). It must also be noted that 3nm was the thinnest possible coating available in this project, fabricated by e-beam deposition.

4.2.1 (1, 2) PtNi (5nm and 3nm)

Electrochemical analysis of the PtNi samples yielded no useful results with both species of NSAs showing highly positive rest potentials of approximately +400 to +500mV$_{SCE}$. These values are substantially greater than the equilibrium potential for the H^+/H_2 reaction (0 V_{SHE} at pH = 0) with the measured currents not reflecting hydrogen reduction (evolution). The most likely cause of the highly positive rest potentials observed here is trace oxygen present in the 99.99% nitrogen gas feed. Reduction of this residual dissolved oxygen in the electrolyte would be able to cause a substantial cathodic reaction rate. This effect would be further compounded by the continuous stirring of the electrolyte by nitrogen gas bubbling. As such, these measurements do not reflect the hydrogen reaction kinetics and thus cannot be used to determine the hydrogen evolution kinetics. This is the same trend as discussed in sections 4.1.4 – 4.1.6.

In figures 4.15 and 4.16 micrographs of the PtNi 5nm surface pre and post Tafel analysis, respectively, are shown. While in figures 4.17 and 4.18 similarly featured micrographs of PtNi 3nm pre and post Tafel analysis, respectively, are shown. Both sets of micrographs (4.15 – 4.18) illustrate an intact coated surface prior to testing followed by a complete breakdown in the coatings during Tafel analysis. It is unclear on the cause of the peeling. Temperature variation between substrate and deposited metal should not cause this (3.2) but rather abrupt interfaces may be responsible (2.4.1). Peeling of the coatings along with reduction of residual dissolved oxygen in the electrolyte prevented any meaningful analysis of the electrochemical results obtained for the PtNi NSAs.

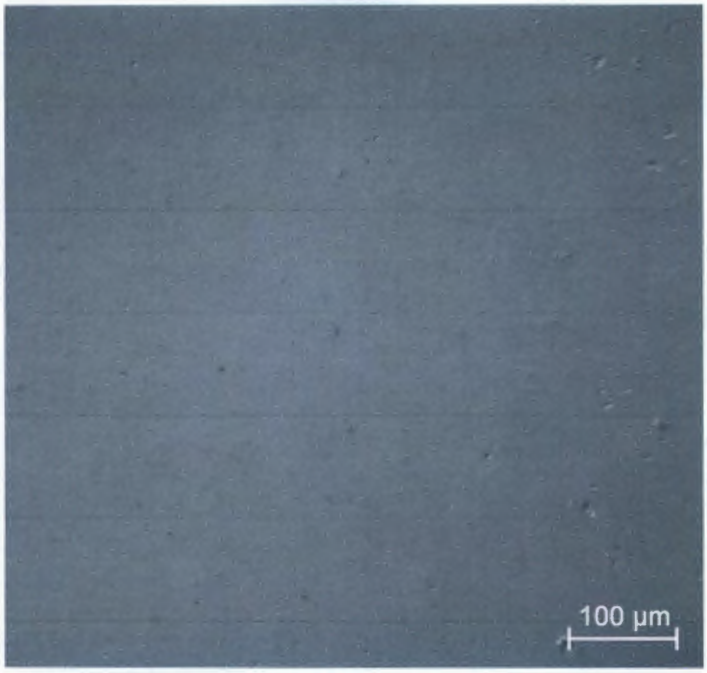

Figure 4.15: Micrograph of PtNi 5nm surface pre-Tafel analysis

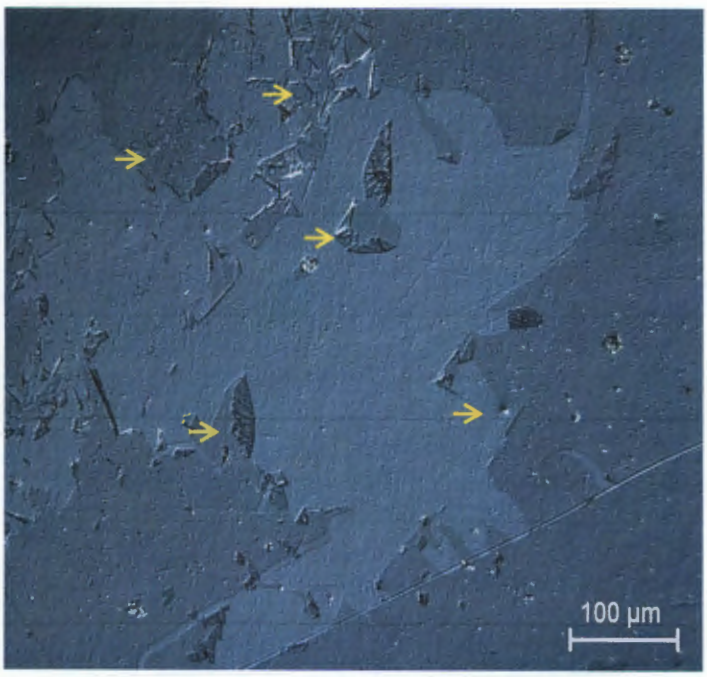

Figure 4.16: Micrograph of PtNi 5nm surface post-Tafel analysis showing peeling at arrows.

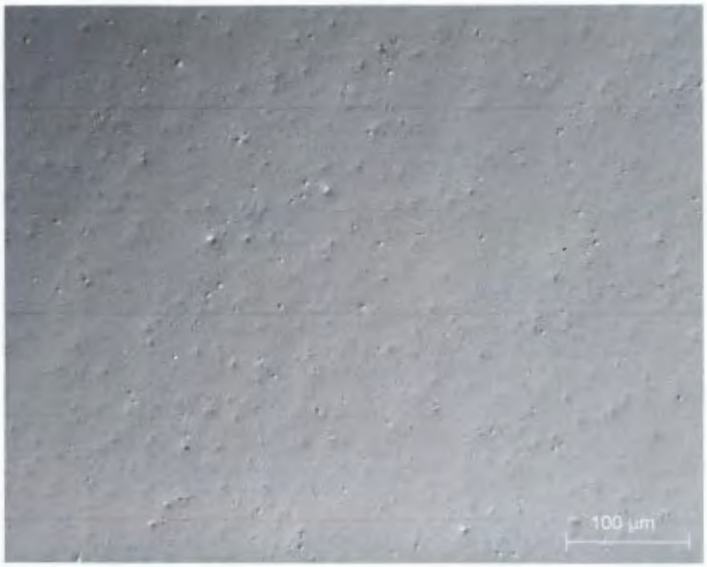

Figure 4.17: Micrograph of PtNi 3nm surface pre-Tafel analysis.

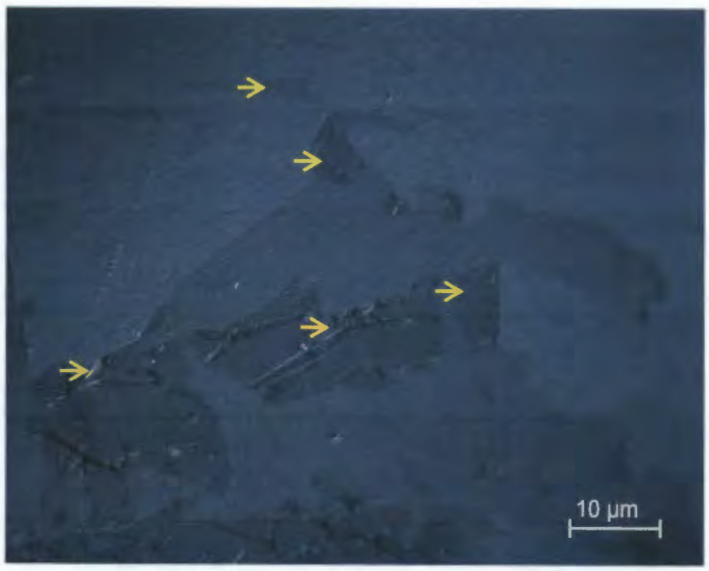

Figure 4.18: Micrograph of PtNi 3nm surface post-Tafel analysis showing peeling at arrows.

In tables 4.1 and 4.2 we see the elemental composition obtained from PIXE analysis for PtNi 5nm and PtNi 3nm samples respectively. Values are quoted in parts per million (ppm). The presence of these elements indicates possible presence of stainless steel. Possible sources of the impurities may be the stainless steel roller used to roll the substrate metals pressing impurities into the highly ductile, softer Pt surface (sections 3.2 and 4.1.4).

Table 4.1: Table showing trace elements and NSA constituents present in PtNi 5nm sample from PIXE analysis.

	Cr	Mn	Fe	Ni	Pt
Concentration (ppm)	1245	192	1042	847	993932
Error	200	88	78	55	12894

Table 4.2: Table showing trace elements and NSA constituents present in PtNi 3nm sample via PIXE analysis.

	Cr	Mn	Fe	Ni	Pt
Concentration (ppm)	1557	298	1070	750	992321
Error	280	173	98	64	10631

These impurities, however, are not responsible for the highly positive rest potentials seen here. Without the presence of reducible species in the electrolyte, the impurities cannot cause the measured current density to be cathodic at potentials more positive than the H^+/H_2 equilibrium potential. As previously discussed, the only probable source of the observed potentials is reduction of trace oxygen from the nitrogen feed.

4.2.2 (5) PtNi Heat Treated

Here we see samples comprising a Pt substrate with a 3nm Ni surface coating. Samples were heat treated to allow for diffusion of the Ni into the subsurface region of the Pt thus forming an NSA structure as described in section 3.2.

Electrochemical analysis of the annealed PtNi samples yielded no useful results with samples showing highly positive rest potentials of approximately +320 to +750mV_{SCE}. These values are substantially greater than the equilibrium potential for the H^+/H_2 reaction (0 V_{SHE} at pH = 0) with the measured currents not reflecting hydrogen reduction (evolution). The broad potential range most likely resulted from varying degrees of Ni segregation into the Pt subsurface while the high positive rest potentials owing to trace oxygen present in the 99.99% nitrogen gas feed.

Reduction of this residual dissolved oxygen in the electrolyte would be able to cause a substantial cathodic reaction rate. This effect would be further compounded by the continuous stirring of the electrolyte by nitrogen gas bubbling. As such, these measurements do not reflect the hydrogen reaction kinetics and thus cannot be used to determine the hydrogen evolution kinetics. This is the same trend as discussed in sections 4.1.4 – 4.1.6.

There were no abnormalities or interesting features seen in microscope analysis of the annealed PtNi samples and so no micrographs were included.

In table 4.3 we see the elemental composition obtained from PIXE analysis for the PtNi heat treated samples. Values are quoted in parts per million (ppm). The presence of these elements indicates possible presence of stainless steel. Possible sources of the impurities may be the stainless steel roller used to roll the substrate metals pressing impurities into the highly ductile, softer Pt surface (sections 3.2 and 4.1.4).

Table 4.3: Table showing trace elements and NSA constituents present in PtNi heat treated samples via PIXE analysis.

	Cr	Mn	Fe	Ni	Pt
Concentration (ppm)	350	69	452	442	991785
Error	29	16	14	107	46530

These impurities, however, are not responsible for the highly positive rest potentials seen here. Without the presence of reducible species in the electrolyte, the impurities cannot cause the measured current density to be cathodic at potentials more positive than the H^+/H_2 equilibrium potential. As previously discussed, the only probable source of the observed potentials is reduction of trace oxygen from the nitrogen feed.

4.2.3 (3, 4) PtV (5nm and 3nm)

Electrochemical analysis of the PtV samples yielded no useful results with both species of NSAs showing highly positive rest potentials of approximately +420 to +550mV_{SCE}. These values are substantially greater than the equilibrium potential for the H^+/H_2 reaction (0 V_{SHE} at pH = 0) with the measured currents not reflecting hydrogen reduction (evolution). The most likely cause of the highly positive rest potentials observed here is trace oxygen present in the 99.99% nitrogen gas feed. Reduction of this residual dissolved oxygen in the electrolyte would be able to cause a substantial cathodic reaction rate.

This effect would be further compounded by the continuous stirring of the electrolyte by nitrogen gas bubbling. As such, these measurements do not reflect the hydrogen reaction kinetics and thus cannot be used to determine the hydrogen evolution kinetics. This is the same trend as discussed in sections 4.1.4 – 4.1.6.

In figures 4.19 and 4.20 micrographs of the PtV 5nm surface pre and post Tafel analysis, respectively, are shown. While in figures 4.21 and 4.22 similarly featured micrographs of PtV 3nm pre and post Tafel analysis, respectively, are shown. Both sets of micrographs (4.19 – 4.22) illustrate an intact coated surface prior to testing followed by a complete breakdown in the coatings during Tafel analysis. It is unclear on the cause of the peeling. Temperature variation between substrate and deposited metal should not cause this (3.2) but rather abrupt interfaces may be responsible (2.4.1). Peeling of the coatings along with reduction of residual dissolved oxygen in the electrolyte prevented any meaningful analysis of the electrochemical results obtained for the PtV NSAs.

In tables 4.4 and 4.5 we see the elemental composition obtained from PIXE analysis for PtV 5nm and PtV 3nm samples respectively. Values are quoted in parts per million (ppm). The presence of these elements indicates possible presence of stainless steel. Possible sources of the impurities may be the stainless steel roller used to roll the substrate metals pressing impurities into the highly ductile, softer Pt surface (sections 3.2 and 4.1.4).

These impurities, however, are not responsible for the highly positive rest potentials seen here. Without the presence of reducible species in the electrolyte, the impurities cannot cause the measured current density to be cathodic at potentials more positive than the H^+/H_2 equilibrium potential. As previously discussed, the only probable source of the observed potentials is reduction of trace oxygen from the nitrogen feed.

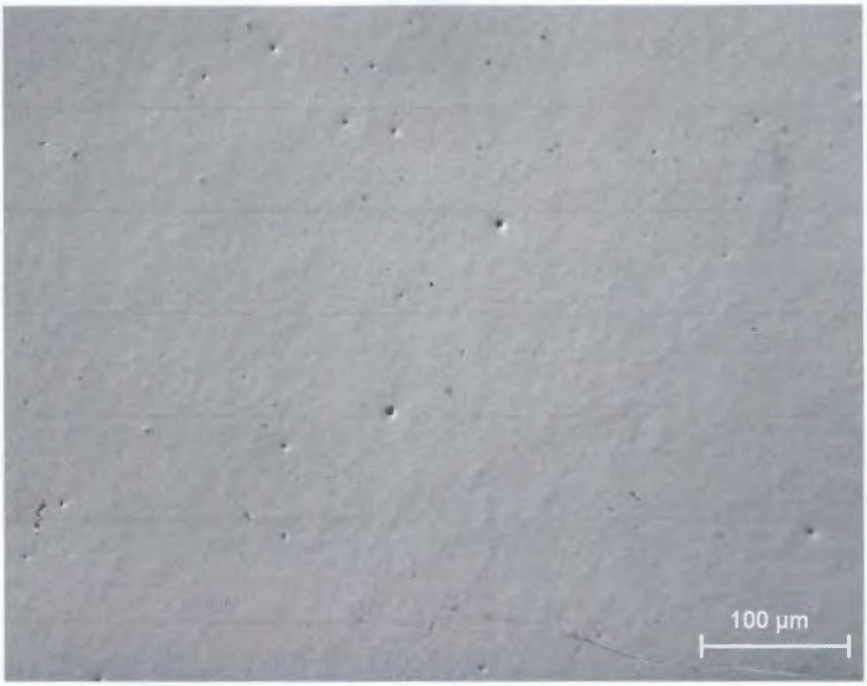

Figure 4.19: Micrograph of PtV 5nm surface pre-Tafel analysis

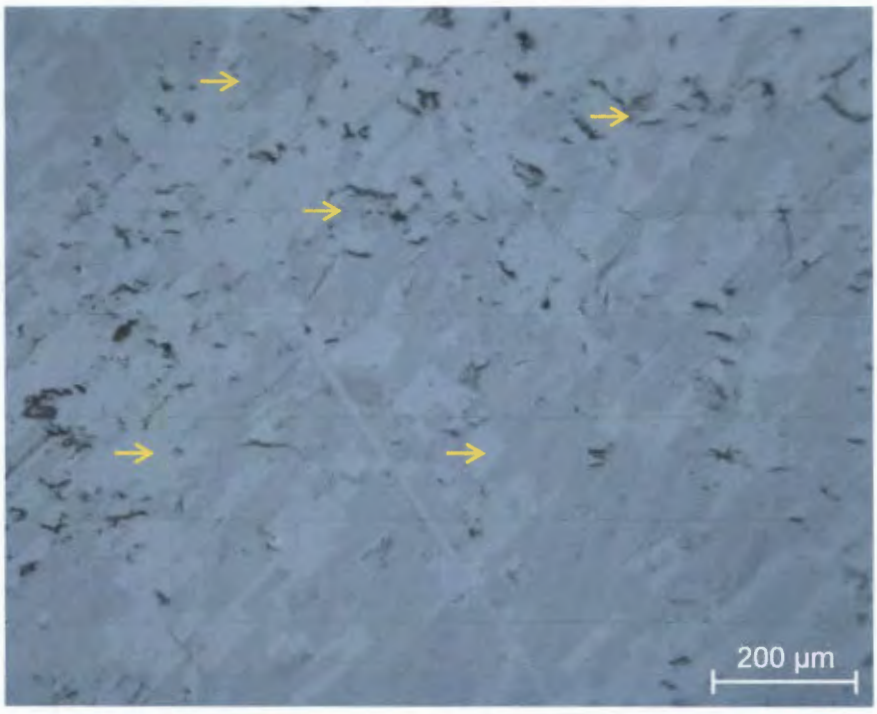

Figure 4.20: Micrograph of PtV 5nm surface post-Tafel analysis showing peeling as indicated

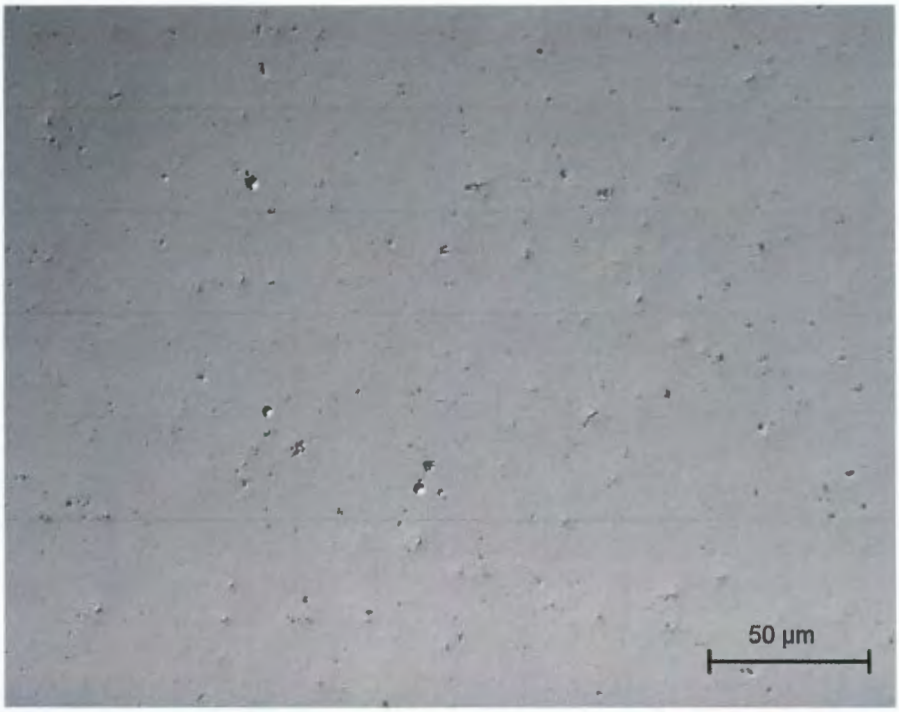

Figure 4.21: Micrograph of PtV 3nm surface pre-Tafel analysis.

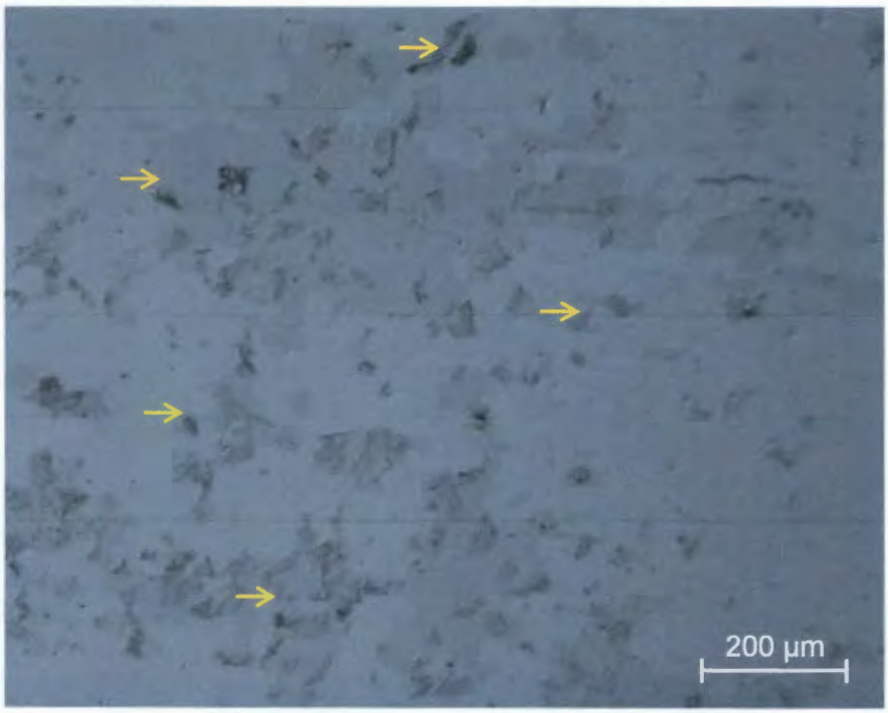

Figure 4.22: Micrograph of PtV 3nm surface post-Tafel analysis showing peeling as indicated.

Table 4.4: Table showing trace elements and NSA constituents present in PtV 5nm sample from PIXE analysis.

	V	Cr	Fe	Pt
Concentration (ppm)	2115	1853	1337	987000
Error	862	290	105	10289

Table 4.5: Table showing trace elements and NSA constituents present in PtV 3nm sample from PIXE analysis.

	V	Cr	Fe	Pt
Concentration (ppm)	1985	1205	1150	988196
Error	840	386	69	14045

In table 4.6 we see comparison of averaged Ra-values for all samples tested in this project. We see that surface roughness is essentially consistent throughout all samples tested. This indicates that the scale of the Ra-values and surface roughness at this magnitude, seen for all samples, had no effect on the Tafel analyses and calculated i_0 values. This holds true due to the i_0 values calculated for the Ni, V and NiPt samples all being almost identical to the literature i_0 values whilst all having the same range of Ra-values as the other tested samples.

As is evident from the results discussed here, catalytic properties of the fabricated PtNi and PtV near-surface alloys could not be successfully determined. Trace oxygen contamination was responsible for the highly positive rest potentials observed, while poor adhesion of the deposited nano-coatings further impeded analysis of the NSA catalytic properties.

Table 4.6: Average Ra-values for all samples tested.

Sample Type		Ra-average (μm)	Ra-average (nm)
Ni		0.11	110
V		0.13	130
NiPt		0.15	150
Pt (57g)		0.29	290
Pt (57g annealed)		0.11	110
Pt (1g)		0.15	150
PtNi (5nm)		0.12	120
PtNi (3nm)		0.16	160
PtNi (heat treated)		0.22	220
PtV (5nm)		0.16	160
PtV (3nm)		0.15	150

CHAPTER 5

CONCLUSION

From the experimental procedures that were performed and the analysis of the results obtained, the following conclusions are drawn:

5.1 Surface Analysis

E-beam deposition was an ineffective technique in creating NSA samples analogous to the computationally modelled NSAs, with the minimum possible coating thickness (5nm and 3nm) still being thicker than the computed NSAs. As discussed in section 2.4.4.2 (a and b), electronic effects in the form of strain and ligand effects are directly responsible for the unique properties seen in NSAs[72]. To observe these effects the subsurface solute metal should be within a set depth below the host metal surface. An optimal solute depth of 3 monolayers below the host surface has been calculated, beyond this depth, electronic effects become minor but not obsolete[39,40,45]. Solutes deeper than 3 monolayers would not have as great an influence on the metal surface and thus not allow for pseudomorphic growth straining the host metal surface. The ligand effect is also minimal below 3 monolayers with subsurface solute atoms not being in an optimal range to bond with the surface atoms and thus not being able to alter the surface electronic properties[39,40,45].

As it stands, theoretically, 3nm and 5nm coatings are possibly too thick and mask the improved NSA catalytic properties. Experimentally, the 3nm coating thicknesses were not disproved due to breakdown of the NSA samples on testing. The 5nm coating was too thick as is seen with the NiPt sample. Here a stable, 5nm Pt coating on Ni displayed exchange current densities of just pure Pt metal showing that electronic effects were masked by the 5nm Ni depth. Alternative NSA fabrication techniques would need to be explored for future work.

Single coatings were seen to be stable for the NiPt sample, whereas two or more coating layers in the NSA samples (PtNi and PtV) were observed to be unstable and prone to peeling off the substrate.

Peeling of the NSA samples may be a result of abrupt interfaces forming as described in section 2.4.1[66]. This peeling of the coatings negatively affected the Tafel analyses, preventing proper analysis of the NSA structure.

Surface roughness on the scale of nanometers was not sufficient to have any negative impact on Tafel analysis.

NSA fabrication via heat treatment also proved unsuccessful as not enough information was available with regard to diffusion kinetics between parent and solute metal. It was not possible to ascertain the depth of Ni diffusion into the Pt substrate with the analytical instruments available to this project.

5.2 Elemental Analysis

Although no impurities were detected in the Pt substrates with SEM-EDS analysis, contamination was found in all the coated NSA samples through the more sensitive PIXE-EDS analysis. Contamination from the evaporated coating metals is not expected; but the presence of impurities in the Pt substrates at low concentrations remains a possibility. Such contaminations may be present in the form of small particulates embedding into the Pt surface during rolling and/or the grinding/polishing stages of preparation. These impurities, however, would have no bearing on the catalytic analyses carried out in this project as without the presence of reducible species in the electrolyte, these impurities cannot cause the measured current density to be cathodic at potentials more positive than the H+/H2 equilibrium potential

5.3 Electrochemical Analysis

Tafel plot analysis was a successful technique in calculating the i_0 values for the pure metals (Ni, V and NiPt as pure Pt). This is evident in the almost identical i_0 values for Ni, V and Pt (albeit in the NiPt form) with reference to the literature values.

Electrochemical analysis of the Pt substrates and NSA samples showed highly positive rest potentials. These positive rest potentials are substantially greater than the equilibrium potential for the H+/H2 reaction (0 VSHE at pH = 0) with the measured currents not reflecting hydrogen reduction (evolution). The most likely cause of the highly positive rest potentials observed here is trace oxygen present in the 99.99% nitrogen gas feed.

Reduction of this residual dissolved oxygen in the electrolyte would cause a substantial cathodic reaction rate. This effect would be further compounded by the continuous stirring of the electrolyte by nitrogen gas bubbling.

It must be noted that different tanks of nitrogen gas were used for the Pt substrates and NSA samples compared to that used for the Ni, V and NiPt samples. It is known that variations in impurity concentrations (such as oxygen) occur between different tanks of gases like the different nitrogen tanks used in this project[88]. This may account for the trace oxygen reduction seen in the NSA samples and Pt substrates but not in the Ni, V and NiPt samples.

Ultimately oxygen contamination and peeling of the NSA films led to lack of viable results characterising NSA catalytic properties. If peeling had not occurred, coating thickness may have also been proved or disproved as a factor. It is evident, as discussed, that 5nm coatings are too thick (as seen with NiPt).

This project has shown that Tafel Plot analysis is an effective technique in analysing the catalytic properties of metal samples as is seen with NiPt, Ni and V. It has given valuable insight on how to improve on future experiments with regards to the oxygen contamination. Finally, it has shown that e-beam deposition is not the most effective technique in forming NSAs but rather other techniques should be employed such as atomic layer deposition. This would allow for a stable NSA with the solute metal to exist in the near surface region of one to three monolayers below the host surface thus giving a definitive insight into the catalytic properties of near-surface alloys.

CHAPTER 6

FUTURE WORK

The following recommendations are made to further research done in this study:

- One could employ alternative deposition methods such as Atomic Layer Deposition (ALD). Such methods would allow for the deposition of individual monolayers (coatings comprising of a single layer of atoms) better mimicking the NSA structure.

- Use of alternative electrochemical methods for measuring exchange current density values of fabricated samples, such as electrochemical impedance spectroscopy (EIS).

- Alternative deaeration techniques should be employed to prevent trace oxygen contamination. An example would be vacuum filtration.

- Ultimately, testing the fabricated NSAs in a working PEMFC in an attempt to identify if indeed the fabricated NSAs are more effective than power generation relative to current PEMFC catalysts.

CHAPTER 7

REFERENCES

1. Britannica, E. platinum (Pt). *In Encyclopædia Britannica* (2012).at <http://www.britannica.com/EBchecked/topic/464081/platinum-Pt>

2. Kitchin, J. R., Nørskov, J. K., Barteau, M. a & Chen, J. G. Modification of the surface electronic and chemical properties of Pt(111) by subsurface 3d transition metals. *The Journal of chemical physics* **120**, 10240–6 (2004).

3. Carrette, L., Friedrich, K. a. & Stimming, U. Fuel Cells - Fundamentals and Applications. *Fuel Cells* **1**, 5–39 (2001).

4. Carrette, L. & Friedrich, K. A. Fuel Cells : Principles , Types , Fuels , and Applications **. *Chem. Phys. Chem* **1**, 163–173 (2000).

5. Zoski, C. G. *Handbook of Electrochemistry*. 7 (Elsevier: New Mexico, 2007).

6. Hagen, J. *Industrial Catalysis: A Practical Approach*. 295–313 (Wiley-VCH Verlag GmbH & Co. KGaA: Weinheim, Germany, 2006).

7. Gasteiger, H. A. and Garche, J. *Fuel Cell: Handbook of Heterogeneous Catalysis*. 3081–3121 (Wiley-VCH Verlag GmbH & Co. KGaA: Weinheim, Germany, 2008).doi:10.1002/9783527610044

8. Shah, R. K. & Range, T. *INTRODUCTION TO FUEL CELLS*. 1–6 (Noida, India, 2003).

9. Electrochemistry Dictionary and Encyclopedia. 1 (2012).at <http://electrochem.cwru.edu/ed/dict.htm#a08>

10. Zhang, J. *PEM Fuel Cell Electrocatalysts and Catalyst Layers Fundamentals and Applications*. 971–973 (Springer-Verlag: London, 2008).

11. Ramani, V. Fuel Cells. *The Electrochemical Society Interface* 41–44 (2006).

12. Monk, P. *FUNDAMENTALS OF ELECTROANALYTICAL CHEMISTRY*. 132–134 (JOHN WILEY & SONS LTD: Manchester, UK, 2001).

13. Lazarou, S., Pyrgioti, E. & Alexandridis, A. T. A simple electric circuit model for proton exchange membrane fuel cells. *Journal of Power Sources* **190**, 380–386 (2009).

14. Wang, C., Member, S., Nehrir, M. H., Member, S. & Shaw, S. R. Dynamic Models and Model Validation for PEM Fuel Cells Using Electrical Circuits. *IEEE Transactions On Energy Conversion* **20**, 442–451 (2005).

15. National Energy Technology Laboratory Fuel Cell Hand Book (sixth edition). 2–9 (2002).

16. National Energy Technology Laboratory Fuel Cell Handbook (fifth edition). 1.1–1.35 (2000).

17. Paulus, U. A. Electrocatalysis for Polymer Electrolyte Fuel Cells : Metal Alloys and Model Systems. 5–36 (2002).

18. Kinoshita, K. Electrochemistry Encyclopedia -- Electrochemical uses of carbon. 1 (2001).at <http://electrochem.cwru.edu/encycl/art-c01-carbon.htm>

19. U. Stimming, W. W. and E. R. Elektrotechnik und Informationstechnik. 114, 564 (1997).

20. S. G. Chalk, J. F. M. and F. W. W. Journal of Power Source. 40, 86 (2000).

21. Hart, D. Journal of Power Sources. 23, 86 (2000).

22. Dufour, A. U. Journal of Power Sources. 19, 71 (1998).

23. L. Carrette, J. Collins, A. D. and U. S. Bunsen magazine of the German Bunsen Society for Physical chemistry. 27 (2000).

24. Cornils, B., Herrmann, W.A., Schlögl, R., Wong, C. H. Catalysis from A to Z. (2000).

25. Acres, G. J. K. et al. Electrocatalysts for fuel cells. 393–400 (1997).

26. Escaño, M. C., Gyenge, E., Nakanishi, H. & Kasai, H. Pt/Cr and Pt/Ni Catalysts for Oxygen Reduction Reaction: To Alloy or Not to Alloy? *Journal of Nanoscience and Nanotechnology* **11**, 2944–2951 (2011).

27. Thompson, E. L. Behavior of Proton Exchange Membrane Fuel Cells at Sub-Freezing Temperatures. 1–3 (2007).

28. Broka, K. & Ekdunge, P. Modelling the PEM fuel cell cathode. *Journal of Applied Electrochemistry* **27**, 281–289 (1997).

29. Mayrhofer, K. J. J. *et al.* Fuel cell catalyst degradation on the nanoscale. *Electrochemistry Communications* **10**, 1144–1147 (2008).

30. Mavrikakis, M. *Near-Surface Alloys for Improved Catalysis. Bulletin of the American Physical Society* 1–27 (Wisconsin, 2006).at <http://www.aps.org/meetings/multimedia/upload/Near_Surface_Alloys_for_Improved_Catalysis_Manos_Mavrikakis.pdf>

31. Hays, C. C., Kulleck, J., Haines, B. & Narayanan, S. R. *Thin Film Platinum Alloys for use as Catalyst Materials in Fuel Cells*. 619–623 (Pasadena, 2009).

32. Gottesfeld, S.; Zawodzinski, T. A. Advances in Electrochemical Science and Engineering. **5**, 197–297 (1997).

33. Markovic, N. M.; Ross, P. N. Electrochim. Acta. *Electrochim. Acta* **45**, 4101– 4115 (2000).

34. Tarasevich, M. R.; Sadkowski; Yeager, E. In Comprehensive Treatise of Electrochemistry. *Journal of Electroanalytical Chemistry and Interfacial Electrochemistry* **136**, 301–398 (1983).

35. Adzic, R. R. In Frontiers in Electrochemistry. 197–241 (1998).

36. Wang, J. X.; Markovic, N. M.; Adzic, R. R. J. Phys. Chem. B. *J. Phys. Chem. B* **108**, 4127–4133 (2004).

37. Zhang, J. *et al.* Mixed-metal pt monolayer electrocatalysts for enhanced oxygen reduction kinetics. *Journal of the American Chemical Society* **127**, 12480–1 (2005).

38. Sabatier, P. Sabatier. *Ber. Der Deutsch. Chem. Ges.* **44**, 1984 (1911).

39. Stephens, I. E. L. *et al.* Tuning the Activity of Pt (111) for Oxygen Electroreduction by Subsurface Alloying. *Journal of the American Chemical Society* **133**, 5485–5491 (2011).

40. Matengaifa, R. *Design of Platinum Alloy Catalysts for Fuel Cell Electrodes*. 3–9 (Cape Town, 2011).

41. Hammer, B. J. K. N. Electronic factors determining the reactivity of metal surfaces. *Surface Science* **343**, 211–220 (1995).

42. Hammer, B. & Norskov, J. K. Why gold is the noblest of all the metals. *Nature* **376**, 238–240 (1995).

43. Lundqvist, B. I., Gunnarsson, O., Hjelmberg, H. & Nørskov, J. K. Theoretical description of molecule-metal interaction and surface reactions. *Surface Science* **89**, 196–225 (1979).

44. Stamenkovic, V. R. *et al.* Trends in electrocatalysis on extended and nanoscale Pt-bimetallic alloy surfaces. *Nature materials* **6**, 241–7 (2007).

45. Stamenkovic, V. R. *et al.* Improved oxygen reduction activity on Pt3Ni(111) via increased surface site availability. *Science (New York, N.Y.)* **315**, 493–7 (2007).

46. Harris, J. & Andersson, S. H2 Dissociation at Metal Surfaces. *Physical Review Letters* **55**, 1583–1586 (1985).

47. Feibelman, P. & Hamann, D. Electronic Structure of a "Poisoned" Transition-Metal Surface. *Physical Review Letters* **52**, 61–64 (1984).

48. Ruban, A., Hammer, B., Stoltze, P., Skriver, H. . & Nørskov, J. . Surface electronic structure and reactivity of transition and noble metals. *Journal of Molecular Catalysis A: Chemical* **115**, 421–429 (1997).

49. Greeley, J. & Nørskov, J. K. A general scheme for the estimation of oxygen binding energies on binary transition metal surface alloys. **592**, 104–111 (2005).

50. Schweitzer, N., Xin, H., Nikolla, E., Miller, J. T. & Linic, S. Establishing Relationships Between the Geometric Structure and Chemical Reactivity of Alloy Catalysts Based on Their Measured Electronic Structure. *Topics in Catalysis* **53**, 348–356 (2010).

51. İnoğlu, N. & Kitchin, J. R. New solid-state table: estimating d-band characteristics for transition metal atoms. *Molecular Simulation* **36**, 633–638 (2010).

52. Bard, A. J.; Faulkner, L. R. *Electrochemical Methods: Fundamentals and Applications.* 7, 87-136 (John Wiley & Sons: New York, 2000).

53. Muller, K. Tafel: His Life and Science. *Electrochemical Science and Technology Information Resource* 1 (2007).at <http://electrochem.cwru.edu/encycl/art-t01-tafel.htm>

54. Tanner's General Chemistry - Tafel Equation. at <http://www.tannerm.com/Tafel.htm>

55. Tang, D., Lu, J., Zhuang, L. & Liu, P. Calculations of the exchange current density for hydrogen electrode reactions : A short review and a new equation. *Journal of Electroanalytical Chemistry* **644**, 144–149 (2010).

56. Song, C. *PEM Fuel Cell Electrocatalysts and Catalyst Layers Fundamentals and Applications.* 91–92 (Springer: 2008).

57. Donald T. Sawyer, Andrzej Sobkowiak, J. L. R. J. *Electrochemistry for Chemists.* 207 (John Wiley & Sons Inc: NY, 1995).

58. Belanger, a. & Vijh, A. K. Hydrogen Evolution Reaction on Vanadium, Chromium, Manganese, Cobalt. *Journal of The Electrochemical Society* **121**, 225 (1974).

59. Wendt, H. *et al.* ELECTROCATALYSIS AND ELECTROCATALYSTS FOR LOW TEMPERATURE FUEL CELLS: FUNDAMENTALS, STATE OF THE ART, RESEARCH AND DEVELOPMENT Hartmut Wendt. *Quim. Nova* **28**, 1066–1075 (2005).

60. Nørskov, J. K. *et al.* Trends in the Exchange Current for Hydrogen Evolution. *Journal of The Electrochemical Society* **152**, J23 (2005).

61. Greeley, J. & Mavrikakis, M. Alloy catalysts designed from first principles. *Nature materials* **3**, 810–5 (2004).

62. Hwu, H. H., Eng, J. & Chen, J. G. Ni/Pt(111) bimetallic surfaces: unique chemistry at monolayer ni coverage. *Journal of the American Chemical Society* **124**, 702–9 (2002).

63. Greeley, J. & Mavrikakis, M. Near-surface alloys for hydrogen fuel cell applications. *Catalysis Today* **111**, 52–58 (2006).

64. Electron Beam Evapoation. at <http://www.tungsten.com/tipsbeam.pdf>

65. *Electron Beam Evaporation.* 1–2 (Illinois, 2012).at http://www.tungsten.com/tipsbeam.pdf

66. Mattox, D. M. Handbook of Physical Vapor Deposition (PVD) Processing. 333 – 360 (Elsevier, William Andrew: United Kingdom, 2010).

67. Ruban, a., Skriver, H. & Nørskov, J. Surface segregation energies in transition-metal alloys. *Physical Review B* **59**, 15990–16000 (1999).

68. Argaman, N. & Makov, G. *Density Functional Theory — an introduction*. 1–2 (Santa Barbara, 1999).

69. Bligaard, T. & Nørskov, J. K. Ligand effects in heterogeneous catalysis and electrochemistry. *Electrochim. Acta* **52**, 5512–5516 (2007).

70. Nørskov, J. K. *et al.* Origin of the Overpotential for Oxygen Reduction at a Fuel-Cell Cathode. *J. Phys. Chem. B* **108**, 17886–17892 (2004).

71. Van Hove, M. A. *et al.* The surface reconstructions of the (100) crystal faces of iridium, platinum and gold. *Surface Science* **103**, 189–217 (1981).

72. Stamenkovic, V. *The Role of Surface Structure and Surface Composition in Electrocatalysis*. 11–12 (2007).

73. Kitchin, J. R., Nørskov, J. K., Barteau, M. A. & Chen, J. G. Role of Strain and Ligand Effects in the Modification of the Electronic and Chemical Properties of Bimetallic Surfaces. *Physical Review Letters* **93**, 4–7 (2004).

74. Kibler, L. a, El-Aziz, A. M., Hoyer, R. & Kolb, D. M. Tuning reaction rates by lateral strain in a palladium monolayer. *Angewandte Chemie (International ed. in English)* **44**, 2080–4 (2005).

75. Strasser, P., Koh, S., Anniyev, T. & Greeley, J. Lattice-Strain Control of Exceptional Activity in Dealloyed Core-Shell Fuel Cell Catalysts. *Nature chemistry* **2**, 1–29 (2010).

76. Erlebacher, J., Aziz, M. J., Karma, a, Dimitrov, N. & Sieradzki, K. Evolution of nanoporosity in dealloying. *Nature* **410**, 450–3 (2001).

77. Jose A. Rodriguez, W. G. The Nature of the Metal - Metal Bond in Bimetallic Surfaces. *science* **257**, 897–903 (1992).

78. Harrison, W. A. *Elementary Electronic Structure (Revised Edition)*. 860 (World Scientific Publishing Company: 2004).at <http://www.amazon.com/Elementary-Electronic-Structure-Revised-Edition/dp/9812387080>

79. Anand Udaykumar Nilekar, Kotaro Sasaki, Carrie A. Farberow, Radoslav R. Adzic, M. M. Mixed-Metal Pt Monolayer Electrocatalysts with Improved CO Tolerance. *Journal of the American Chemical Society* **133**, 18574–18576 (2011).

80. Kandoi, S., Ferrin, P. a. & Mavrikakis, M. Hydrogen on and in Selected Overlayer Near-Surface Alloys and the Effect of Subsurface Hydrogen on the Reactivity of Alloy Surfaces. *Topics in Catalysis* **53**, 384–392 (2010).

81. Stamenkovic, V. R., Mun, B. S., Mayrhofer, K. J. J., Ross, P. N. & Markovic, N. M. Effect of surface composition on electronic structure, stability, and electrocatalytic properties of Pt-transition metal alloys: Pt-skin versus Pt-skeleton surfaces. *Journal of the American Chemical Society* **128**, 8813–9 (2006).

82. X.G. Lu, B. Sundman, and J. Agren. Thermodynamic Assessment of the Ni-Pt and Al-Ni-Pt Systems, Calphad, **33**, 450-456 (2009)

83. W. M. Makhetha, C.I. Lang, M. Topic. Formation of Ordered Phases in the Pt-V Coating System, Centre for Materials Engineering, 2013.

84. S.A.E. Johansson and J.L. Campbell, and K. G. M. *Particle-Induced X-Ray Emission Spectrometry (PIXE) (Chemical Analysis: A Series of Monographs on Analytical Chemistry and Its Applications)*. 1–17 (Wiley-Interscience: 1995).at <http://www.mrsec.harvard.edu/cams/PIXE.html>

85. Mayer, M. *Rutherford Backscattering Spectrometry (RBS)*. 19–30 (Garching, Germany, 2003).

86. EAG | Rutherford Backscattering Spectrometry, RBS Analysis. at <http://www.eaglabs.com/mc/rutherford-backscattering-spectrometry.html>

87. Tait, W. S. *An introduction to electrochemical corrosion testing for practicing engineers and scientists. Progress in Organic Coatings* **26**, 10–15, 53–62 (Pair O Docs Publications: 1994).

88. AFROX Gas, South Africa, technical consultant, 2014.

89. D. Pletcher, F. C. W. *Industrial Electrochemistry*. 10 – 16 (Chapman and Hall, 1990).

APPENDIX A

Section A.1 briefly discusses electrochemical theory and equations relevant to this project. In section A.2 we see phase diagrams for the PtNi and PtV systems. Section A.3 shows the results obtained from the analysis of the pure reference metals Ni, V and Pt. With regards to Ni and V we see overlaid Tafel plots along with Ra-values. For Pt we see results for different sources of Pt showing overlaid Tafel plots (NiPt), Ra-values and EDS spectra. In section A.4 we see Ra-values obtained for the NSA samples. Overlaid Tafel plots for all samples tested demonstrate reproducible results[87].

A.1 Butler-Volmer and Tafel Equations

The basis of the electrochemical testing for this project is derived from the Butler-Volmer equation as seen below[52,89]:

$$i = i_0\left\{\exp\left[(E-E_e)\frac{(1-\alpha)}{RT}F\right] - \exp\left[(E-E_e)\frac{-\alpha}{RT}F\right]\right\}$$

Anodic part — Cathodic Part

Where,

i: electrode current density (A/m^2)

i_0: exchange current density (A/m^2) [see section 2.3.3]

E: electrode potential (V)

E_e: equilibrium potential (V)

$(E-E_e)$: overpotential, η (V) [see section 2.2.1]

T: temperature (K)

F: Faraday constant

R: universal gas constant

$(1-\alpha)$: anodic charge transfer coefficient

α: cathodic charge transfer coefficient

An important variable to note here is the overpotential (η). The overpotential is the change of the electrode potential from its equilibrium potential[89].

These values can either be negative or positive. The exchange current density occurs at the equilibrium potential which thus implies that the exchange current density occurs when $\eta = 0V$[52,56,89].

In order to understand how the Butler-Volmer equation relates to the work in this project, it is necessary to further simplify it. There are two scenarios under which the Butler-Volmer equation can be simplified; the first being the 'low-field' region which is applicable under low overpotentials ($\eta \leq 50mV$) and the second being the 'high-field' region which occurs at high overpotentials ($\eta > 50mV$)[52,89]. Most electrochemical processes occur in the high-field region and thus for this research only the high-field region is applicable as large overpotentials are applied.

At large negative overpotentials, the anodic contribution to the cathodic reaction becomes negligible and vice-versa. The Butler-Volmer equation can thus be further simplified generating the Tafel Equation[52,89]:

$$\ln(i) = \ln(i_0) + \frac{\eta(1-\alpha)}{RT}F$$

With the Tafel equation being rearranged to represent the cathodic reaction[52,89]:

$$\eta_c = b \cdot \log_{10}\left(\frac{i_0}{i_c}\right)$$

And, likewise the anodic reaction[52,89]:

$$\eta_a = b \cdot \log_{10}\left(\frac{i_a}{i_0}\right)$$

Where b is defined as the Tafel Slope[52,89]

$$b = 2.303\frac{RT}{(1-\alpha)F}$$

In figure A.1 we see a Tafel plot showing the exchange current density and Tafel slopes[89]. The graph supports the fact that the exchange current density can be visually extracted from the Tafel plot at the intersection of the Tafel slopes where η = 0V (i.e. the equilibrium potential).

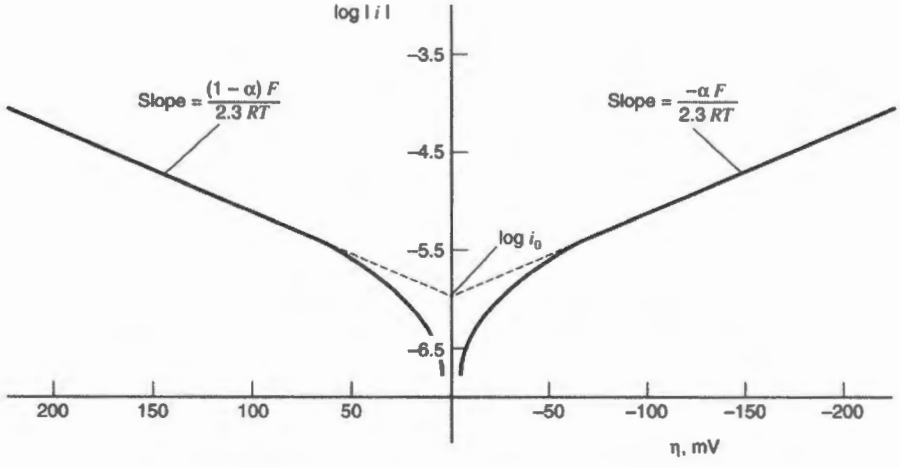

Figure A.1: Tafel plot showing the anodic and cathodic slopes along with the exchange current density (i_0)[89].

A.2 Pt – Ni and Pt – V Phase Diagrams

In figures A.2 and A.3 phase diagrams of the Pt-Ni and Pt-V systems are seen, respectively[82,83].

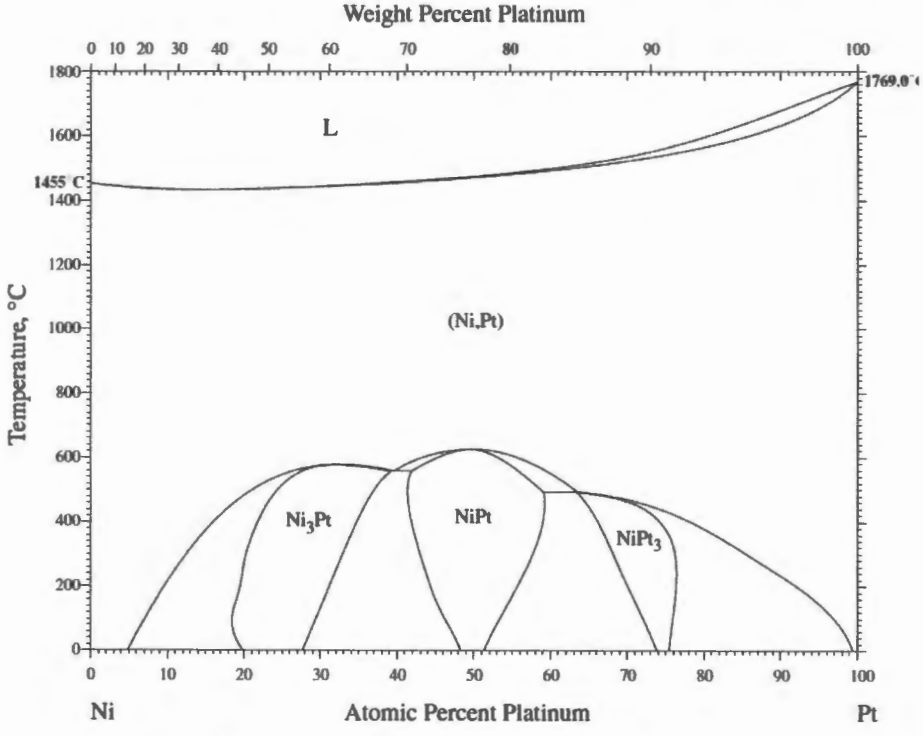

Figure A.2: Pt – Ni phase diagram[82].

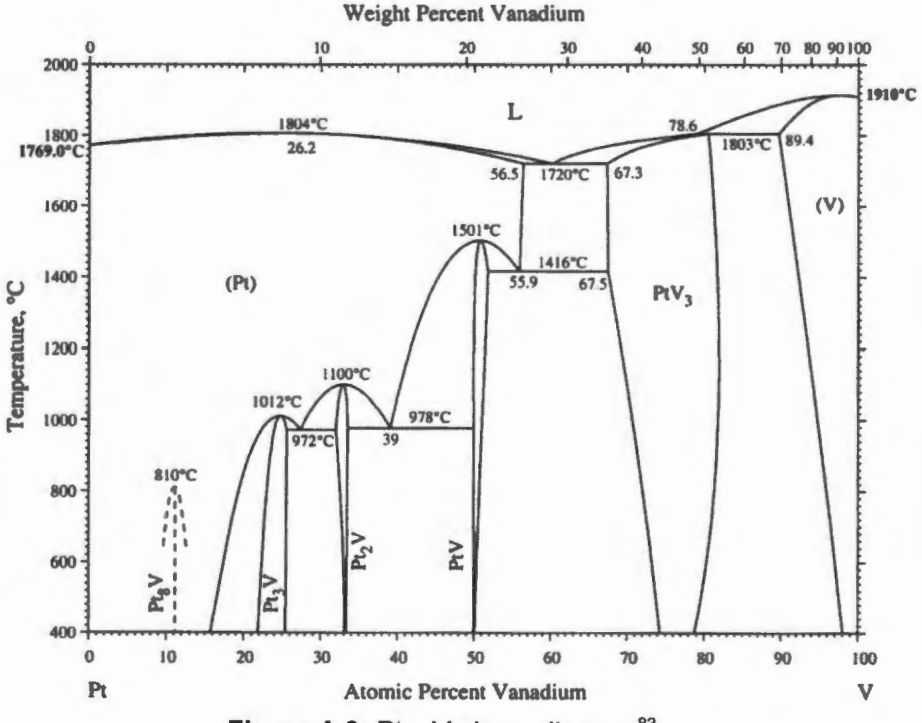

Figure A.3: Pt – V phase diagram[83].

A.3 Pure Metal References

A.3.1 Nickel

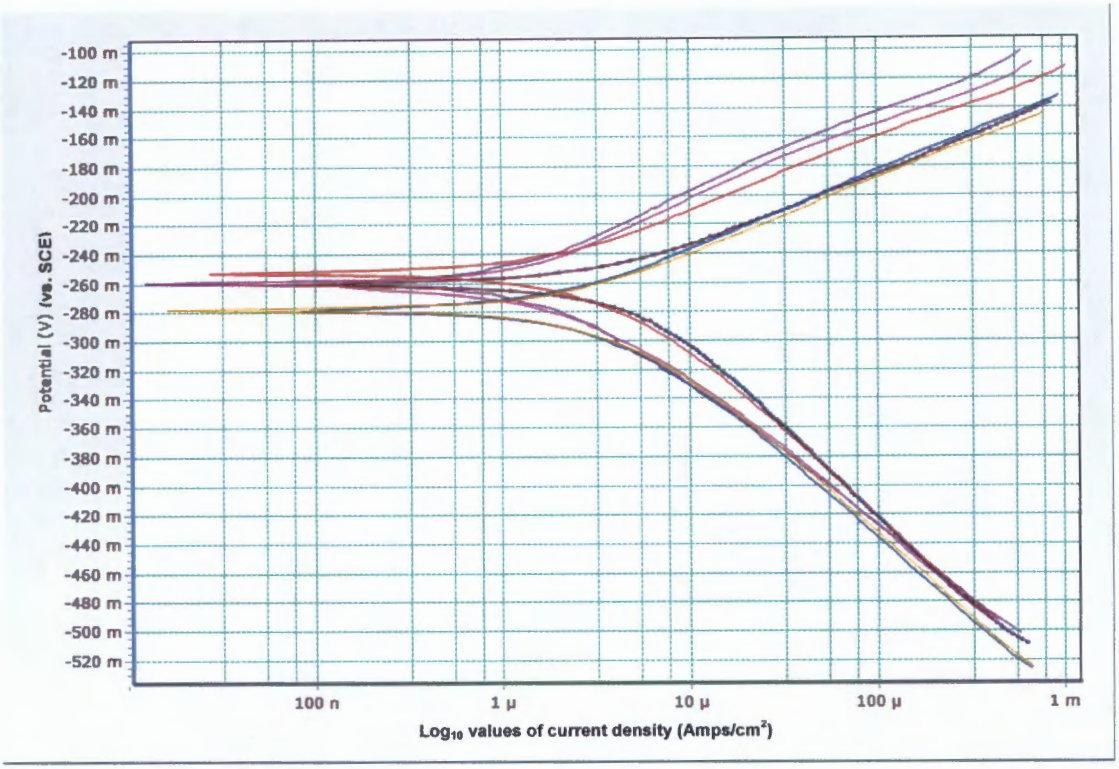

Figure A.4: Seven overlaid Tafel plots of potential (V_{SCE}) vs. log current density (A/cm^2) for Ni.

Table A.1: Ra-values for the Ni samples seen in figure A.4 with measurements taken as shown in section 3.3.3.

Sample Type	Sample #		Ra 1 (µm)	Ra 2 (µm)	Ra 3 (µm)	Ra 4 (µm)	Average (µm)	nm
Ni	1		0.04	0.09	0.19	0.05	0.09	90
	2		0.11	0.15	0.12	0.15	0.13	130
	3		0.09	0.12	0.14	0.09	0.11	110
	4		0.08	0.17	0.07	0.09	0.10	100
	5		0.2	0.06	0.05	0.1	0.10	100
	6		0.13	0.15	0.11	0.12	0.13	130
	7		0.05	0.11	0.12	0.11	0.10	100

A.3.2 Vanadium

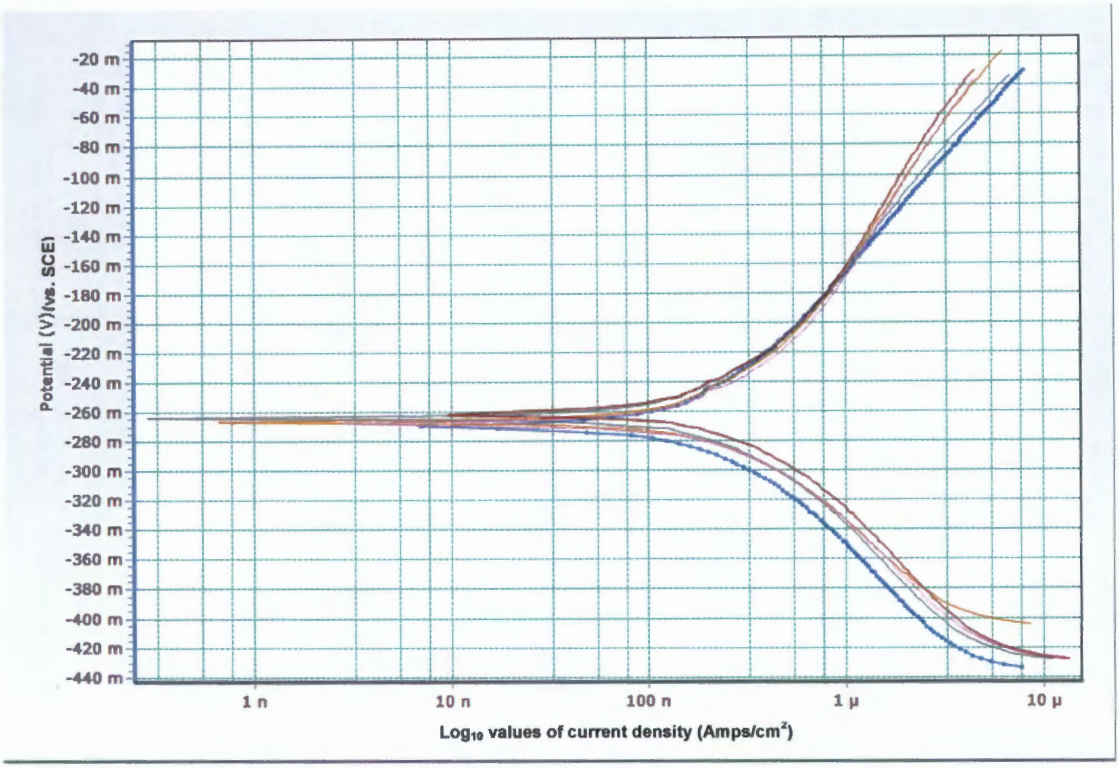

Figure A.5: Five overlaid Tafel plots of potential (V_{SCE}) vs. log current density (A/cm^2) for V.

Table A.2: Ra-values for the V samples seen in figure A.5 with measurements taken as shown in section 3.3.3.

Sample Type	Sample #		Ra 1 (µm)	Ra 2 (µm)	Ra 3 (µm)	Ra 4 (µm)	Average (µm)	nm
V	1		0.11	0.12	0.16	0.1	0.12	120
	2		0.13	0.09	0.1	0.07	0.10	100
	3		0.2	0.15	0.08	0.05	0.12	120
	4		0.09	0.19	0.14	0.18	0.15	150
	5		0.13	0.11	0.18	0.13	0.14	140

A.3.3 (6) NiPt (as pure Pt)

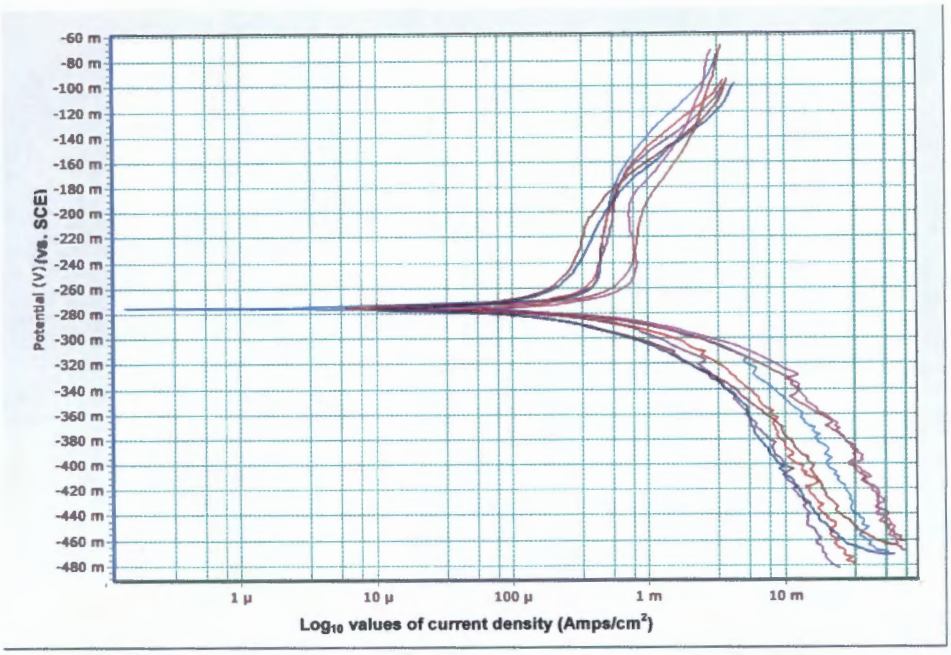

Figure A.6: Seven overlaid Tafel plots of potential (V_{SCE}) vs. log current density (A/cm^2) for NiPt.

Table A.3: Ra-values for the NiPt samples seen in figure A.6 with measurements taken as shown in section 3.3.3.

Sample Type	Sample #		Ra 1 (µm)	Ra 2 (µm)	Ra 3 (µm)	Ra 4 (µm)	Average (µm)	nm
NiPt	1		0.12	0.16	0,20	0.13	0.14	140
	2		0.15	0.13	0.18	0.17	0.16	160
	3		0.11	0.16	0.19	0.14	0.15	150
	4		0.13	0.15	0.16	0.11	0.14	140
	5		0.11	0.10	0.19	0.15	0.14	140
	6		0.17	0.18	0.17	0.19	0.18	180
	7		0.10	0.14	0.13	0.18	0.14	140

A.3.4 Platinum (57g button)

Table A.4: Ra-values for the Pt (57g) samples with measurements taken as shown in section 3.3.3.

Sample Type	Sample #		Ra 1 (µm)	Ra 2 (µm)	Ra 3 (µm)	Ra 4 (µm)	Average (µm)	nm
Pt	1		0.20	0.41	0.24	0.33	0.30	300
	2		0.41	0.22	0.34	0.21	0.30	300
	3		0.33	0.24	0.31	0.42	0.33	330
	4		0.11	0.21	0.32	0.30	0.24	240
	5		0.17	0.16	0.25	0.24	0.21	210
	6		0.38	0.41	0.24	0.21	0.31	310
	7		0.32	0.27	0.44	0.35	0.35	350
	8		0.37	0.28	0.22	0.31	0.30	300

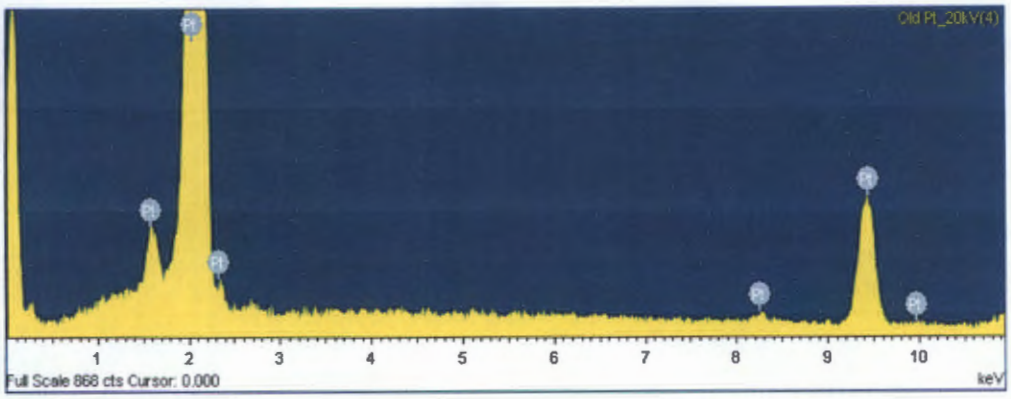

Figure A.7: EDS Spectrum of the Pt (57g) sample (point 2).

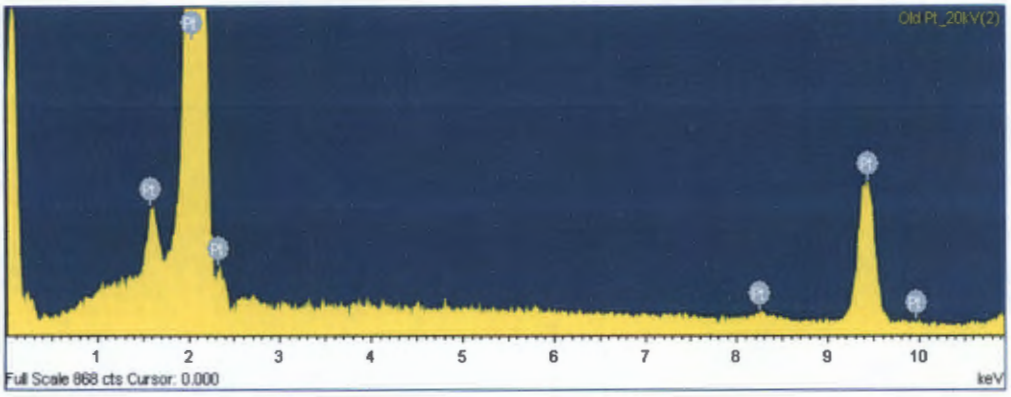

Figure A.8: EDS Spectrum of the Pt (57g) sample (point 3).

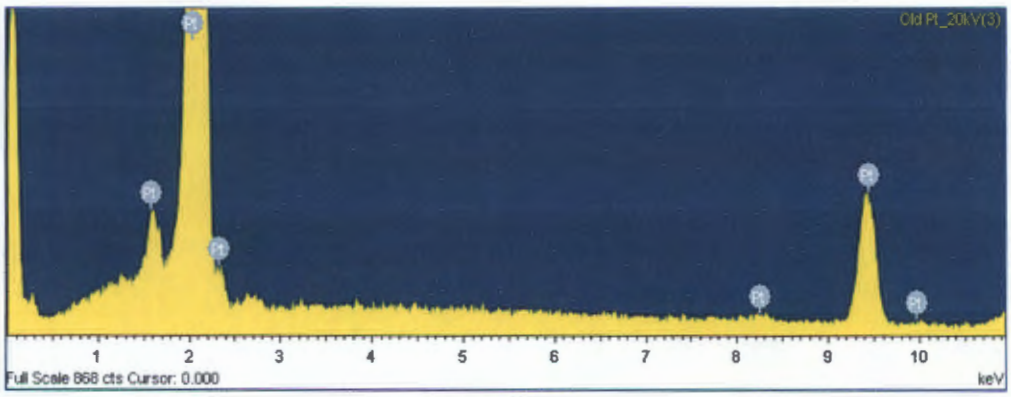

Figure A.9: EDS Spectrum of the Pt (57g) sample (point 4).

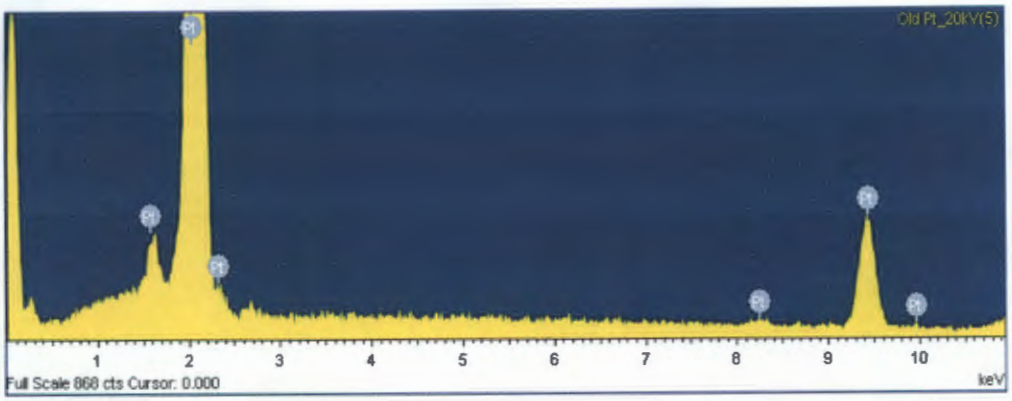

Figure A.10: EDS Spectrum of the Pt (57g) sample (point 5).

A.3.5 Platinum Annealed (57g button)

Table A.5: Ra-values for the annealed Pt samples with measurements taken as shown in section 3.3.3.

Sample Type	Sample #		Ra 1 (µm)	Ra 2 (µm)	Ra 3 (µm)	Ra 4 (µm)	Average (µm)	nm
Pt	1		0.1	0.12	0.11	0.09	0.11	110
	2		0.05	0.14	0.17	0.1	0.12	120
	3		0.07	0.12	0.07	0.04	0.08	80
	4		0.1	0.18	0.06	0.08	0.11	110

A.3.6 Platinum (1g button)

Table A.6: Ra-values for the 1g Pt samples with measurements taken as shown in section 3.3.3.

Sample Type	Sample #		Ra 1 (µm)	Ra 2 (µm)	Ra 3 (µm)	Ra 4 (µm)	Average (µm)	nm
Pt	1		0.17	0.16	0.2	0.04	0.14	140
	2		0.19	0.17	0.19	0.07	0.16	160
	3		0.16	0.17	0.17	0.1	0.15	150
	4		0.18	0.2	0.14	0.12	0.16	160

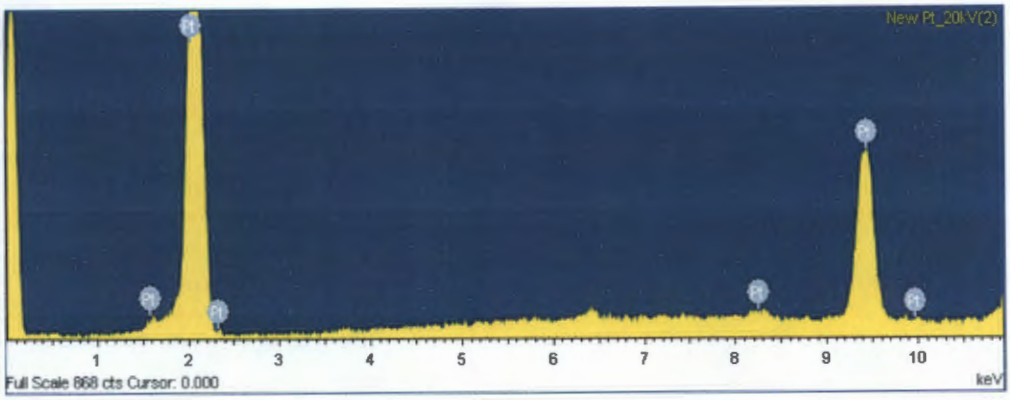

Figure A.11: EDS Spectrum of the Pt (1g) sample (point 2).

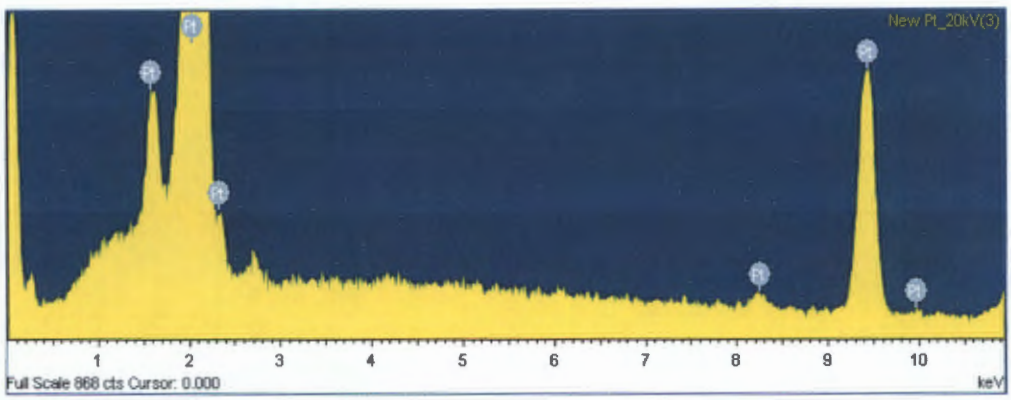

Figure A.12: EDS Spectrum of the Pt (1g) sample (point 3).

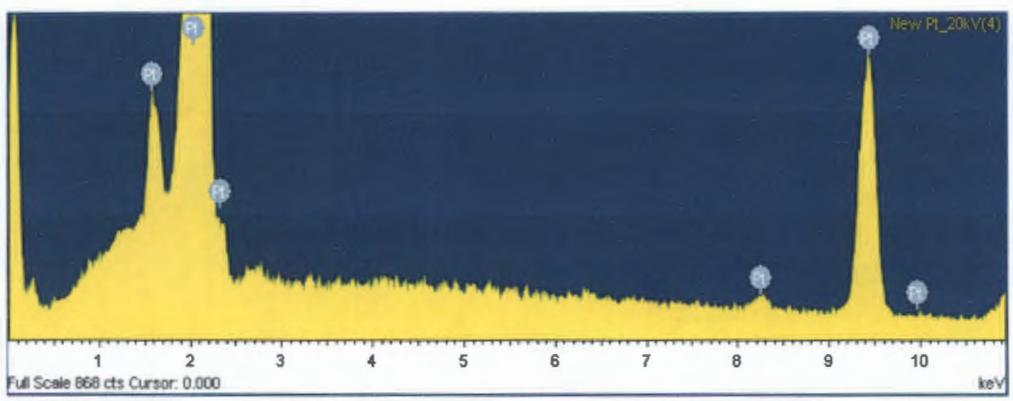

Figure A.13: EDS Spectrum of the Pt (1g) sample (point 4).

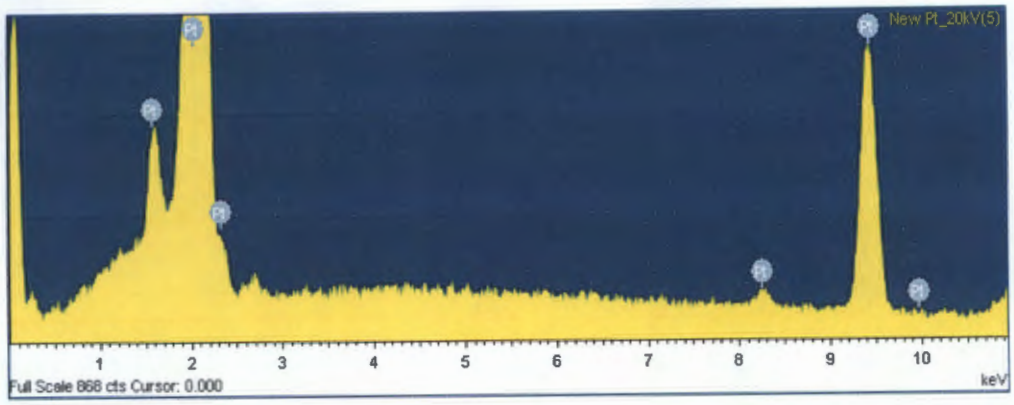

Figure A.14: EDS Spectrum of the Pt (1g) sample (point 5).

A.4 Near-Surface Alloys (NSAs)

A.4.1 (2) PtNi 5nm

Table A.7: Ra-values for the PtNi 5nm samples with measurements taken as shown in section 3.3.3.

Sample Type	Sample #		Ra 1 (µm)	Ra 2 (µm)	Ra 3 (µm)	Ra 4 (µm)	Average (µm)	nm
PtNi 5nm	1		0.06	0.29	0.1	0.13	0.15	150
	2		0.07	0.08	0.07	0.09	0.08	80
	3		0.14	0.14	0.15	0.09	0.13	130
	4		0.07	0.09	0.09	0.07	0.08	80
	5		0.09	0.08	0.08	0.07	0.08	80
	6		0.13	0.12	0.12	0.13	0.13	130
	7		0.09	0.1	0.09	0.09	0.09	90
	8		0.16	0.17	0.23	0.18	0.19	190

A.4.2 (1) PtNi 3nm

Table A.8: Ra-values for the PtNi 3nm samples with measurements taken as shown in section 3.3.3.

Sample Type	Sample #		Ra 1 (µm)	Ra 2 (µm)	Ra 3 (µm)	Ra 4 (µm)	Average (µm)	nm
PtNi 3nm	1		0.12	0.17	0.15	0.12	0.14	140
	2		0.48	0.37	0.33	0.21	0.35	350
	3		0.11	0.14	0.14	0.2	0.15	150
	4		0.14	0.12	0.09	0.1	0.11	110
	5		0.13	0.13	0.14	0.11	0.13	130
	6		0.1	0.12	0.13	0.1	0.11	110
	7		0.12	0.12	0.1	0.13	0.12	120

A.4.3 (5) PtNi Heat Treated

Table A.9: Ra-values for the heat treated PtNi samples with measurements taken as shown in section 3.3.3.

Sample Type	Sample #		Ra 1 (µm)	Ra 2 (µm)	Ra 3 (µm)	Ra 4 (µm)	Average (µm)	nm
PtNi heat treated	1		0.11	0.32	0.18	0.14	0.19	190
	2		0.15	0.26	0.30	0.15	0.22	220
	3		0.76	1.24	0.58	0.52	0.78	780
	4		0.05	0.19	0.17	0.21	0.16	160
	5		0.08	0.11	0.06	0.10	0.09	90
	6		0.30	0.32	0.35	0.12	0.27	270
	7		0.13	0.25	0.12	0.11	0.15	150
	8		0.12	0.22	0.24	0.16	0.19	190
	9		0.21	0.19	0.23	0.17	0.20	200
	10		0.10	0.13	0.11	0.14	0.12	120
	11		0.11	0.09	0.14	0.12	0.12	120
	12		0.22	0.27	0.21	0.19	0.22	220

A.4.4 (4) PtV 5nm

Table A.10: Ra-values for the PtV 5nm samples with measurements taken as shown in section 3.3.3.

Sample Type	Sample #		Ra 1 (µm)	Ra 2 (µm)	Ra 3 (µm)	Ra 4 (µm)	Average (µm)	nm
PtV 5nm	1		0.26	0.28	0.25	0.22	0.25	250
	2		0.08	0.13	0.07	0.11	0.10	100
	3		0.12	0.13	0.16	0.18	0.15	150
	4		0.13	0.14	0.16	0.12	0.14	140
	5		0.44	0.5	0.4	0.22	0.39	390

A.4.5 (3) PtV 3nm

Table A.11: Ra-values for the PtV 3nm samples with measurements taken as shown in section 3.3.3.

Sample Type	Sample #		Ra 1 (µm)	Ra 2 (µm)	Ra 3 (µm)	Ra 4 (µm)	Average (µm)	nm
PtV 3nm	1		0.12	0.15	0.14	0.11	0.13	130
	2		0.11	0.16	0.15	0.12	0.14	140
	3		0.23	0.22	0.16	0.11	0.18	180
	4		0.07	0.3	0.25	0.13	0.19	190
	5		0.12	0.13	0.12	0.15	0.13	130